Nonlinear Analysis and Control of PEM Fuel Cells

Dissertation

zur Erlangung des akademischen Grades

Doktoringenieur
(Dr.-Ing.)

von M.Sc. Markus Grötsch
geb. am 05. Sept. 1975 in Weiden/Oberpfalz

genehmigt durch die Fakultät Elektrotechnik und Informationstechnik
der Otto-von-Guericke-Universität Magdeburg

Gutachter:

Prof. Dr.-Ing. Achim Kienle

Prof. Dr.-Ing. Oliver Sawodny

PD Dr.-Ing. Michael Mangold

Promotionskolloquium am 16. Nov. 2010

Abstract

The present contribution deals with the model-based analysis, the model reduction and the control of polymer electrolyte membrane fuel cells (PEMFCs). In the first part of this work a bifurcation analysis of a PEM fuel cell under two-phase conditions, i.e. the parallel presence of liquid water and water vapor inside the cell, is performed. A steady-state multiplicity is found by this analysis that results from different liquid water contents in the cell that are close to flooding. This multiplicity is physically explained and the dependency on different and significant fuel cell parameters is investigated. Finally, the dynamic behavior of the system in the parameter region, where multiple steady states occur, is also studied in order to completely characterize the multiplicity and therefore increase the knowledge about two-phase PEMFCs close to flooding conditions.

After this analysis, the two-phase model is reduced by applying simplifying physical assumptions in order to obtain a low-order model that can be used for the design of process control strategies in a real-time environment. For this purpose, the reduced model should conserve the qualitative as well as the quantitative behavior of the original model. This is accomplished and shown by comparing steady state and dynamic simulation results of both models.

Prior to the control design, an analysis of the PEM fuel cell and common DC-DC converters is done in order to find out if multiplicities or instabilities are introduced by the coupling of both systems. First of all, the influence of the switching ripples of the DC-DC converters upon the PEMFC is considered. They introduce oscillations in the fuel cell. Their origin is explained, discussed and possibilities for their suppression are given. After this, the overall behavior of the fuel cell and the converters is examined. It is shown mathematically that the coupling between PEM fuel cells and DC-DC converters neither leads to stationary multiplicities nor to oscillations in the coupled system. Therefore, it is not necessary to develop integrated control approaches for the coupled system and one can instead design separate control approaches for both systems.

Finally in this contribution, a passivity-based control approach is developed for a

one-phase PEM fuel cell. The main aims of the control approach are the avoidance of flooding and the undersupply of the fuel cell with hydrogen and oxygen. In the first step, a controllability analysis is performed. It is found that the operating points are completely controllable and that a decentralized control approach can be used. After that, passivity-based control is applied to the PEMFC. This approach is tested for set point control and servo control with disturbances in the load, the temperature and the gas pressures. It is found, that the control approach introduces upper limits for the activities of water vapor and can primarily be used to prevent flooding, while the fuel starvation of the cell is avoided too.

Zusammenfassung

Die vorliegende Dissertation beschäftigt sich mit der modellbasierten Analyse, der Modellreduktion und der Regelung von Polymerelektrolytmembranbrennstoffzellen (PEM-Brennstoffzellen, im englischen kurz PEMFCs).

Im ersten Teil der Arbeit wird das Verhalten von PEM-Brennstoffzellen unter zweiphasigen Betriebsbedingungen, d.h. der gleichzeitigen Präsenz von Wasserdampf und Flüssigwasser innerhalb der Zelle, mit Hilfe einer modellbasierten, nichtlinearen Analyse untersucht. Diese Untersuchung zeigt, daß eine unterschiedlich hohe Sättigung der Zelle mit Flüssigwasser zu stationär mehrdeutigem Zellverhalten führt. Die Ursache dieser Mehrdeutigkeit wird physikalisch erklärt und ihre stationäre Abhängigkeit von wichtigen Brennstoffzellenparametern wird ebenfalls betrachtet. Im Anschluß daran wird auch das transiente Verhalten der Brennstoffzelle um die gefundene Bifurkation untersucht, um damit die Mehrdeutigkeit weiter zu charakterisieren und so insgesamt weitere Erkenntnisse über das Betriebsverhalten von zweiphasigen PEM-Brennstoffzellen zu gewinnen.

Im Anschluß an die Bifurkationsanalyse wird das zugrundeliegende komplexe Zweiphasenmodell einer Modellreduktion unterzogen. Dies geschieht mit Hilfe von vereinfachenden physikalischen Annahmen mit dem Ziel ein niedrigdimensionales, zweiphasiges Modell zu erhalten, dass sich für den Entwurf von modellbasierten Regelungsstrategien und deren Einsatz unter Echtzeitbedingungen eignet. Zu diesem Zweck muß das reduzierte Modell sowohl das qualitative als auch das quantitative Verhalten des Ursprungsmodells aufweisen. Dies wird im Rahmen der Modellreduktion erreicht und durch vergleichende stationäre und dynamische Simulationen beider Modelle gezeigt.

Vor dem abschließenden Regelungsentwurf im letzten Teil der Arbeit wird zuvor das Kopplungsverhalten von PEM-Brenstoffzellen und Gleichspannungskonvertern untersucht. Dabei wird untersucht inwieweit Kopplungen beider Teilsysteme Mehrdeutigketen und Instabilitäten im Gesamtsystem induzieren und damit einen integrierten Regelungsansatz erforderlich machen. Zuallererst wird der Einfluß der Schaltwelligkeit der Konverter auf die PEMFC betrachtet. Es zeigt sich, daß dadurch

Oszillationen in der Brennstoffzelle hervorufen werden. Der Ursprung dieser Oszillationen wird erklärt, diskutiert und Möglichkeiten zu ihrer Unterdrückung werden aufgezeigt. Danach wird das eigentliche Verhalten des gekoppelten Brennstoffzellen-Konverter-Systems untersucht. Es wird mathematisch gezeigt, daß die Kopplung zwischen PEMFC und Gleichspannungskonvertern weder zusätzliche Mehrdeutigkeiten noch Oszillationen in das Gesamtsystem einbringt. Aus diesem Grund ist es nicht nötig einen integrierten Regelungsansatz für das gekoppelte System zu entwerfen sondern man kann sich auf den Entwurf von separaten Ansätzen für Brennstoffzelle bzw. Konverter konzentrieren.

Der letzte Teil dieser Arbeit beschäftigt sich mit dem Entwurf eines passivitätsbasierten Regelungsansatzes für PEM-Brennstoffzellen. Die wesentlichen Ziele dieses Ansatzes sind dabei die Vermeidung von Zellflutung bzw. die Unterversorgung mit Reaktanten während des Betriebs. Vor dem eigentlichen Regelungsentwurf wird zuerst die Steuerbarkeit des dem Regelungsansatzes zugrundeliegenden Brennstoffzellenmodells untersucht. Dies wird anhand von stationären Arbeitspunkten des Modells durchgeführt. Es zeigt sich im Zuge dieser Analyse, daß diese Arbeitspunkte vollständig steuerbar sind und ein dezentraler Regelungsansatz verwendet werden kann. Danach wird eine passivitätsbasierte Regelung für die PEM-Brennstoffzelle entworfen und ihr Leistungsvermögen im Hinblick auf Störunterdrückung bei Festwertregelung und Folgeregelung simulativ erprobt. Dabei zeigt sich, daß der Regelungsansatz die vorgegebenen Ziele erfüllt und besonders einer Flutung der Zelle entgegenwirken kann.

Acknowledgement

This thesis is the result of my research activity as a scientific assistant at the Max Planck Institute for Dynamics of Complex Technical Systems in Magdeburg from March 2005 till April 2009. During this time I joined the Process Synthesis and Process Dynamics group led by Prof. Dr.-Ing. Achim Kienle. I am deeply grateful to him for giving me the chance to do my PhD thesis under his supervision.

I also want to thank Prof. Dr.-Ing. Oliver Sawodny for his effort in co-reporting and for his interest in this research.

Furthermore, my deep gratitude goes to Dr.-Ing. Michael Mangold with whom I closely cooperated during my PhD study. I want to thank him for his kindness and readiness to assist me during the whole period of my work and also for his suggestions and useful discussions. He was and is a real source of knowledge.

Additionally, I want to thank Dr.-Ing. Richard Hanke-Rauschenbach for his solid support and inspiring ideas in fuel cell modeling.

Also I want to thank Prof. Dr.-Ing. Andreas Lindemann for useful discussions and hints concerning DC/DC converters.

Finally, I want to thank all my colleagues at the Max Planck Institute especially for the inspiring discussions we had during our lunch breaks.

Puchheim, November 2010 Markus Grötsch

Contents

List of Symbols[1]

Greek symbols

Quantity	*Description*	*Value/Unit*
$\tilde{\alpha}$, α	transport coefficient of membrane	$[mol^2/J\,m\,s]$
β	fitting parameter of reduced two-phase model	$[-]$
χ	concentration	$[mol/m^3]$
$\Delta\phi_{eq}$	equilibrium potential of the cathodic reaction	$[V]$
$\tilde{\eta}$, η	overvoltage at the catalyst layer	$[V]$
γ	active surface area of the catalyst per unit volume	$[1/m]$
$\tilde{\lambda}$, λ	membrane humidity	$[-]$
μ	viscosity	$Pa\,s]$
$\tilde{\varpi}$	electrochem. potential	$[J/mol]$
ν	Nafion content in catalyst layers	$[-]$
π	porosity	$[-]$
$\tilde{\phi}$	electrical potential	$[V]$
φ	charge transfer coefficient	$[-]$
$\tilde{\rho}$, ρ	density	$[kg/m^3]$
ϱ	gas constant	$8.314\ J/mol\,K$
σ_{H_2O}	surface tension of water	$[N/m]$
$\tilde{\sigma}$, σ	electrical conductivity	$[S/m]$
θ	contact angle of water	$[deg]$

continued ...

[1]The symbols marked with a tilde are used together with the detailed two-phase PEMFC model in chapter 3 and indicate beside a time-dependency also a spatial dependency. This is in contrast to the reduced and concentrated two-phase model in chapter 4 where equal symbols but without a tilde are used.

Quantity	*Description*	*Value/Unit*
ϑ	cell temperature	$[K]$
ξ	electro-osmotic drag coefficient	$[-]$
ζ	no. of exchanged electrons during reaction	$[-]$

Latin symbols

Quantity	*Description*	*Value/Unit*
$\tilde{a}$, a	activity of water	$[-]$
A	cross-sectional area of fuel cell	$[m^2]$
$\tilde{c}$, c	mass fraction	$[-]$
C	capacitance	$[F]$
C_{dl}	double layer capacitance	$[F/m^2]$
D	binary diffusion coefficient	$[m^2/s]$
d	thickness	$[m]$
EW	equivalent weight of the dry membrane	$[kg/mol]$
$\tilde{f}$, f	volume fraction	$[-]$
F	Faraday constant	$96485.3\ C/mol$
i	current density	$[A/m^2]$
I	electrical current	$[A]$
$\tilde{j}^e$, j^e	electrical current density in the carbon phase	$[A/m^2]$
$\tilde{j}^l$, j^l	mass flow density of liquid water	$[kg/m^2\,s]$
$\tilde{j}^p$, j^p	current density in the proton conducting phase	$[A/m^2]$
$\tilde{j}^\iota$, j^ι	mass flow density of gas species ι	$[kg/m^2\,s]$
K	abs. permeability of catalyst & gas diffusion layers	$[m^2]$
K_m	absolute permeability of the membrane	$[m^2]$
k_{con}	condensation rate	$[1/s]$
k_{vap}	evaporation rate	$[1/Pa\,s]$
L	inductivity	$[H]$
$\tilde{M}$, M	molar mass	$[kg/mol]$
$\tilde{p}$, p	pressure	$[Pa]$
$\tilde{Q}^l$, Q^l	kinetics for condensation/vaporization	$[kg/m^3\,s]$
$\tilde{Q}_{ch}$	charge generation rate	$[C/s\,m^3]$
$\overline{q}$	duty ratio of DC-DC converters	$[-]$
q	duty cycle of DC-DC converters	$[-]$
$\tilde{\mathfrak{r}}$	radius of liquid water channels in membrane	$[m]$
r	areal ohmic resistance	$[\Omega\,m^2]$
R	ohmic resistance	$[\Omega]$
$\tilde{S}$, S	fraction of expanded channels in the membrane	$[-]$

continued ...

Quantity	*Description*	*Value/Unit*
$\tilde{s}^l$, s^l	liquid water saturation	$[-]$
t	time	$[s]$
T	duty period DC-DC converters	$[s]$
U	voltage	$[V]$
v	molar volume	$[m^3/mol]$
$\dot{V}$	volume flow rate	$[m^3/s]$
U	voltage	$[V]$
V	volume	$[m^3]$
x	molar fraction	$[-]$
z	spatial coordinate	$[m]$

Sub- and Superscripts

Quantity	*Description*
a	anode
m	membrane
b	gas bulk
c	cathode
$catl$	catalyst layer
$cell$	cell
cp	capillary
cap	capacitor
$d\Omega$	boundary of modeling domains
dl	double layer
e	electrical
p	protonic
g	gas
gdl	gas diffusion layer
H_2	hydrogen
H_2O	water vapor
HI	hydrophilic pores
HO	hydrophobic pores
in	input
ind	inductor
κ	modeling domains
l	liquid water
$load$	load
m	membrane

continued ...

Quantity	*Description*
max	maximum
min	minimum
N_2	nitrogen
O_2	oxygen
ref	reference
sat	saturation
s	stationary
tot	total

CHAPTER 1

Introduction

The world's energy situation is at crossroads. The energy demand is continually rising since the 1970s and this rise is expected to continue due to the rapid technological advance of newly industrializing countries like China or India [35]. Up to now, the main sources for energy are fossil fuels like coal, oil and gas that supply the global energy demand to more than 80 percent [34]. If the current composition of the energy sources is not changed an irreversible climatic change driven by the emission of carbon dioxide by the energy-related combustion of fossil fuels is going to happen with catastrophic consequences especially in third world countries [59].

In order to cope with both the increasing energy demand and the climatic change there is a need for efficient and carbon-free energy sources. Besides renewable energies like hydro, wind and solar energy for example, hydrogen energy and fuel cells are expected to be a hot candidate for that [30]. In 2004, the European Commission set up the European Hydrogen & Fuel Cell Technology Platform (HFP) in order to prepare and direct an effective strategy for bringing hydrogen & fuel cells to market and to exploit their outstanding environmental and economic potential. The HFP proposes a 10 year research, development and demonstration program including hydrogen production technologies, hydrogen storage technologies and fuel cell technologies [22, 23]. While the main goals in hydrogen production and storage deal with the research on hydrogen production from fossil fuels, renewable and carbon free energy sources and the development of novel storage materials and principles, the key challenges in fuel cells are improvements in fuel cell durability, performance and economics. Finally, this program has now been launched in October 2008 and the European Commission, the European Industry and the European Research Community will invest together nearly 1 billion Euros over the next six years to achieve these ambitious goals [21].

The most promising types of fuel cells are hydrogen-oxygen fuel cells. They are named after the underlying electrochemical reactions: The division of hydrogen into electrons and protons and the combination of protons, electrons and oxygen to

water. Both reactions are spatially separated. Electrons, which are obtained from the first reaction and needed by the second one, are transported via an electrical circuit and perform work before they are consumed by the second reaction [56]. Since fuel cells produce electrical energy directly from chemical energy, they are often far more efficient than combustion engines. Unlike combustion engines, fuel cells do not need moving parts for energy conversion. This inherits the potential for highly reliable and long-lasting systems. A lack of moving parts also means that fuel cells are silent. Finally, the undesirable products such as NO_x, SO_x and CO_2 of fossil fuel driven combustion engines are also avoided.

Hydrogen-oxygen fuel cells [43, 71, 76] can be classified according to their operating temperature in high temperature and low temperature fuel cells. Promising fuel cell types at high temperature are the molten carbonate fuel cell and the solid-oxide fuel cell. They are most suitable for stationary applications. For mobile applications, like cars and boats, the polymer electrolyte membrane fuel cell [4] is most suitable. The polymer electrolyte membrane fuel cell is a low temperature fuel cell and will be introduced in more detail in the next section.

1.1 PEM fuel cell - working principle

Figure 1.1 shows a sketch of the internal structure of a polymer electrolyte membrane fuel cell (PEMFC). The working principle of the fuel cell is quite simple. At the

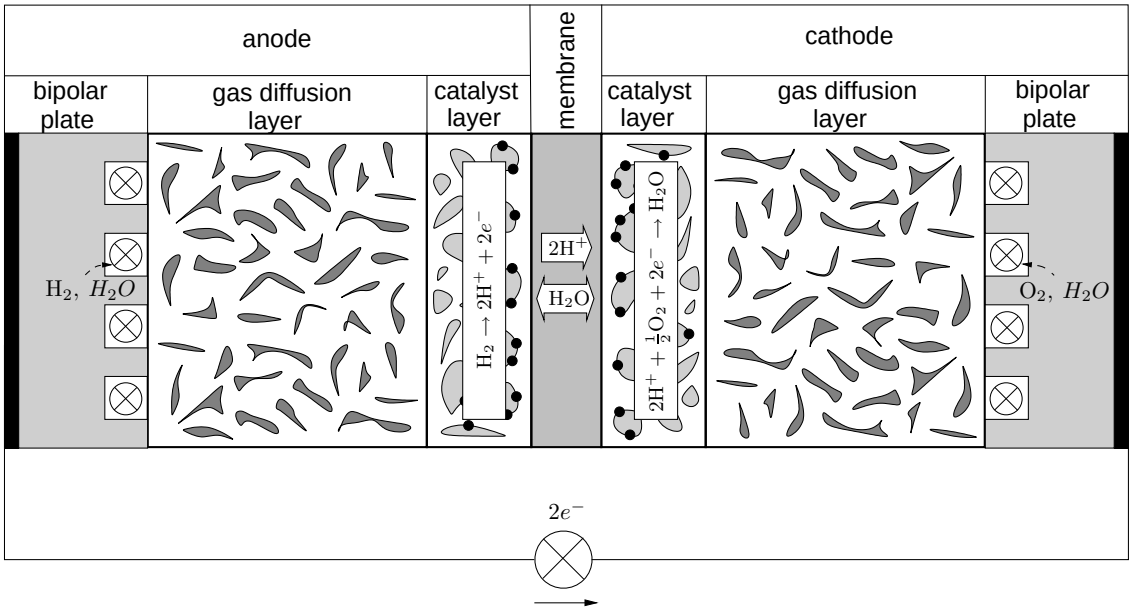

Figure 1.1: Internal structure of a PEM fuel cell.

anode side, hydrogen reacts to protons and electrons. The protons are transported through the membrane to the cathode side, while the electrons arrive there via the

external electrical circuit and perform work by doing this. At the cathode side the protons, the electrons and oxygen react together to water.

The heart of the fuel cell is a thin polymer membrane. This membrane must conduct protons on the one hand and must be impermeable to the reactant gases hydrogen and oxygen as well as to the electrons, produced and consumed at both electrodes on the other hand. Moreover, the membrane should also be chemically and mechanically stable to avoid degradation effects in the fuel cell environment. The membrane is typically 25 to 250 μm thick and made from Nafion^{TM}, a product from DuPont. Due to the use of this material, the proton conductivity of the membrane depends strongly on its water content and allows the exchange of water from the anode to the cathode side and vice versa.

The membrane is located between the electrodes. Both electrodes are made up from a catalyst layer (CATL) and a gas diffusion layer (GDL). In the catalyst layers, the electrochemical reactions of the fuel cell take place. At the anode side, hydrogen is oxidized to protons and at the cathode side oxygen and protons are reduced to water. In these reactions three species participate: hydrogen/oxygen, protons, and electrons. The places where these reactions occur are therefore called triple-phase boundaries and are between 10 and 50 μm thick. In order to generate these boundaries, the membrane, the gas phases and the electron conducting catalyst must be in close contact. The most common catalyst in PEM fuel cells, for both the oxygen reduction and the hydrogen oxidation reactions, is platinum.

The gas diffusion layer is located between the bipolar plate and the catalyst layer and does not directly participate in the electrochemical reaction but has to fulfill several supporting functions. First of all, it provides a pathway for reactant gases and product water from the bipolar plate to the catalyst layer and vice versa. Moreover, the GDL electrically connects the catalyst layer to the bipolar plate, allowing the electrons to close the electrical circuit. Finally, it allows the removal of heat generated in the electrochemical reactions inside the catalyst layer and provides mechanical support for both the membrane and the catalyst layer. The gas diffusion layer is typically between 200 and 400 μm thick and made from porous carbon fiber based materials.

Finally, the GDLs are electrically connected to the external circuit via the bipolar plates. Besides the electrical conductance, the bipolar plates are also used to remove heat from the cell, to distribute the reactant gases, to lead away the product water and to provide mechanical support for the fuel cell. Typically, bipolar plates are made from metal, carbon composite materials or a combination of both.

More information about PEMFC materials and their properties can be found in [4, 29, 47, 48, 76]. Information about the modeling of PEM fuel cells is available in [4, 57, 68, 69, 89] for example.

1.2 State of the art in PEMFC technology and aim of this work

Up to now, PEM fuel cells have still some problems concerning economics, durability and performance. The cost of a PEMFC stack is made up from the sum of the individual costs for the membrane, the electrode, the bipolar plates, the platinum catalyst, the peripheral materials and the cost for assembly. The total cost for a prototype PEMFC stack are currently around 1800-2000 $/kW and are dominated by the costs for manually made bipolar plates and electrodes including the platinum catalyst. Nevertheless it is expected that through mass-scale production and the usage of new membrane and catalyst materials the costs for a PEMFC stack can be reduced below 100 $/kW [32, 33].

Currently, PEMFCs are less durable than combustion engines. Under operating conditions occurring in vehicles like cyclic loads and frequent starts and stops, the typical lifetime of a PEMFC stack is around 2,000 hours. This corresponds to about 100,000 km. In stationary applications, the lifetimes are up to 30,000 hours. The goal for stationary applications is an operating life of 40,000-60,000 hours or 5-8 years of operation, while in mobile applications a life of 3,000-5,000 hours for cars and up to 20,000 hours for buses is required [32, 33]. The problems considering the durability and the performance of PEM fuel cells can be subdivided in two categories: (i) Degradation effects due to contamination, corrosion and mechanical failure of PEMFC components and (ii) degradation impacts due to insufficient strategies for reactant gas supply, thermal management and water management.

In PEMFCs the contamination, corrosion and mechanical failure of the membrane, the catalyst layers and the gas diffusion layers are detrimental to fuel cell life and among the important degradation mechanisms. In Nafion^{TM} membrane the formation of hydroxyl (*OH) and peroxyl (OOH) radicals is observed in fuel cell operation. It is supposed that the radicals originate from hydrogen peroxide (H_2O_2) which can be formed prior to the formation of water. The chemical attack of these radicals at polymer end groups of the membrane causes the build up of fluorides that lead to a thinning of the membrane and facilitates the reactant gas crossover which in turn facilitates the formation of hydrogen peroxide. Due to the crossover of the reactant gases and their reaction in the reverse electrodes, mixed potentials and hot spots resulting in pinhole formation in the membrane occur, which in turn facilitate the gas crossover [9, 17, 63, 83]. Both effects lead to a deterioration of the cell performance and the cell durability. Besides the corrosion inside the membrane, its contamination with metal ions from bipolar plates, humidifiers and tubing materials, and ammonia from fuel impurities can also lead to a decreased proton conductivity of the membrane and to a significant loss in fuel cell performance [9, 12]. Membrane degradation can also be caused by mechanical failures of the membrane. During the normal operation of the fuel cell, the components of the PEMFC are put under compressive force to ensure good electrical conductivity between them. Under this constant compressive stress, the membrane can creep or crack and cause membrane thinning and pinholes that can lead together with membrane corrosion to a fast loss

in durability of a PEMFC [9].

The corrosion and contamination of the catalyst layers is another fundamental mechanism that strongly influences the performance and the durability of PEMFCs in the long run. Corrosion of the catalyst layer means the loss of electrochemically active surface area (ECSA) of the platinum catalyst in this layer. This effect happens primarily at the cathodic side of the fuel cell and results from two mechanisms: (i) The redistribution (agglomeration/sintering) of initially small narrow and uniformly dispersed platinum particles to form larger particles which are then distributed more widely, and (ii) the oxidation of the carbon support in the catalyst layer to carbon dioxide. While the first mechanism leads to larger platinum particles, the second mechanism degrades the carbon support and leads to the formation of unsupported platinum particles. Both mechanisms result in a smaller ECSA, which means higher activation losses and eventually a loss in the output voltage and the cell performance [9, 17, 63, 83]. Beside the corrosion, the contamination of the catalyst with carbon monoxide (CO), carbon dioxide and hydrogen sulphide is also very harmful. Carbon monoxide can be present in the hydrogen feed stream when the fuel is obtained by reforming liquid hydrocarbons or alcohol fuels. It is found that even small amounts of carbon monoxide and hydrogen sulphide are sufficient to poison the catalyst resulting in a lower cell voltage and a decreased cell performance [9, 12]. Finally, corrosion effects also appear in gas diffusion layers. Due to their carbon structure, the GDLs are also susceptible to the carbon oxidation which can result in a loss of their hydrophobic character and their pore structure. This can lead to higher water contents in the GDL and can impede the mass transport of reactants to the reaction sites [9, 17, 83]. The impacts of the presented degradation effects can be substantially decreased by the development and usage of improved materials. Concerning the membrane, good progress has been made in the past few years by using chemically modified and reinforced membranes, but a full evaluation of these improved materials has still to be carried out. Concerning the catalyst layer and the GDLs, the trend is towards alternatives for platinum, such as Pt-alloys, and to alternative support materials and new electrode concepts [9, 83].

The durability and performance of a PEM fuel cell is also strongly influenced by its operation strategy concerning the reactant gas supply, the thermal and the water management of the cell. An insufficient management of the reactant gases during fuel cell operation can lead to an undersupply of the fuel cell, i.e. the catalyst layers with reactant gases. This is called starvation and typically results from an obstruction of the flow-paths in the bipolar plates or the gas diffusion layers with liquid water or ice. Another cause for starvation is the insufficient reactant feeding of the PEMFC at sudden changes in the power demand leading to a transient form of starvation. Starvation at the anode side, i.e. hydrogen starvation, is also possible due to the presence of air inside the anodic catalyst layer prior to the start-up of the fuel cell. Similarly, air starvation at the cathode side can also happen, e.g. at a restart of the cell after a prior shutdown and nitrogen purge. The main consequences of fuel starvation are an intensified corrosion of the carbon support in the anodic and cathodic catalyst which results in a permanent loss of catalyst there. The main

consequences of air starvation is a rapid cell reversal, i.e. the evolution of hydrogen at the cathode side, which can lead together with oxygen to an undesired later heat generation that further stresses the membrane and the catalyst. The final result of starvation is a deteriorated cell performance [9, 63, 86].

Besides an undersupply of the PEMFC with reactant gases, the thermal management is also of significance for the fuel cell's durability and performance. It has been found that improper thermal management that permits the appearance of high cell temperatures ($> 80°C$), for example due to a transient change from low to high power demand, leads to an increased membrane and catalyst degradation since higher temperatures promote the occurrence of radicals and the loss of ECSA and therefore leads to a shortened cell durability [17]. Another significant issue for thermal management is the start-up and shut-down of a PEMFC from subfreezing temperatures, a feature that is especially required for automotive applications. If the water generated in the cathode is not removed while the cell starts-up from subfreeze temperatures, ice will be formed inside the catalyst layer, the gas diffusion layer and the bipolar plate which can hinder or even block the reactant gas from streaming to the catalyst. Therefore, it is important that the cell temperature climbs quickly above the freezing temperature of water before the ice can completely block the catalyst layer and leads to a significant drop in the cell performance [9, 36, 63].

The thermal management is also closely related to the water management of a PEM fuel cell. The operation of a PEMFC is fundamentally linked with the presence of water in the cell, that has a major impact on its performance and durability [63, 85]. On the one hand, water is important to keep the membrane humidified and ensure a high proton conductivity and therefore the desired cell performance. If this is not the case, i.e. too little water is inside the cell, a dehydration of the membrane can be observed. This is called drying out and leads to a higher protonic resistance and therefore to a loss in the cell voltage and the available cell power. A too long operation of the membrane in a dried state can also lead to an increased generation of radicals and therefore to an enhanced membrane degradation [17]. On the other hand, the accumulation of water inside the cell can impede and block the reaction sites, the pores of the GDLs and the flow channels in the bipolar plates. This is called flooding and can directly [17] and indirectly enhance the carbon corrosion of the catalyst support via the previously described reactant starvation. Both extremes, flooding and drying out, decrease the durability and the performance of the fuel cell. Therefore, a proper water management is important and consists in maintaining, during fuel cell operation, the equilibrium between: (i) The water carried inside and outside the cell by the inlet and outlet gases, (ii) the water generated in the cathodic catalyst layer by the electrochemical reaction, (iii) the water transported by the electro-osmosis and back diffusion through the membrane, (iv) the temperature in the fuel cell and (v) the gas pressure inside the PEMFC.

The impacts of impure reactant gas, thermal and water management can be significantly reduced by using appropriate control approaches for the PEM fuel cell [75, 86]. Considerable progress has been made in order to avoid starvation and overheating of the fuel cell by applying linear [58], nonlinear [15] and model predictive

control approaches [27] to the PEMFC. The understanding and the control of the water household is more difficult and requires a detailed understanding, especially if low temperature fuel cells with a two-phase water household, i.e. the parallel presence of liquid water and water vapor inside the cell are considered. This work tries to contribute both to the understanding and the control of the water household in PEMFCs by performing model-based analysis and synthesis there. For this purpose, models of the PEM fuel cell are necessary and therefore introduced in chapter 2 prior to the presentation of the actual analysis and synthesis approaches. The aim of chapter 3 is devoted to the first goal, an improved understanding of the water household. For this purpose, the two-phase water household of a low temperature PEM fuel cell is analyzed. This investigation is model-based and carried out by performing a bifurcation analysis of a representative two-phase PEMFC model. In chapter 4, a reduced two-phase PEMFC model that can be used for the development of model-based control approaches is derived. This model is obtained via a model reduction by applying simplified physical assumptions upon the detailed two-phase model used for the bifurcation analysis in chapter 3. After this, and before the development of the control approach, the coupling between PEM fuel cells and DC-DC converters is analyzed in chapter 5. A PEMFC that is used to supply a DC load at different voltage levels is typically connected to the load via a DC-DC converter. The coupling of a PEMFC and such a converter may induce nonlinear phenomena like instabilities and oscillations that are not present in the single systems and may require an integrated control approach for the coupled system that cannot be replaced by separated control approaches for the single systems. Therefore, in order to clarify this, a model-based analysis of the coupling between a PEMFC and common DC-DC converters is done in this chapter. After this, a nonlinear control approach for the water management is developed in chapter 6 and tested in simulations for set-point control and servo control. Finally, the results of this work are summarized in the conclusion in chapter 7.

CHAPTER 2

Modeling overview

In the previous chapter the potential as well as the problems concerning the operation of polymer electrolyte membrane fuel cells (PEMFCs) have been stated. It was pointed out that the water management is one major problem there. This work tries to contribute to a solution of this problem by analyzing its roots and proposing a control strategy to avoid it. For this purpose, representative models of the PEMFC with different modeling depths depending on the respective aim, i.e. analysis or synthesis are necessary. Therefore, before the actual analysis and synthesis is performed in the subsequent chapters, this chapter presents, displays connections and differences and summarizes these different models.

In this work four models are used. For the model-based analysis of the water household in chapter 3, i.e. the flooding phenomena, a very detailed model of a PEMFC operated under two-phase conditions is necessary. Therefore, a rigorous, distributed two-phase model from [90] is chosen and modified with respect to the boundary conditions and presented in section 2.1. While this distributed model forms a suitable basis for the model-based analysis, it is too complex for the design of a nonlinear control approach for two-phase PEMFCs. For this aim, a simpler and reduced two-phase model that can be used in a real-time process environment is desirable. Therefore, a model reduction is done via simplifying physical assumptions and the outcome, a reduced two-phase model, is stated in section 2.2, while the actual model comparison between detailed and reduced model is performed in chapter 4.

After the model reduction, an intermediate step has to be taken prior to the controller design in chapter 6. In fuel cell operation, PEMFCs are connected to its load via power conditioning units (PCUs). This is typically done to adapt the power delivered from the PEM fuel cell to the load's demand. For DC loads this can be achieved with DC-DC converters. If a DC-DC converter is attached to a PEM fuel cell a complex dynamic system is created that might lead to phenomena like multiplicities or oscillations, which are not present in the single systems. Therefore,

a detailed investigation of the coupling is necessary in order to clarify if an integrated control approach of the coupled system is indispensable or can be substituted by particular control designs. A mathematical and model-based analysis is a suitable way to do this by either highlighting the reason for nonlinear behavior in the coupling or proving the non-existence of it there. Therefore, a suitable PEMFC model is obligatory that incorporates the relevant PEMFC dynamics that can potentially play a vital role in the coupling between fuel cell and DC-DC converters. These are the fast dynamics of the electrochemical reactions, because only the rapid discharging and recharging effects of the double layers [71] can show time transients, in the order of magnitude of milliseconds and smaller, similar to that of DC-DC converters. Due to this reasoning, the PEMFC model utilized for the coupling analysis is quite simple including only the dynamics of the electrochemical reactions and the gaseous mass transport and neglecting the slow dynamics of the liquid water transport in the gas diffusion, the catalyst layer and the membrane. This model is presented in section 2.3.

After the coupling analysis is done in chapter 5, the focus of this work is shifted towards the control of PEM fuel cells in chapter 6. Prior to the actual controller development for a PEMFC operating under two-phase conditions, where the reduced model in chapter 4 forms a solid basis, an intermediate step is necessary: The two-phase modeling of the gas manifolds in PEM fuel cells. This is a necessary step, because in PEM fuel cells operating under two-phase conditions liquid water is not only built in the fuel cell itself but also in the gas manifolds [6, 72, 74]. This leads to a qualitative change in the behavior of the gas bulks and has to be taken into account by a model-based control approach. Therefore, liquid water can also hinder and block the transport of reactants and the removal of water in the gas bulks like it happens in the gas diffusion and catalyst layers. Due to this, a parallel strategy is chosen for this work: A two-phase model of the gas bulks is developed during a student's thesis, while a nonlinear passivity-based control approach is proposed, applied and evaluated at easier one-phase conditions in a first step. For this purpose, a one-phase PEMFC model made up from the detailed and one-phase membrane model from section 2.1 and electrode models like in section 2.3 are chosen. This model includes, as one of few models in the literature, a detailed modeling of the electro-osmotic drag, an important aspect in fuel cell operation that has not been paid much attention in the development of control strategies for PEMFCs up to now. This model is introduced in section 2.4.

In summary, four models are used in this contribution. They are summarized together with the presupposed model assumptions in Fig. 2.1 and will be introduced in more detail and described in the following.

2.1 Detailed two-phase PEMFC model

The presented bifurcation analysis requires a rigorous PEMFC-model that incorporates the flooding/drying out of the cell. The detailed two-phase model is used as basis for the analysis of the water household in chapter 3. For this purpose, a dy-

Figure 2.1: Modelling overview.

namic, one-dimensional (through the plane) and two-phase model from Ziegler [90] is used. This model is slightly modified with respect to the boundary conditions as will be explained below. The model considers a cell sandwich consisting of GDLs, catalyst layers and the membrane (Fig. 2.2). The main model assumptions are:

- The model is isothermal.
- The gas phases are isobaric and behave like ideal gases.
- Transport of hydrogen and water vapor through the GDL and catalyst layer at the anode side is described by a Fick diffusion approach.
- Transport of oxygen and water vapor through the GDL and catalyst layer at the cathode side is described by a Fick diffusion approach.
- Transport of liquid water through the GDLs and catalyst layers at the anode and cathode side follows Darcy's law.
- Transport of water vapor and liquid water as well as electro-osmotic drag of water through the membrane are considered using a model formulation suggested by Weber et al. [77, 78, 79].
- Butler-Volmer kinetics are used at the anode and cathode side.
- Constant gas compositions in the anode and cathode bulk are assumed.

In the following, the model equations and the used boundary conditions are presented. In this modeling context, $\kappa \in \{1,2,3,4,5\}$ is used to specify the modeling domains, e.g. $\kappa = 1$ for the anodic GDL, (see also Fig. 2.2) and $\iota \in \{H_2, O_2, H_2O\}$ is used to denote the different species in the PEMFC.

2.1.1 Charge balances

The electron and the proton potentials are evaluated from the Poisson equation. The electrons are generated by the hydrogen oxidation reaction in the anodic catalyst layer and transported via the anodic gas diffusion layer, the external circuit and the cathodic gas diffusion layer to the catalyst layer at the cathode side. Consequently, the electron potential is calculated in both catalyst and gas diffusion layers and reads with subdomains $\kappa \in \{1,2,4,5\}$:

$$\frac{\partial}{\partial z}\underbrace{\left(-\tilde{\sigma}_\kappa^e \frac{\partial \tilde{\phi}_\kappa^e}{\partial z}\right)}_{\tilde{j}_\kappa^e :=} = \begin{cases} 0 & \text{for} \quad \kappa = 1,5 \\ -\tilde{Q}_a^{ch} & \text{for} \quad \kappa = 2 \\ -\tilde{Q}_c^{ch} & \text{for} \quad \kappa = 4 \end{cases}, \tag{2.1}$$

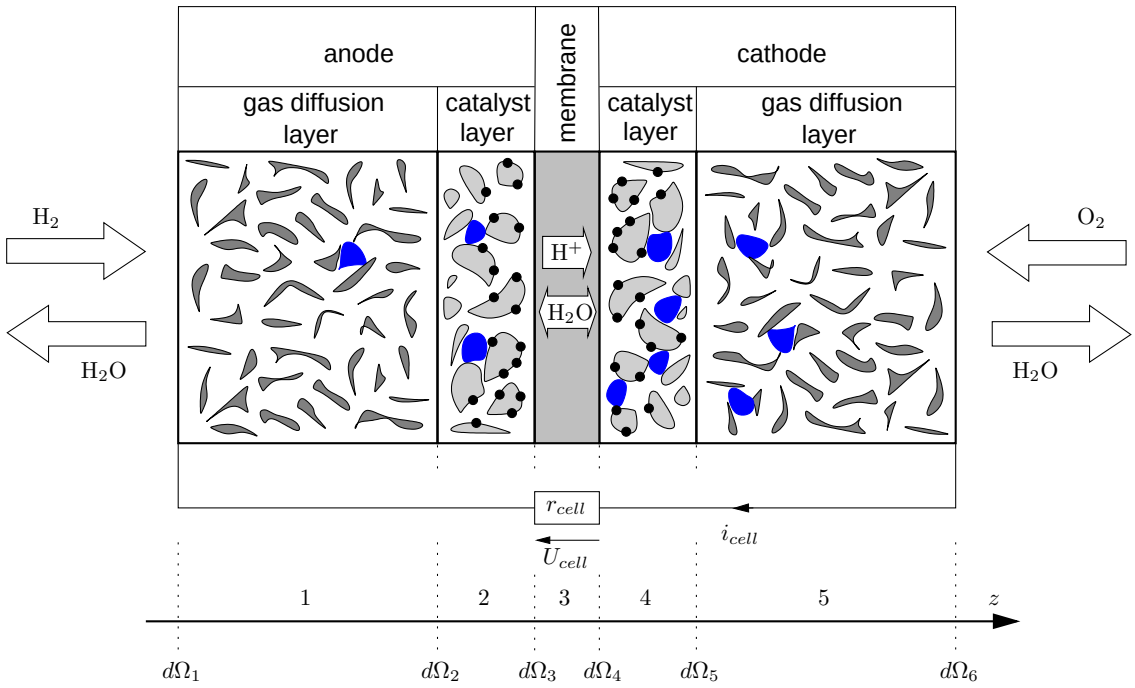

Figure 2.2: Sandwich model of the considered PEMFC consisting of GDLs, catalyst layers and the membrane. Also shown is the modeling direction z, the modeling domains $\kappa \in \{1, 2, 3, 4, 5\}$ and its boundaries $\{d\Omega_1, \ldots, d\Omega_6\}$.

where the following boundary conditions are used:

$$\begin{aligned}
&\tilde{j}^e_\kappa|_{d\Omega_{\kappa+1}} \triangleq \tilde{j}^e_{\kappa+1}|_{d\Omega_{\kappa+1}} \quad \text{and} \quad \tilde{\phi}^e_\kappa|_{d\Omega_{\kappa+1}} \triangleq \tilde{\phi}^e_{\kappa+1}|_{d\Omega_{\kappa+1}} \quad \text{for} \quad \kappa = 1, 4\,; \\
&\tilde{j}^e_2|_{d\Omega_3} \triangleq 0\,; \\
&\tilde{j}^e_4|_{d\Omega 4} \triangleq 0\,; \\
&\tilde{\phi}^e_1|_{d\Omega_1} \triangleq 0 \quad \text{and} \\
&\tilde{\phi}^e_5|_{d\Omega_6} \triangleq U_{cell}\,.
\end{aligned} \tag{2.2}$$

The electrical potential of the carbon phase, in the above charge balance, is denoted with $\tilde{\phi}^e_\kappa$, while the conductivity of this phase is described with $\tilde{\sigma}^e_\kappa$. The source terms $\tilde{Q}^{ch}_a$ and $\tilde{Q}^{ch}_c$ model the electrochemical reactions in the catalyst layer at the anode and cathode side respectively. This is done according to the Butler-Volmer kinetics introduced in Eqn. 2.41 and Eqn. 2.42. The boundary conditions for the charge balance of the electrons are described in Eqn. 2.2. Between the GDLs and the catalyst layers the consistency of the electrical flow and potential of the electrons are demanded, whereas it is assumed that no electrons are entering the membrane. Finally, the potential of the electrons at the PEMFC borders is set to zero and equal to the cell voltage U_{cell} respectively.

The protons are also generated in the anodic catalyst layer, but they are transported through the membrane to the cathodic catalyst. Therefore, the equations for the proton potentials are formulated in both catalyst layers and the membrane and read as follows with $\kappa \in \{2, 3, 4\}$:

$$\frac{\partial}{\partial z} \underbrace{\left(-\tilde{\sigma}^p_\kappa \frac{\partial \tilde{\phi}^p_\kappa}{\partial z} \right)}_{\tilde{j}^p_\kappa :=} = \begin{cases} \tilde{Q}^{ch}_a & \text{for} \quad \kappa = 2 \\ 0 & \text{for} \quad \kappa = 3 \\ \tilde{Q}^{ch}_c & \text{for} \quad \kappa = 4 \end{cases}, \tag{2.3}$$

where the boundary conditions are given by

$$\begin{aligned}
&\tilde{j}^p_\kappa|_{d\Omega_{\kappa+1}} \triangleq \tilde{j}^p_{\kappa+1}|_{d\Omega_{\kappa+1}} \quad \text{and} \quad \tilde{\phi}^p_\kappa|_{d\Omega_{\kappa+1}} \triangleq \tilde{\phi}^p_{\kappa+1}|_{d\Omega_{\kappa+1}} \quad \text{for} \quad \kappa = 2, 3\,; \\
&\tilde{j}^p_2|_{d\Omega_2} \triangleq 0\,; \\
&\tilde{j}^p_4|_{d\Omega_5} \triangleq 0 \quad \text{and} \\
&\tilde{j}^p_2|_{d\Omega_3} \triangleq i_{cell}\,.
\end{aligned} \tag{2.4}$$

The potential of the proton conducting phase in the catalyst layers and the membrane is given by $\tilde{\phi}^p_\kappa$. The corresponding proton conductivity is described by $\tilde{\sigma}^p_\kappa$. The reaction kinetics denoted with $\tilde{Q}^{ch}_a$ and $\tilde{Q}^{ch}_c$ serve as source terms like in the charge balances of the electrons. The boundary conditions in Eqn. 2.4 require both the consistency of the electrical flow and the potential of the protons between the catalyst layers and the membrane. Furthermore, it is modeled that no protons are migrating in the gas diffusion layers. Finally, the last boundary condition secures that the flow of protons through the membrane is equal to the electrical cell current i_{cell} that can be drawn from the fuel cell.

The proton conductivity in the membrane (in S/m) is calculated from the following empirical equation according [78]:

$$\tilde{\sigma}_3^p = \begin{cases} 50\,(\tilde{f}-0.06)^{1.5}\,\exp\left(\frac{15000}{\varrho}\left(\frac{1}{\vartheta_{ref}}-\frac{1}{\vartheta}\right)\right) & \text{for} \quad \tilde{f}\le 0.45 \\ 50\,(0.39)^{1.5}\,\exp\left(\frac{15000}{\varrho}\left(\frac{1}{\vartheta_{ref}}-\frac{1}{\vartheta}\right)\right) & \text{for} \quad \tilde{f}>0.45 \end{cases} . \tag{2.5}$$

The proton conductivity depends on the cell temperature ϑ and the water content in the membrane, that enters in the above equation via the quantity $\tilde{f}$. This quantitiy describes the volume fraction of water in the membrane and is calculated by

$$\tilde{f} = \frac{\tilde{\lambda}\, v_l}{v_m + \tilde{\lambda}\, v_l} , \tag{2.6}$$

where $\tilde{\lambda}$ is the number of water molecules per sulfonic acid group in the membrane [77]. It can be interpreted as the membrane humidity and is determined by Eqn. 2.16. The other quantities in Eqn. 2.6 are the molar volume of water, $v_l = M_{H_2O}/\rho_l$, and the partial molar volume of the dry membrane: $v_m = EW/\rho_m$. Finally, the proton conductivities of the catalyst layers are expressed as the product of the Nafion content in the catalyst layers and the protonic conductivity of the membrane: $\tilde{\sigma}_{2/4}^p = \nu\,\tilde{\sigma}_3^p|_{d\Omega_{3/4}}$.

2.1.2 Balance equations for liquid water

If PEM fuel cells are operated at low temperatures, liquid water is formed inside the cell, in particular in the porous gas diffusion and catalyst layers. The liquid water content inside these layers is modeled with mass balances in the following and reads with $\kappa \in \{1,2,4,5\}$:

$$\pi\rho_l \frac{\partial \tilde{s}_\kappa^l}{\partial t} = -\frac{\partial}{\partial z}\underbrace{\left(-\frac{\rho_l K}{\mu_l}\left(\tilde{s}_\kappa^l\right)^3 \frac{\partial \tilde{p}_\kappa^l}{\partial z}\right)}_{\tilde{j}_\kappa^l :=} + \tilde{Q}_\kappa^l , \tag{2.7}$$

where the boundary conditions are given by

$$\tilde{j}_\kappa^l|_{d\Omega_{\kappa+1}} \triangleq \tilde{j}_{\kappa+1}^l|_{d\Omega_{\kappa+1}} \quad \text{and} \quad \tilde{p}_\kappa^l|_{d\Omega_{\kappa+1}} \triangleq \tilde{p}_{\kappa+1}^l|_{\Omega_{\kappa+1}} \quad \text{for} \quad \kappa = 1,4\,; \tag{2.8a}$$

$$\tilde{j}_2^l|_{d\Omega_3} \triangleq \tilde{j}_{a,m}^l \quad \text{and} \quad \tilde{p}_2^l|_{d\Omega_3} \triangleq \tilde{p}_{a,m}^l\,; \tag{2.8b}$$

$$\tilde{j}_4^l|_{d\Omega_4} \triangleq \tilde{j}_{c,m}^l \quad \text{and} \quad \tilde{p}_3^l|_{d\Omega_4} \triangleq \tilde{p}_{c,m}^l\,; \tag{2.8c}$$

$$\tilde{p}_1^l\big|_{d\Omega_1} \triangleq p_g \quad \text{and} \quad \tilde{p}_5^l\big|_{d\Omega_6} \triangleq p_g\,. \tag{2.8d}$$

The liquid water content in Eqn. 2.7 is described by the liquid water saturation $\tilde{s}_\kappa^l$, which denotes the volume fraction of the pore space in the GDLs and catalyst layers that is filled with liquid water. The first term on the right hand side in this balance equation contains the Darcy law and models the pressure-driven liquid water transport, where $\tilde{p}_\kappa^l$ describes the liquid water pressure. The pressure $\tilde{p}_\kappa^l$ is related

to the saturation $\tilde{s}_\kappa^l$ via Eqn. 2.30 till Eqn. 2.35, a relationship that is introduced later on in detail in subsection 2.1.5. Another important quantity of the Darcy law is the permeability which is given via the absolute permeability K and the relative permeability that is modeled by the term $(s_\kappa^l)^3$ [7, 80]. The second term on the right hand side, $(\tilde{Q}_\kappa^l)$, in Eqn. 2.7 models the kinetics for condensation and vaporization in the PEMFC and is described and introduced in subsection 2.1.6. The other quantities in the balance equation are parameters, like the porosity of the GDLs and the catalyst layers, π, and the density of liquid water ρ_l.

For the calculation of the liquid water mass balance the above boundary conditions are applied. The boundary conditions in Eqn. 2.8a, Eqn. 2.8b and Eqn. 2.8c require the consistency of the liquid water flows and the liquid water pressures between the GDLs and the catalyst layers, and the catalyst layers and the membrane. The boundary conditions in Eqn. 2.8d, where p_g is the gas pressure, are equal to assuming a capillary pressure of zero at the boundaries $d\Omega_1$, $d\Omega_6$. This approach differs from the original model but seems to be physically more justified than the assumption in [90], where the liquid water saturation at the boundaries is set equal to the spatial average along the GDLs.

2.1.3 Balance equations for gas components

Usually PEM fuel cells are fed with hydrogen at the anode side and air at the cathode side. This is also assumed here.

Anode. At the anode side the presence of hydrogen, water vapor and nitrogen is assumed and described by the following mass balances with $\kappa \in \{1, 2\}$ and $\iota \in \{\mathrm{H_2}, \mathrm{H_2O}\}$:

$$\frac{\partial \hat{\tilde{\rho}}_\kappa^\iota}{\partial t} = -\frac{\partial}{\partial z} \underbrace{\left(-\hat{D}_\kappa^\iota \left(1 - \tilde{s}_\kappa^l\right)^2 \frac{\partial \tilde{c}_\kappa^\iota}{\partial z} \right)}_{\tilde{j}_\kappa^\iota :=} + \tilde{Q}_a^g \tag{2.9}$$

$$\text{with} \quad \hat{\tilde{\rho}}_\kappa^\iota := \pi \tilde{\rho}_\kappa^g (1 - \tilde{s}_\kappa^l) \tilde{c}_\kappa^\iota \quad , \quad \hat{D}_\kappa^\iota := \pi \left(\frac{\pi - 0.11}{1 - 0.11} \right)^{0.785} \tilde{\rho}_\kappa^g D_\kappa^\iota$$

$$\text{and} \quad \tilde{Q}_a^g := \begin{cases} -\tilde{Q}_\kappa^l & \text{for} \quad \kappa = 1, 2 \quad \text{and} \quad \iota = \mathrm{H_2O} \\ 0 & \text{for} \quad \kappa = 1 \quad \text{and} \quad \iota = \mathrm{H_2} \\ -\frac{M_{H_2}}{2F} \tilde{Q}_a^{ch} & \text{for} \quad \kappa = 2 \quad \text{and} \quad \iota = \mathrm{H_2} \end{cases} .$$

The boundary conditions read

$$\tilde{j}_1^\iota|_{d\Omega_2} \triangleq \tilde{j}_2^\iota|_{d\Omega_2} \quad \text{and} \quad \tilde{c}_1^\iota|_{d\Omega_2} \triangleq \tilde{c}_2^\iota|_{d\Omega_2} \quad \text{for} \quad \iota = \mathrm{H_2}, \mathrm{H_2O} \, ; \tag{2.10a}$$

$$\tilde{j}_2^{H_2O}|_{d\Omega_3} \triangleq \tilde{j}_{a,m}^{H_2O} \quad \text{and} \quad \tilde{c}_2^{H_2O}|_{d\Omega_3} \triangleq \tilde{c}_{a,m}^{H_2O} \, ; \tag{2.10b}$$

$$\tilde{j}_2^{H_2}|_{d\Omega_3} \triangleq 0 \quad \text{and} \tag{2.10c}$$

$$\tilde{c}_1^\iota|_{d\Omega_1} \triangleq c_{a,b}^\iota \quad \text{for} \quad \iota = \mathrm{H_2}, \mathrm{H_2O} \, . \tag{2.10d}$$

The gas compositions at the anode side are described by the mass fractions $\tilde{c}_\kappa^\iota$ and by the overall gas densities $\tilde{\rho}_\kappa^g$ which are calculated from the ideal gas law

$$\tilde{\rho}_\kappa^g = \frac{\tilde{M}_\kappa p_g}{\varrho \vartheta} \,, \tag{2.11}$$

where the overall molar mass in layer κ is given by

$$\frac{1}{\tilde{M}_\kappa} = \frac{\tilde{c}_\kappa^{H_2}}{M_{H_2}} + \frac{\tilde{c}_\kappa^{H_2O}}{M_{H_2O}} + \frac{1 - \tilde{c}_\kappa^{H_2} - \tilde{c}_\kappa^{H_2O}}{M_{N_2}} \,. \tag{2.12}$$

The first term on the right hand side of Eqn. 2.9 models the diffusive mass transport of the gas components in the PEM fuel cell. It should be noted, that this mass transport is affected by the liquid water saturation $\tilde{s}_\kappa^l$ that models the impeding of the gas transport at an increased liquid water level. The quantities $\tilde{Q}_\kappa^l$ and $\tilde{Q}_a^{ch}$ that appear as source terms in the definition of $\tilde{Q}_a^g$ are already introduced and model the kinetics for condensation/vaporization and the Butler-Volmer kinetics at the anode side respectively. Finally, the parameters D_κ^ι and F describe the binary diffusion coefficient of species ι in layer κ and the Faraday constant.

The boundary conditions for the anodic gas compositions are given in Eqn. 2.10. The conditions in Eqn. 2.10a secure the continuity of the water vapor and hydrogen flows as well as the water vapor and the hydrogen content between the anodic catalyst layer and the GDL. In Eqn. 2.10b the same consistency is also assured for water vapor between the catalyst layer and the membrane, while in Eqn. 2.10c no crossover of hydrogen from the anode to the cathode side is assumed. Finally, in Eqn. 2.10d the water vapor and the hydrogen content at the left boundary of the anodic GDL are assumed to be equal to the gas composition in the anodic gas bulk, which is described by the mass fractions $c_{a,b}^\iota$.

Cathode. At the cathode side of the PEMFC, air made up from oxygen, nitrogen and water vapor is considered. Similar to the anode side, the gas compositions at the cathode are modeled by the following mass balances with $\kappa = 4, 5$ and $i = \mathrm{O}_2, \mathrm{H}_2\mathrm{O}$:

$$\frac{\partial \hat{\tilde{\rho}}_\kappa^\iota}{\partial t} = -\frac{\partial}{\partial z} \underbrace{\left(-\hat{D}_\kappa^\iota (1 - \tilde{s}_\kappa^l)^2 \frac{\partial \tilde{c}_\kappa^\iota}{\partial z} \right)}_{\tilde{j}_\kappa^\iota :=} + \tilde{Q}_c^g \tag{2.13}$$

$$\text{with} \quad \hat{\tilde{\rho}}_\kappa^\iota := \pi \tilde{\rho}_\kappa^g (1 - \tilde{s}_\kappa^l) \tilde{c}_\kappa^\iota \quad , \quad \hat{D}_\kappa^\iota := \pi \left(\frac{\pi - 0.11}{1 - 0.11} \right)^{0.785} \tilde{\rho}_\kappa^g D_\kappa^\iota$$

$$\text{and} \quad \tilde{Q}_c^g := \begin{cases} -\tilde{Q}_\kappa^l - \frac{M_{H_2O}}{2F} \tilde{Q}_c^{ch} & \text{for} \quad \kappa = 4 \quad \text{and} \quad \iota = \mathrm{H}_2\mathrm{O} \\ \frac{M_{O_2}}{4F} \tilde{Q}_c^{ch} & \text{for} \quad \kappa = 4 \quad \text{and} \quad \iota = \mathrm{O}_2 \\ -\tilde{Q}_\kappa^l & \text{for} \quad \kappa = 5 \quad \text{and} \quad \iota = \mathrm{H}_2\mathrm{O} \\ 0 & \text{for} \quad \kappa = 5 \quad \text{and} \quad \iota = \mathrm{O}_2 \end{cases} .$$

The boundary conditions are given by:

$$\tilde{j}_4^{\iota}|_{d\Omega_5} \triangleq \tilde{j}_5^{\iota}|_{d\Omega_5} \quad \text{and} \quad \tilde{c}_4^{\iota}|_{d\Omega_5} \triangleq \tilde{c}_5^{\iota}|_{d\Omega_5} \quad \text{for} \quad \iota = \mathrm{O_2}, \mathrm{H_2O}\,; \tag{2.14a}$$

$$\tilde{j}_4^{H_2O}|_{d\Omega_4} \triangleq \tilde{j}_{c,m}^{H_2O} \quad \text{and} \quad \tilde{c}_4^{H_2O}|_{d\Omega_4} \triangleq \tilde{c}_{c,m}^{H_2O}\,; \tag{2.14b}$$

$$\tilde{j}_4^{O_2}|_{d\Omega_4} \triangleq 0 \quad \text{and} \tag{2.14c}$$

$$\tilde{c}_5^{\iota}|_{d\Omega_6} \triangleq c_{c,b}^{\iota} \quad \text{for} \quad \iota = \mathrm{O_2}, \mathrm{H_2O}\,. \tag{2.14d}$$

The content of oxygen and water vapor in the cathodic GDL and catalyst layer is described by the mass fractions $\tilde{c}_\kappa^\iota$. Like at the anode side, the density of the gas mixture is given by $\tilde{\rho}_\kappa^g$ and calculated from the ideal gas law in Eqn. 2.11, where the overall molar mass is now given by

$$\frac{1}{\tilde{M}_\kappa} = \frac{\tilde{c}_\kappa^{O_2}}{M_{O_2}} + \frac{\tilde{c}_\kappa^{H_2O}}{M_{H_2O}} + \frac{1 - \tilde{c}_\kappa^{O_2} - \tilde{c}_\kappa^{H_2O}}{M_{N_2}}\,. \tag{2.15}$$

The boundaries of the cathodic gas compositions are formulated in Eqn. 2.14 in an analogous manner like at the anode side. The conditions in Eqn. 2.14a and Eqn. 2.14b are used to guarantee the consistency of water vapor and oxygen between the cathodic gas diffusion layer, the catalyst layer and the membrane. Correspondingly to the anode, no crossover of oxygen is assumed in Eqn. 2.14c, while the gas composition at the right boundary of the GDL is set to the gas composition in the gas bulk described by the mass fractions $c_{c,b}^\iota$.

2.1.4 Water balance equation in the membrane

The membrane is modeled according to the approach from Weber [77, 78, 79]. This model is a dynamical and distributed one and considers the transport of liquid water and water vapor through the membrane. It can be formulated by using a total water balance in the membrane that reads:

$$\frac{\rho_m}{EW}\frac{\partial \tilde{\lambda}}{\partial t} = -\frac{\partial}{\partial z}\tilde{N}_{H_2O}\,, \tag{2.16}$$

where $\tilde{\lambda}$ describes the membrane humidity, ρ_m denotes the density and EW stands for the equivalent weight of the dry membrane. The overall flux of water transported through the membrane is denoted with $\tilde{N}_{H_2O}$ and is determined from the following equation:

$$\begin{aligned}\tilde{N}_{H_2O} =& \tilde{S}\left[-\left(\tilde{\alpha}_l + \frac{\tilde{\sigma}_3^p \xi_l^2}{F^2}\right) v_l \frac{\partial \tilde{p}_3^{cp}}{\partial z} - \frac{\tilde{\sigma}_3^p \xi_l}{F}\frac{\partial \tilde{\phi}_3^p}{\partial z}\right] \\ &+ (1-\tilde{S})\left[-\left(\tilde{\alpha}_g + \frac{\tilde{\sigma}_3^p \xi_g^2}{F^2}\right)\frac{\partial \tilde{\varpi}_3^{H_2O}}{\partial z} - \frac{\tilde{\sigma}_3^p \xi_g}{F}\frac{\partial \tilde{\phi}_3^p}{\partial z}\right]\,.\end{aligned} \tag{2.17}$$

It can be seen that the total water flux inside the membrane results from a superposition between the transport of liquid water given in the first bracket and the

transport of water vapor in the second bracket. The superposition is done via the quantity $\tilde{S}$, the fraction of expanded channels [77] in the membrane. In the given membrane model it is assumed that the presence of liquid water leads to a structural change in the membrane that forms liquid water channels inside. The quantity $\tilde{S}$ is used to describe the fraction of those channels and depends on the membrane humidity:

$$\tilde{S} = \begin{cases} 0 & \text{for} \quad 0 \leq \tilde{\lambda} < \lambda_g^{max} \\ \frac{\tilde{\lambda} - \lambda_g^{max}}{\lambda_l^{max} - \lambda_g^{max}} & \text{for} \quad \lambda_g^{max} \leq \tilde{\lambda} \leq \lambda_l^{max} \end{cases} , \tag{2.18}$$

where λ_g^{max} and λ_l^{max} are the maximum stationary humidity values of a membrane in contact with saturated vapor and with liquid water respectively.

The transport of liquid water through the membrane is established by two effects. First of all, liquid water is transport through the membrane by means of the liquid water pressure $\tilde{p}_3^{cp}$. This effect is given as the first term inside the first bracket of Eqn. 2.17. Liquid water can also be carried through the membrane by the protonic current directed from the anode to the cathode and driven by the proton potential $\tilde{\phi}_3^p$. This effect is also known as the electro-osmotic drag and is described by the second term in the first bracket of Eqn. 2.17.

The liquid water pressure in the membrane $\tilde{p}_3^{cp}$ can be described with capillary forces. It is assumed that the formation of liquid water channels inside the membrane can be treated as a bundle of capillaries and the well-known Laplace equation can be used to determine the liquid water pressure there:

$$\tilde{p}_3^{cp} = -\frac{2\,\sigma_{H_2O}\,cos\theta_3}{\tilde{\mathfrak{r}}} . \tag{2.19}$$

In the above equation, the quantity σ_{H_2O} and θ_3 denote the surface tension and contact angle of water inside the membrane. The surface tension (in N/m) can be calculated from

$$\sigma_{H_2O} = B_1 \left(1 - \frac{\vartheta}{\vartheta_c}\right)^{1.256} \left(1 + B_2 \left(1 - \frac{\vartheta}{\vartheta_c}\right)\right) \tag{2.20}$$

with $B_1 = 0.235\ N/m$, $B_2 = -0.625$ and $\vartheta_c = 647.096\ K$. The radius of the liquid water channels $\tilde{\mathfrak{r}}$ (in m) can be determined from the channel size distribution [78], where a successive integration leads to the fraction of expanded channels:

$$\tilde{S} = \frac{1}{2}\left(1 - \mathrm{erf}\left(\frac{\ln(10^9\,\tilde{\mathfrak{r}}) - \ln(1.25)}{0.3\sqrt{2}}\right)\right) , \tag{2.21}$$

with erf() denoting the error function. The description of the liquid water transport through the membrane given in the first bracket of Eqn. 2.17 is completed by the statement of the belonging transport coefficients. Besides the already introduced proton conductivity $\tilde{\sigma}_3^p$ (Eqn. 2.5) and the molar volume of water v_l, there are still

two unknown quantities in there: $\tilde{\alpha}_l$ and ξ_l, which are given by the relations

$$\tilde{\alpha}_l = \frac{K_m}{\mu_l v_l^2} \left(\frac{\tilde{f}}{f_l} \right)^2 \tag{2.22}$$

$$\text{and} \quad \xi_l = 2.55 \exp\left(\frac{4000}{\varrho} \left(\frac{1}{\vartheta_{ref}} - \frac{1}{\vartheta} \right) \right) . \tag{2.23}$$

In the previous two equations, the variables $\tilde{f}$ and $\tilde{f}_l$ denote the volume fraction of water in the membrane given in Eqn. 2.6 and its maximum value $f_l := \tilde{f}(\tilde{\lambda}_l^{max})$. The other quantities in the above equations are the already mentioned molar volume of water v_l, the absolute permeability of the membrane K_m, the viscosity of liquid water μ_l, the cell temperature ϑ and the ideal gas constant ϱ.

Besides liquid water, water vapor is also transported through the membrane. This transport is realized by two effects as can be seen from the second bracket in Eqn. 2.17. The first effect is concentration-driven by the electrochemical potential of water $\tilde{\varpi}_3^{H_2O}$, while the second effect is given by the electro-osmotic drag. The electrochemical potential $\tilde{\varpi}_3^{H_2O}$ is related to $\tilde{a}_3^{H_2O}$, the activity of water vapor in the membrane, by the following equation:

$$\tilde{\varpi}_3^{H_2O} = \varrho \vartheta \ln(\tilde{a}_3^{H_2O}) . \tag{2.24}$$

The activity itself can be calculated from the membrane humidity $\tilde{\lambda}$ given in Eqn. 2.16. For a membrane in contact with water vapor only, i.e. $0 \leq \tilde{\lambda} < \lambda_g^{max}$, the activity is related to the membrane humidity via the model from Springer [70]:

$$\tilde{\lambda} = 0.043 + 17.81 \tilde{a}_3^{H_2O} - 39.85 (\tilde{a}_3^{H_2O})^2 + 36 (\tilde{a}_3^{H_2O})^3 . \tag{2.25}$$

On the other side, if the membrane is in contact with liquid water, i.e. $\lambda_g^{max} \leq \tilde{\lambda} \leq \lambda_l^{max}$, an activity of one is used instead: $\tilde{a}_3^{H_2O} = 1$. The description of the transport of water vapor is accomplished by the designation of the transport coefficients. There are only two unknown ones present in the second bracket of Eqn. 2.17: $\tilde{\alpha}_g$ and ξ_g. They depend both on the membrane humidity and read

$$\tilde{\alpha}_g = \frac{\rho_m}{\varrho \, \vartheta \, EW} \, \tilde{\lambda} \, (\tilde{\lambda} + 1) \, \tilde{D}_m^{H_2O} \tag{2.26}$$

$$\text{with} \quad \tilde{D}_m^{H_2O} = 1.8 \cdot 10^{-9} \, \tilde{f} \exp\left(\frac{20000}{\varrho} \left(\frac{1}{\vartheta_{ref}} - \frac{1}{\vartheta} \right) \right) \quad \text{in } m^2/s \tag{2.27}$$

$$\text{and} \quad \xi_g = \begin{cases} \tilde{\lambda} & \text{for} \quad \tilde{\lambda} < 1 \\ 1 & \text{for} \quad \tilde{\lambda} \geq 1 \end{cases} . \tag{2.28}$$

Finally, the following boundary conditions are used for the calculation of the membrane humidity in Eqn. 2.16:

$$\tilde{N}_{H_2O}|_{d\Omega_3} \triangleq \frac{1}{M_{H_2O}} \left(\tilde{j}_{a,m}^{l} + \tilde{j}_{a,m}^{H_2O} \right) , \tag{2.29a}$$

$$\tilde{N}_{H_2O}|_{d\Omega_4} \triangleq \frac{1}{M_{H_2O}} \left(\tilde{j}_{c,m}^{l} + \tilde{j}_{c,m}^{H_2O} \right) , \tag{2.29b}$$

$$\tilde{p}_3^{cp}|_{d\Omega_3} \triangleq \tilde{p}_{a,m}^{l} - p_g , \tag{2.29c}$$

$$\tilde{p}_3^{cp}|_{d\Omega_4} \triangleq \tilde{p}_{c,m}^{l} - p_g \,, \tag{2.29d}$$

$$\tilde{a}_3^{H_2O}|_{d\Omega_3} \triangleq \frac{p_g}{p_{sat}} \frac{\tilde{M}_2|_{d\Omega_3}}{M_{H_2O}} \, \tilde{c}_{a,m}^{H_2O} \quad \text{and} \tag{2.29e}$$

$$\tilde{a}_3^{H_2O}|_{d\Omega_4} \triangleq \frac{p_g}{p_{sat}} \frac{\tilde{M}_4|_{d\Omega_4}}{M_{H_2O}} \, \tilde{c}_{c,m}^{H_2O} \,. \tag{2.29f}$$

Equations 2.29a and 2.29b secure the continuity of the liquid and gaseous water flow between the catalyst layers and the membrane, while in Eqn. 2.29c till Eqn. 2.29f the consistency of the liquid water pressure and the water activity between the catalyst layers and the membrane is assured.

2.1.5 Liquid water pressure

For the modeling of the liquid water pressures in the catalyst and the gas diffusion layers, the capillary effect must be taken into account due to the small pore sizes there. In this contribution, the liquid water pressure is related to the capillary pressure by

$$\tilde{p}_\kappa^l = p_g - \tilde{p}_\kappa^{cp} \quad \text{for} \quad \kappa \in \{1, 2, 4, 5\} \,, \tag{2.30}$$

where the quantity p_g describes the constant pressure of the gas phase. The capillary pressure $\tilde{p}_\kappa^{cp}$ itself depends on the liquid water saturation. For its determination the original model from [90] is extended. It is assumed, that the GDLs and catalyst layers may contain hydrophilic as well as hydrophobic pores. This aspect is modeled by introducing an additional parameter, f_{HI}, which denotes the fraction of hydrophilic pores and allows to study the influence of the hydrophilic/hydrophobic pore ratio on the water household of the fuel cell. The parameter f_{HI} is assumed to be the same in both GDLs and catalyst layers. With this parameter, the liquid water saturation can be subdivided in the saturation of the hydrophobic pores, denoted with $\tilde{s}_\kappa^{l,HO}$, and the saturation of the hydrophilic pores denoted with $\tilde{s}_\kappa^{l,HI}$ [80]:

$$\tilde{s}_\kappa^l = f_{HI} \tilde{s}_\kappa^{l,HI} + (1 - f_{HI}) \tilde{s}_\kappa^{l,HO} \,. \tag{2.31}$$

The liquid water saturations of hydrophilic and hydrophobic pores are related to the same capillary pressure by:

$$\tilde{p}_\kappa^{cp} = \sigma_{H_2O} \, cos(\theta_{HI}) \, \sqrt{\frac{\pi}{K}} \, \tilde{J}_{HI}(\tilde{s}_\kappa^{l,HI}) \quad \text{and} \tag{2.32}$$

$$\tilde{p}_\kappa^{cp} = \sigma_{H_2O} \, cos(\theta_{HO}) \, \sqrt{\frac{\pi}{K}} \, \tilde{J}_{HO}(\tilde{s}_\kappa^{l,HO}) \,, \tag{2.33}$$

where θ_{HI} and θ_{HO} are the contact angles of the hydrophilic and hydrophobic pores and are assumed to be the same in the GDLs and catalyst layers. This is also the case for the porosity π, the permeability K and the surface tension of water σ_{H_2O}

that are used for both types of pores. The equations for the capillary pressure above are completed by the Leverett functions for hydrophilic and hydrophobic pores [90]:

$$\tilde{J}_{HI}(\tilde{s}_\kappa^{l,HI}) = 1.417(1-\tilde{s}_\kappa^{l,HI}) - 2.120(1-\tilde{s}_\kappa^{l,HI})^2 + 1.263(1-\tilde{s}_\kappa^{l,HI})^3\,, \tag{2.34}$$

$$\tilde{J}_{HO}(\tilde{s}_\kappa^{l,HO}) = 1.417\tilde{s}_\kappa^{l,HO} - 2.120(\tilde{s}_\kappa^{l,HO})^2 + 1.263(\tilde{s}_\kappa^{l,HO})^3\,. \tag{2.35}$$

Equations 2.31 till Eqn. 2.35 can now be used to calculate the capillary pressure $\tilde{p}_\kappa^{cp}$ and the liquid water saturations of the hydrophilic and hydrophobic pores, i.e. $\tilde{s}_\kappa^{l,HI}$ and $\tilde{s}_\kappa^{l,HO}$ respectively. The above equations are illustrated in Fig. 2.3, where the liquid water saturation is shown as a function of the liquid water pressure for different values of f_{HI}. The liquid water saturation at a liquid water pressure of p_g

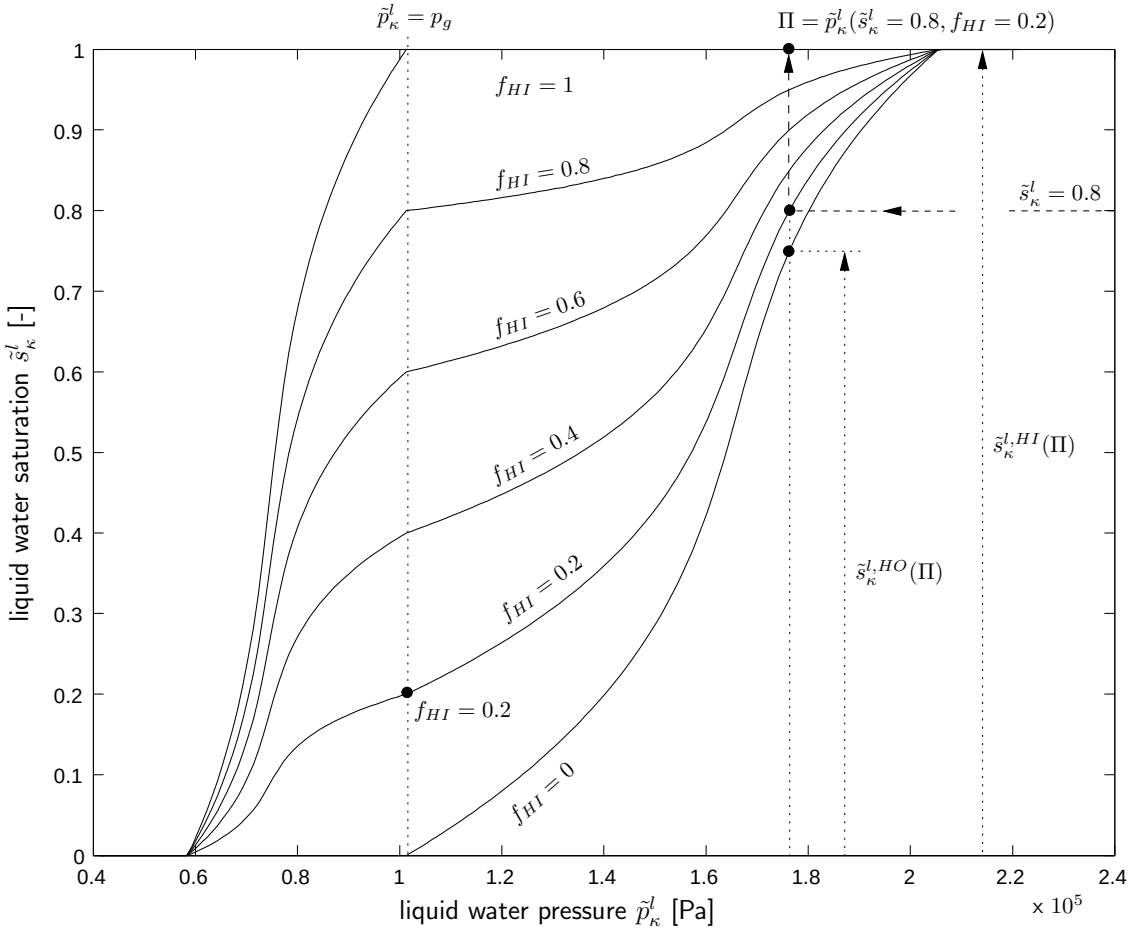

Figure 2.3: Liquid water saturation as function of the liquid water pressure for different values of f_{HI}. The diagram also shows exemplarily the corresponding liquid water pressure Π, the liquid water saturations of the hydrophilic and hydrophobic pores $\tilde{s}_\kappa^{l,HI}$ and $\tilde{s}_\kappa^{l,HO}$ for an overall liquid water saturation $\tilde{s}_\kappa^l = 0.8$ and a fraction of hydrophilic pores $f_{HI} = 0.2$ in the cell.

is called the residual saturation and denotes the liquid water that is trapped in the

hydrophilic pores. This residual saturation cannot be removed from the cell during fuel cell operation and is equal to the respective value of f_{HI}.

The variation of f_{HI} has a strong effect on the liquid water flow out of the cell, as will be explained in the following. From Eqn. 2.8d and Eqn. 2.30 follows that the capillary pressure on the outer surfaces of the GDLs is zero. The corresponding liquid water saturations $\tilde{s}_1^l|_{d\Omega_1}$ and $\tilde{s}_5^l|_{d\Omega_6}$ are obtained by setting the left hand side of Eqn. 2.32 and Eqn. 2.33 to zero and inserting the results in Eqn. 2.31. This results in $\tilde{s}_1^l|_{d\Omega_1} = \tilde{s}_5^l|_{d\Omega_6} = f_{HI}$. Therefore, the liquid water flows out of the cell, $\tilde{j}_1^l|_{d\Omega_1}$ and $\tilde{j}_5^l|_{d\Omega_6}$, which are given by Eqn. 2.7, depend on f_{HI}:

$$\tilde{j}_1^l|_{d\Omega_1} = -\frac{\rho_l K}{\mu_l}\left(\tilde{s}_1^l|_{d\Omega_1}\right)^3 \left.\frac{\partial \tilde{p}_1^l}{\partial z}\right|_{d\Omega_1} = -\frac{\rho_l K}{\mu_l}\left(f_{HI}\right)^3 \left.\frac{\partial \tilde{p}_1^l}{\partial z}\right|_{d\Omega_1} , \tag{2.36}$$

$$\tilde{j}_5^l|_{d\Omega_6} = -\frac{\rho_l K}{\mu_l}\left(\tilde{s}_5^l|_{d\Omega_6}\right)^3 \left.\frac{\partial \tilde{p}_5^l}{\partial z}\right|_{d\Omega_6} = -\frac{\rho_l K}{\mu_l}\left(f_{HI}\right)^3 \left.\frac{\partial \tilde{p}_5^l}{\partial z}\right|_{d\Omega_6} . \tag{2.37}$$

In the case of $f_{HI} = 0$, i.e. purely hydrophobic GDLs, the liquid water flow from the cell is zero. This means that liquid water can only leave the fuel cell by vaporization in the outer parts of the GDLs. If the fraction of hydrophilic pores is increased, i.e. $f_{HI} > 0$, a rising (absolute) value of the liquid water flows $\tilde{j}_1^l|_{d\Omega_1}$ and $\tilde{j}_5^l|_{d\Omega_6}$ is established. For this case, water can leave the cell in vapor or in liquid form.

2.1.6 Kinetics for condensation and vaporization

Besides the electrochemical reaction kinetics in the PEMFC, there are also explicit kinetics for condensation and vaporization in the catalyst and the gas diffusion layers considered. They read with $\kappa \in \{1, 2, 4, 5\}$:

$$\tilde{Q}_\kappa^l = \begin{cases} k_{con}\,\pi\,(1-\tilde{s}_\kappa^{l,HO})\,\frac{M_{H_2O}}{\varrho^\vartheta}\left(\tilde{p}_\kappa^{H_2O} - p_{sat}\right) & \text{for} \quad \tilde{p}_\kappa^{H_2O} > p_{sat} \\ k_{vap}\,\pi\,\tilde{s}_\kappa^{l,HO}\,\rho_l\left(\tilde{p}_\kappa^{H_2O} - p_{sat}\right) & \text{for} \quad \tilde{p}_\kappa^{H_2O} < p_{sat} \end{cases} , \tag{2.38}$$

where $\tilde{p}_\kappa^{H_2O}$ denotes the partial pressure of water vapor that can be calculated from

$$\tilde{p}_\kappa^{H_2O} = p_g \frac{\tilde{M}_\kappa}{M_{H_2O}} \tilde{c}_\kappa^{H_2O} . \tag{2.39}$$

The saturation pressure of water vapor, p_{sat} (in Pa), depends on the cell temperature, ϑ (in K), and is given from the relation [90]:

$$\log(p_{sat}) = 8.07 - \frac{1656.39}{226.86 + \vartheta - 273.15} + 2 . \tag{2.40}$$

2.1.7 Reaction kinetics

The electrochemical reactions in the catalyst layers at the anode and the cathode side of the fuel cell are described by the Butler-Volmer kinetics. They are given by:

$$\tilde{Q}^a_{ch} = \gamma\, i_a\, (1-\tilde{s}^l_2) \left(\frac{\tilde{c}^{H_2}_2}{c^{H_2}_{ref}}\right) \left(\exp\left(\frac{(1-\varphi_a)\zeta_a F}{\varrho\vartheta}\tilde{\eta}_a\right) - \exp\left(-\frac{\varphi_a\zeta_a F}{\varrho\vartheta}\tilde{\eta}_a\right)\right) , \quad (2.41)$$

$$\tilde{Q}^c_{ch} = \gamma\, i_c\, (1-\tilde{s}^l_4) \left(\frac{\tilde{c}^{O_2}_4}{c^{O_2}_{ref}}\right) \left(\exp\left(\frac{(1-\varphi_c)\zeta_c F}{\varrho\vartheta}\tilde{\eta}_c\right) - \exp\left(-\frac{\varphi_c\zeta_c F}{\varrho\vartheta}\tilde{\eta}_c\right)\right) . \quad (2.42)$$

The kinetics are driven by the overvoltage in the catalyst layers. At the anode side, the overvoltage is given by $\tilde{\eta}_a = \tilde{\phi}^e_2 - \tilde{\phi}^p_2$, while at the cathode side it is given by $\tilde{\eta}_c = \tilde{\phi}^e_4 - \tilde{\phi}^p_4 - \Delta\phi_{eq}$, where $\Delta\phi_{eq}$ is the equilibrium potential there. The Butler-Volmer kinetics are also affected by the hydrogen and oxygen content in the anodic and cathodic catalyst layer, i.e. $\tilde{c}^{H_2}_2$ and $\tilde{c}^{O_2}_4$. Finally, the liquid water saturations $\tilde{s}^l_2$ and $\tilde{s}^l_4$ play also an important role in the kinetics and model the covering of the reaction sites with liquid water. The other quantities are constant model parameters.

2.1.8 Numerical solution

In summary, the used PEMFC-model consists of 13 parabolic partial differential equations, 7 ordinary differential equations in space and additional algebraic equations. The operating condition of the PEMFC model is determined by the model constants and nominal model parameters that are given in Table 2.1.

Table 2.1: Used parameter values and constants.

Quantity	**Value**
equilibrium potential of the cathodic reaction, $\Delta\phi_{eq}$	$1.229\ V$
charge transfer coefficient at anode, φ_a	0.5
charge transfer coefficient at cathode, φ_c	0.5
active surface area of catalyst per unit volume, γ	$1.1 \cdot 10^7\ 1/m$
max. membrane humidity for vapor-eq. membrane, λ_g^{max}	14
max. membrane humidity for liquid-eq. membrane, λ_l^{max}	22
viscosity of water (at ϑ), μ_l	$3.56 \cdot 10^{-4}\ Pa\,s$
Nafion content in catalyst layers, ν	0.4
porosity of catalyst layers and GDLs, π	0.4
density of liquid water (at ϑ), ρ_l	$995.56\ kg/m^3$
density of the dry membrane, ρ_m	$1980\ kg/m^3$
conductivity of the carbon phase, $\tilde{\sigma}^e_{1/5}$	$1400\ S/m$
conductivity of the proton conducting phase, $\tilde{\sigma}^e_{2/4}$	$300\ S/m$
cell temperature, ϑ	$313\ K$

continued ...

Quantity	**Value**
reference temperature, ϑ_{ref}	298 K
contact angle of hydrophilic pores, θ_{HI}	80 deg
contact angle of hydrophobic pores, θ_{HO}	115 deg
contact angle of water in the membrane, θ_3	90.02 deg
no. of exchanged electrons at anodic reaction, ζ_a	2
no. of exchanged electrons at cathodic reaction, ζ_c	2
reference hydrogen content, $c_{ref}^{H_2}$	1
reference oxygen content, $c_{ref}^{O_2}$	1
mass fraction of H_2 in anode bulk, $c_{a,b}^{H_2}$	0.5
mass fraction of H_2O in anode bulk, $c_{a,b}^{H_2O}$	0.3
mass fraction of O_2 in cathodic bulk, $c_{c,b}^{O_2}$	0.15
mass fraction of H_2O in cathodic bulk, $c_{c,b}^{H_2O}$	0.045
binary diffusion coefficient of H_2, $D_{1/2}^{H_2}$	$3.5 \cdot 10^{-5}\ m^2/s$
binary diffusion coefficient of H_2O, $D_{1/2/4/5}^{H_2O}$	$2.2 \cdot 10^{-5}\ m^2/s$
binary diffusion coefficient of O_2, $D_{4/5}^{O_2}$	$1.8 \cdot 10^{-5}\ m^2/s$
thickness of the membrane, d_m	$25 \cdot 10^{-6}\ m$
thickness of catalyst layers, d_{catl}	$10 \cdot 10^{-6}\ m$
thickness of gas diffusion layers, d_{gdl}	$300 \cdot 10^{-6}\ m$
equivalent weight of the dry membrane, EW	0.909 kg/mol
fraction of hydrophilic pores, f_{HI}	0
anodic exchange current density, i_a	$1 \cdot 10^{3}\ A/m^2$
cathodic exchange current density, i_c	$1 \cdot 10^{-3}\ A/m^2$
absolute permeability of catalyst layers and GDLs, K	$1 \cdot 10^{-14}\ m^2$
absolute permeability of the membrane, K_m	$1.8 \cdot 10^{-18}\ m^2$
condensation rate of H_2O, k_{con}	$1 \cdot 10^{4}\ 1/s$
evaporation rate of H_2O, k_{vap}	$5.1 \cdot 10^{-5}\ 1/Pa\,s$
molar mass of water, M_{H_2O}	0.018 kg/mol
molar mass of hydrogen, M_{H_2}	0.002 kg/mol
molar mass of nitrogen, M_{N_2}	0.028 kg/mol
molar mass of oxygen, M_{O_2}	0.032 kg/mol
overall gas pressure, p_g	$1.013 \cdot 10^{5}\ Pa$

The model is decomposed into components, the GDLs, the catalyst layers and the membrane, and coupling elements according to [53] and is discretized with an equidistant grid using the method of finite volume elements. The resulting model consists of 130 dynamic and 413 algebraic states. The implementation is done in ProMoT [73] and the simulations and parameter continuations are performed with DIVA [52].

2.2 Reduced two-phase PEMFC model

In the following the reduced two-phase model is presented and derived from the detailed model in section 2.1 by means of simplifying physical assumptions. The model reduction in this work is split into two parts. In chapter 4 the comparison between the detailed and the reduced model is done, while the model equations itself are presented and explained here in order to summarize all models being used in this work in the present chapter. The reduced model can be described as a dynamic, 0-dimensional and two-phase model approach. The changes compared to the detailed model assumptions in section 2.1 are:

- Negligible resistance for the transport of hydrogen through the GDL and catalyst layer at the anode side. The hydrogen content at the anode side is assumed to be constant and equal to the content in the anodic bulk.
- No transport of water vapor as well as no electro-osmotic drag of water vapor through the membrane.
- The anodic reaction is in equilibrium and the anodic overpotential is equal to zero.
- The spatial distribution of GDLs, catalyst layers and the membrane is neglected due to its relative small influence on the simulation results. Moreover, the modelling of the catalyst and gas diffusion layers at the anode and cathode side is lumped together.
- Dynamic effects in the membrane are no longer considered. The membrane's properties, e.g. membrane humidity, are calculated from states at the anode or cathode side.

Between the bulks and the anode side there is a transport of water vapor and liquid water. This is also the case at the cathode side, where additionally the transport of oxygen is considered. Finally, the anode and cathode exchange liquid water across the membrane with each other. In Fig. 2.4 a sketch of this modelling approach is shown.

In the following the model equations are presented. The equations are organized in six subsections. First of all, the mass balances for the liquid water and the gas components together with the explanations of the main source terms are given in subsection 2.2.1 and subsection 2.2.2 respectively. In subsection 2.2.3 the equations for the reaction kinetics, the calculation of the cell voltage and the membrane conductivity are presented. After that, the modeling approach for the membrane humidity is presented in subsection 2.2.4. Finally, the calculation of the liquid water pressure and the condensation and vaporization kinetics are addressed in subsection 2.2.5. The description of the reduced model ends with subsection 2.2.6, where the operating conditions of the fuel cell model are explained and some remarks about the numerical solution are stated. For a derivation of the balance equations please see Appendix A.1. For an additional description of the appearing quantities and

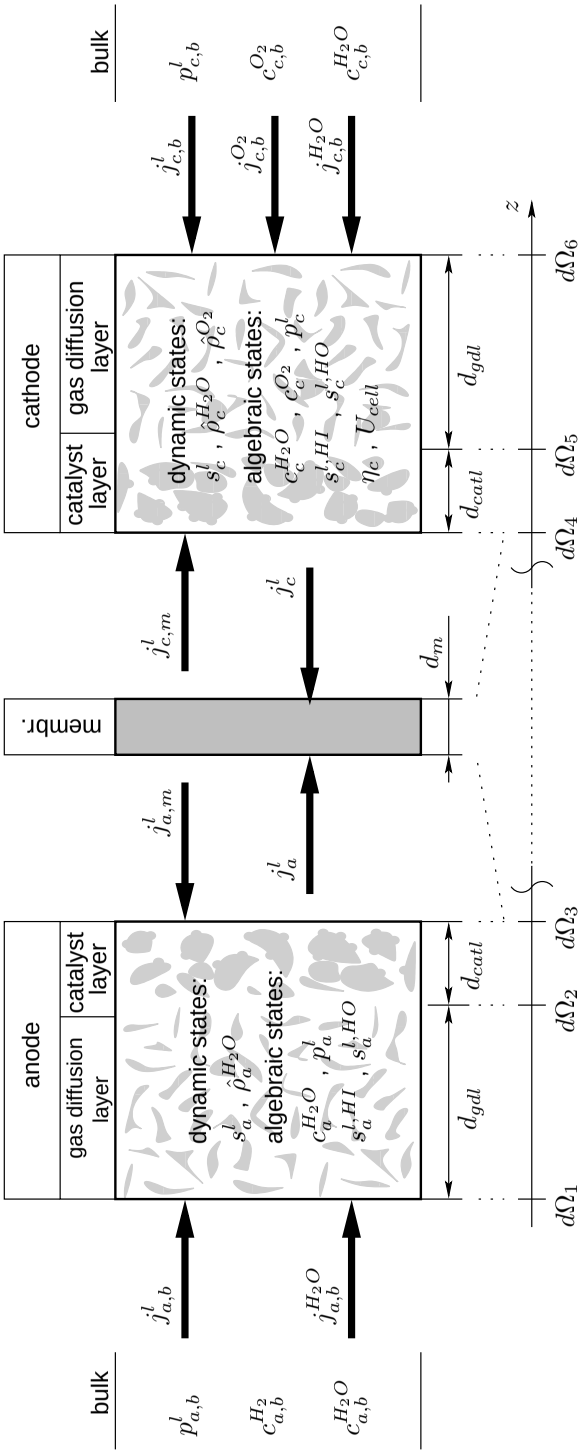

Figure 2.4: Modelling approach of the reduced PEMFC model.

their values and units please see also the list of symbols at the beginning of this work.

2.2.1 Balance of liquid water

Mass balances for the liquid water content are derived at the anode and at the cathode side. With $\epsilon \in \{a, c\}$ they read:

$$\pi \rho_l \frac{ds_\epsilon^l}{dt} = \frac{1}{d_{gdl} + d_{catl}} \left(j_{\epsilon,m}^l + j_{\epsilon,b}^l \right) + Q_\epsilon^l \,. \tag{2.43}$$

The average liquid water saturation at the anode or cathode side is denoted by s_ϵ^l, and the averaged source term due to condensation and vaporization is given by Q_ϵ^l, and calculated according to subsection 2.2.5. The hydraulic transport of liquid water from the gas bulks to the electrodes is described by $j_{\epsilon,b}^l$. This mass flow is modeled with Darcy's law and is given by:

$$j_{\epsilon,b}^l = \begin{cases} -\frac{\rho_l K}{\mu_l} \left(f_{HI}\right)^3 \frac{p_\epsilon^l - p_{\epsilon,b}^l}{\beta_l (d_{gdl} + d_{catl})} & \text{for} \quad p_\epsilon^l > p_{\epsilon,b}^l \\ 0 & \text{for} \quad p_\epsilon^l \leq p_{\epsilon,b}^l \end{cases} \,. \tag{2.44}$$

The average liquid water pressures in the electrodes and the bulks are denoted by p_ϵ^l and $p_{\epsilon,b}^l$ respectively, while the fitting parameter β_l is used for the approximation of the pressure gradient. Please see Appendix A.2 for details about its determination. The hydraulic transport of water depends on the liquid water pressure which on the other hand depends on the capillary pressure. In the reduced model, the same relation between liquid water pressure and capillary is used as in the detailed model. It is given according to subsection 2.2.5. In agreement with the detailed model a capillary pressure of zero is assumed in the bulks. Therefore, the liquid water pressure in the bulks ,$p_{\epsilon,b}^l$, is equal to the gas pressure, p_g, there. The quantity f_{HI} denotes the already defined fraction of hydrophilic pores in the GDLs and catalyst layers and can be interpreted as the residual liquid water saturation according to subsection 2.1.5.

The quantity $j_{\epsilon,m}^l$ in Eqn. 2.43 describes the liquid water flow from the membrane towards the electrodes and is given by $j_{\epsilon,m}^l = -j_\epsilon^l$ and

$$j_\epsilon^l = \left(\begin{matrix} (a) \\ \mp \\ (c) \end{matrix} M_{H_2O}\, \alpha_l\, v_l\, \frac{p_c^l - p_a^l}{\beta_m\, d_m} \begin{matrix} (a) \\ \pm \\ (c) \end{matrix} M_{H_2O}\, \frac{\xi_l}{F} i_{cell} \right) S \,. \tag{2.45}$$

The first term inside the brackets in Eqn. 2.45 describes the hydraulic transport of liquid water through the membrane due to different liquid water pressures at the anode, p_a^l, and cathode side, p_c^l, while the second term models the liquid water transport from the anode to the cathode side due to the electro-osmotic drag of protons. In the first term, α_l denotes the transport coefficient for a liquid-equilibrated membrane and is calculated like in the detailed model by:

$$\alpha_l = \frac{K_m}{\mu_l v_l^2} \left(\frac{f(\lambda)}{f_l} \right)^2 \,, \tag{2.46}$$

where α_l depends on the membrane humidity λ via the quantity f, the volume fraction of water inside the membrane. The maximal value of f is denoted by f_l. They are both given by:

$$f(\lambda) = \frac{\lambda\, v_l}{v_m + \lambda\, v_l} \quad \text{and} \quad f_l = \frac{\lambda_l^{max}\, v_l}{v_m + \lambda_l^{max}\, v_l}\,, \tag{2.47}$$

and are in accordance with Eqn. 2.6 from the detailed model. The calculation of the membrane humidity λ is done with Eqn. 2.56 and is shown later on. If we consider the second term inside the brackets in Eqn. 2.45, we find ξ_l that models the electro-osmotic drag coefficient in a liquid-equilibrated membrane and is calculated according to the detailed model from Eqn. 2.23. Finally, the quantity S in Eqn. 2.45 describes the fraction of expanded channels in the membrane and reads:

$$S = \frac{\lambda - \lambda_\nu^{max}}{\lambda_l^{max} - \lambda_\nu^{max}}\,. \tag{2.48}$$

The above equation is only a part of Eqn. 2.18 given in the detailed model, because the reduced model focuses on the two-phase behavior of the PEMFC. The other quantities in Eqn. 2.45 were already introduced in the last chapter with one exception for β_m, which is used as a fitting parameter for approximating the pressure gradient across the membrane. Please visit Appendix A.2 for its determination.

2.2.2 Balance of gas components

The mass balances are derived for both electrodes. At first, the model equations at the anode side are shown. Due to the negligence of transport resistances for hydrogen, the hydrogen content is constant there and equal to the bulk content: $c_a^{H_2} = c_{a,b}^{H_2}$. Therefore, only water vapor is transported in the gas phase. The averaged mass balance reads:

$$\frac{d\hat{\rho}_a^{H_2O}}{dt} = \frac{1}{d_{gdl} + d_{catl}}\, j_{a,b}^{H_2O} - Q_a^l \tag{2.49}$$

$$\text{with} \quad \hat{\rho}_a^{H_2O} := \pi \rho_a^g (1 - s_a^l) c_a^{H_2O}\,,$$

where $c_a^{H_2O}$ stands for the mass fraction of water vapor at the anode side. The density of the gas mixture, ρ_a^g, is determined from the ideal gas law in Eqn. 2.11 analog to the detailed model, while the variable s_l^a models the liquid water saturation at the anode side and is calculated from Eqn. 2.43. The mass flow $j_{a,b}^{H_2O}$ models the transport of water vapor from the bulk to the anode. This mass flow is determined by:

$$j_{a,b}^{H_2O} = \hat{D}_a^{H_2O}\, \frac{c_{a,b}^{H_2O} - c_a^{H_2O}}{\beta_{H_2O}(d_{gdl} + d_{catl})} \tag{2.50}$$

$$\text{with} \quad \hat{D}_a^{H_2O} := D_{H_2O}\, \rho_a^g\, (1 - s_a^l)^2\, \pi \left(\frac{\pi - 0.11}{1 - 0.11}\right)^{0.785}\,,$$

where $c_{a,b}^{H_2O}$ is the mass fraction of water vapor in the anode bulk and β_{H_2O} is used as a fitting parameter for the approximation of the gradient.

At the cathode side both water vapor and oxygen are transported in the gas phase. This transport is described by the following equations, where $\iota \in \{\mathrm{O}_2, \mathrm{H}_2\mathrm{O}\}$ is used to specify the different species:

$$\frac{d\hat{\rho}_c^\iota}{dt} = \frac{1}{d_{gdl} + d_{catl}}\, j_{c,b}^\iota + Q_c^g \tag{2.51}$$

$$\text{with} \quad \hat{\rho}_c^\iota := \pi \rho_c^g (1 - s_c^l) c_c^\iota$$

$$\text{and} \quad Q_c^g := \begin{cases} -Q_c^l + \frac{M_{H_2O}}{2F} \frac{i_{cell}}{d_{gdl}+d_{catl}} & \text{for} \quad \iota = \mathrm{H}_2\mathrm{O} \\ -\frac{M_{O_2}}{4F} \frac{i_{cell}}{d_{gdl}+d_{catl}} & \text{for} \quad \iota = \mathrm{O}_2 \end{cases} .$$

In the above equation, the mass fractions of species ι at the cathode side are given by c_c^ι, whereas ρ_c^g stands for the density of the gas mixture and is calculated with the ideal gas law as at the anode side. The quantity s_c^l is already introduced in Eqn. 2.43 and models the liquid water saturation at the cathode side. The mass flows $j_{c,b}^\iota$ in Eqn. 2.51 in Eqn. 2.51 are determined from:

$$j_{c,b}^\iota = \hat{D}_c^\iota \frac{c_{c,b}^\iota - c_c^\iota}{\beta_\iota (d_{gdl} + d_{catl})} \tag{2.52}$$

$$\text{with} \quad \hat{D}_c^\iota := D_\iota\, \rho_c^g\, (1 - s_c^l)^2\, \pi \left(\frac{\pi - 0.11}{1 - 0.11} \right)^{0.785} ,$$

where $c_{c,b}^\iota$ denotes the mass fraction of species ι in the cathode bulk. Finally, the quantities β_i, i.e. β_{H_2O} and β_{O_2} are fitting parameters that are used to adapt the behavior of the reduced model to the detailed one.

2.2.3 Reaction kinetics and cell voltage

As mentioned in the model assumptions, it is assumed that the reaction kinetics at the anode side is in equilibrium and the corresponding overvoltage is equal to zero. At the cathode side, the reaction is described by the Butler-Volmer kinetics:

$$i_{cell} = \gamma\, i_c\, d_{catl}\, (1 - s_c^l) \left(\frac{c_c^{O_2}}{c_{ref}^{O_2}} \right) \left(\exp\left(-\frac{\varphi_c \zeta_c F}{\varrho \vartheta} \eta_c \right) - \exp\left(\frac{(1 - \varphi_c)\zeta_c F}{\varrho \vartheta} \eta_c \right) \right) \tag{2.53}$$

where η_c is the overvoltage, $c_c^{O_2}$ is the mass fraction of oxygen and s_l^c is the liquid water saturation at the cathode side. The above equation can be obtained by integrating the cathodic Butler-Volmer kinetics in Eqn. 2.42 from $d\Omega_4$ to $d\Omega_5$ and assuming a constant charge generation rate $\tilde{Q}_c^{ch}$.

The cell voltage is calculated from the well-known equation:

$$U_{cell} = \Delta\phi_{eq} + \eta_c - \frac{d_m}{\sigma_p} i_{cell} \tag{2.54}$$

that follows from the charge balances in subsection 2.1.1 and the Butler-Volmer kinetics at the cathode side by dropping the distributed approach for the membrane. In the above equation, $\Delta\phi_{eq}$ stands for the already introduced equilibrium potential of the cathodic reaction and σ_p denotes the proton conductivity of the membrane. It is calculated in an analog manner to Eqn. 2.5 of the detailed model with

$$\sigma_p = \begin{cases} 50\,(f-0.06)^{1.5}\,\exp\left(\frac{15000}{\varrho}\left(\frac{1}{\vartheta_{ref}}-\frac{1}{\vartheta}\right)\right) & \text{for} \quad f \leq 0.45 \\ 50\,(0.39)^{1.5}\,\exp\left(\frac{15000}{\varrho}\left(\frac{1}{\vartheta_{ref}}-\frac{1}{\vartheta}\right)\right) & \text{for} \quad f > 0.45 \end{cases}, \tag{2.55}$$

where f is determined from Eqn. 2.47.

2.2.4 Membrane humidity

The humidity in the membrane is determined from states calculated in the electrodes. Two candidates for the membrane humidity are calculated, one at the anode and one at the cathode side of the cell. We assume that the resulting humidity is the maximum value of both due to the thin membrane used in the model[1]:

$$\lambda = \max_{\epsilon \in \{a,c\}} \lambda_\epsilon \,. \tag{2.56}$$

Usually, the membrane humidity calculated at the cathode side will be larger than at the anode side. This is due to the produced water of the chemical reaction and the case for higher cell currents. However, at low cell currents the membrane humidity can be determined by the activity of water vapor in the cathode bulk as well as in the anode bulk. Therefore, the calculation at both sides is done. The membrane humidity λ_ϵ at both sides is made up of two parts:

$$\lambda_\epsilon = \lambda_\epsilon^g + \lambda_\epsilon^l \,, \tag{2.57}$$

where λ_ϵ^g considers the dependency of the membrane humidity from the activity of the gas phase and λ_ϵ^l includes the dependency from possible liquid water in the cell. We distinguish between two cases:

1. $s_\epsilon^l = f_{HI}$: The liquid water saturation is equal to its residual saturation (see subsection 2.1.5). The only liquid water present is trapped in hydrophilic pores. We assume that it does not take part in a humidification of the membrane. This means $\lambda_\epsilon^l = 0$. Due to the absence of liquid water in hydrophobic pores there is only a gas phase with an activity in the range $0 \leq a_\epsilon^{H_2O} \leq 1$. The membrane humidity is then given by $\lambda_\epsilon = \lambda_\epsilon^g$ and is in the range $0 \leq \lambda_\epsilon \leq \lambda_g^{max}$.

2. $s_\epsilon^l > f_{HI}$: Liquid water is built and the liquid water saturation is larger than the residual saturation. The gas phase is saturated and therefore the activity

[1]This assumption is taken, because simulations of the membrane humidity in the detailed two-phase model always showed, at high as well as low cell currents, only small spatial gradients across the membrane.

is one: $a_\epsilon^{H_2O} = 1$. This means $\lambda_\epsilon^g = \lambda_g^{max}$. There is liquid water present in hydrophobic pores which we assume takes part in the humidification of the membrane. This means $\lambda_\epsilon^l > 0$ and therefore the membrane humidity for this case is $\lambda_\epsilon = \lambda_g^{max} + \lambda_\epsilon^l$ and is in the range $\lambda_g^{max} < \lambda_\epsilon \leq \lambda_l^{max}$.

As mentioned above, λ_ϵ^g depends on the relative humidity $a_\epsilon^{H_2O}$ in the GDLs and CATLs, and the same approach as in the detailed model is used to express this dependency:

$$\lambda_\epsilon^g = 0.043 + 17.81 a_\epsilon^{H_2O} - 39.85 \left(a_\epsilon^{H_2O}\right)^2 + 36 \left(a_\epsilon^{H_2O}\right)^3 , \tag{2.58}$$

where the activity is defined by

$$a_\epsilon^{H_2O} := \frac{p_\epsilon^{H_2O}}{p_{sat}} , \tag{2.59}$$

in the range $0 \leq a_\epsilon^{H_2O} \leq 1$, with the pressure of the vapor phase, $p_\epsilon^{H_2O}$, and its saturation pressure, p_{sat}, that can be calculated in an analogous manner like in Eqn. 2.39 and Eqn. 2.40 of the detailed model. The dependency of the membrane humidity from the liquid water content in Eqn. 2.57 is modeled with the quantity λ_ϵ^l, where we propose the following calculation:

$$\lambda_\epsilon^l = \frac{\lambda_l^{max} - \lambda_g^{max}}{2} \left(1 - \operatorname{erf}\left(\frac{\ln\left(\frac{2 \cdot 10^9 \, \Sigma_{H_2O} \cos\theta_3}{p_\epsilon^{cp}}\right) - \ln(1.25)}{0.3\sqrt{2}}\right)\right) . \tag{2.60}$$

This equation can be easily derived from the membrane model in subsection 2.1.4, where p_ϵ^{cp} stands for the capillary pressure and is determined according to the next section.

2.2.5 Additional equations

The liquid water pressure and the condensation and vaporization in the reduced model are calculated in an analog manner as in the original model in order to maintain their impact upon the two-phase water household. Therefore, the model equations presented in subsection 2.1.5 and subsection 2.1.6 also apply to the reduced model if the distributed variables, marked by a tilde, are replaced by the corresponding ones of the reduced model.

2.2.6 Operating conditions and numerical solution

In summary, the reduced PEMFC model forms a DAE system that consists of 5 dynamic and 11 algebraic states. The operating conditions of the reduced model are the same as for the detailed model and determined by the parameters in Table 2.1 and Table 2.2. The implementation of the reduced model is also done in ProMoT [73], and the simulations are performed with DIVA [52] too.

Table 2.2: Additionally used parameter values and constants.

Quantity	Value
fitting parameter, β_l	0.08
fitting parameter, β_m	0.7
fitting parameter, β_{H_2O}	0.2
fitting parameter, β_{O_2}	2.385

2.3 Concentrated one-phase PEMFC model

The coupling analysis in chapter 5 is performed with a relative simple, dynamic and lumped one-phase fuel cell model in order to outline the essential qualitative effects due to the coupling between one-phase or two-phase PEMFCs and DC-DC converters. For this purpose, the fast dynamics of the electrochemical reactions have to be taken into account and the slow dynamics, e.g. of the liquid water transport can be neglected. Therefore, the main model characteristics read:

- It is assumed that there is no liquid water in the gas bulks and the gas diffusion layers.
- Only the cathode of the fuel cell is considered. The anodic reaction is assumed to be in equilibrium and the anodic overpotential is equal to zero.
- The cathodic gas bulk, the gas diffusion layer and the catalyst layer are modeled as one perfectly mixed phase (Fig. 2.5).
- The electrochemical reactions in the cathodic catalyst layer and the membrane are modeled by the equivalent electrical circuit in Fig. 2.5, as suggested in [19].
- The dynamic behavior of the membrane's water household is neglected.
- The model is isothermal and the gas phases are isobaric and behave like ideal gases.
- The Tafel approach is used for the cathode kinetics.

In the following the model equations are presented. For a derivation of the model equations please see Appendix A.3. The appearing quantities are also given in the list of symbols. First of all, the dynamic equations of the model are specified. The transport equations for the gas transport read

$$\dot{x}_c^{O_2} = -\frac{A}{2\chi_c^{tot}\zeta_c V_c F}\left(1 + x_c^{O_2}\right) i_T + \left(x_{c,b}^{O_2} - x_c^{O_2}\right)\frac{\dot{V}_{c,b}}{V_c}\,, \tag{2.61}$$

$$\dot{x}_c^{H_2O} = \frac{A}{2\chi_c^{tot}\zeta_c V_c F}\left(2 - x_c^{H_2O}\right) i_T + \left(x_{c,b}^{H_2O} - x_c^{H_2O}\right)\frac{\dot{V}_{c,b}}{V_c}\,, \tag{2.62}$$

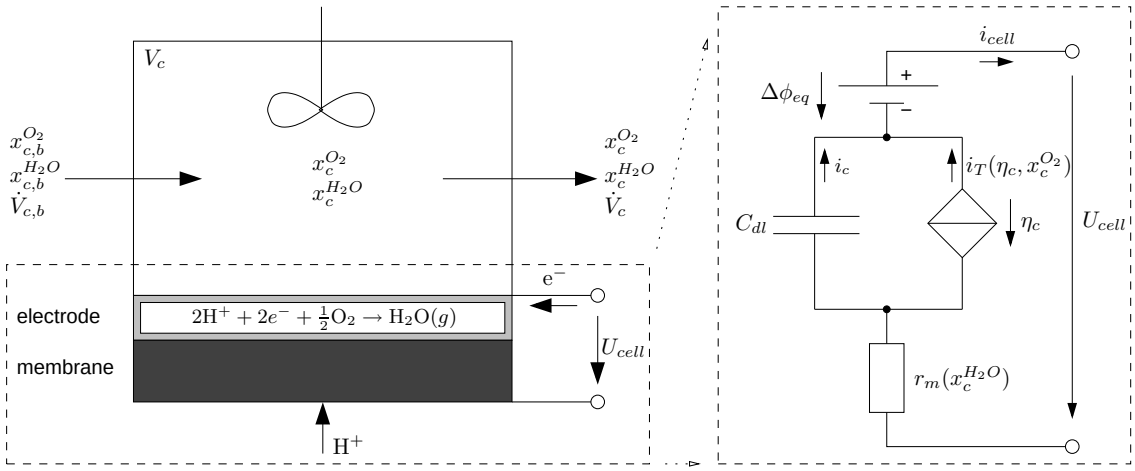

Figure 2.5: Modeling approach of the PEM fuel cell.

where $x_c^{O_2}$ and $x_c^{H_2O}$ denote the content of oxygen and water vapor in the PEMFC. The overvoltage in the catalyst layer is described by η_c and is determined by

$$\dot{\eta}_c = \frac{1}{C_{dl}} (i_T - i_{cell}) \quad \text{with} \quad i_T := i_T^0 \, x_c^{O_2} \, \exp(-b\eta_c) \tag{2.63}$$

$$\text{and} \quad b := (1 - \varphi_c)\zeta_c F / \varrho\vartheta \, . \tag{2.64}$$

The electrical current density in the fuel cell is given by i_{cell} and $\dot{V}_{c,b}$ describes the volume flow rate of humidified air that enters the cell. The other quantities are constant model parameters. An additional algebraic equation is used to calculate the cell voltage U_{cell}:

$$U_{cell} = \Delta\phi_{eq} + \eta_c - r_m(x_c^{H_2O}) \, i_{cell} \, . \tag{2.65}$$

Equation 2.65 includes activation losses of the catalyst via the overvoltage η_c and ohmic losses due to the transport of protons, modeled by the membrane resistance r_m. The membrane's resistance is calculated from its proton conductivity σ_p: $r_m(x_c^{H_2O}) := d_m/\sigma_p(x_c^{H_2O})$, where for brevity the following dependency from [84] is used to model the dependency from the cathodic water content:

$$\sigma_p(x_c^{H_2O}) = \sigma_{p_0} \, exp(14 \, (x_c^{H_2O} \, p_g/p_{sat})^{0.2}) \, .$$

In summary, the fuel cell model is made up by a system of 3 nonlinear ordinary differential equations and an additional algebraic equation. The PEMFC model is operated at one-phase conditions with respect to the water household. It is fed with air and will be operated in rheostatic mode due to the coupling with the DC-DC converters. The parameters for the fuel cell model are mainly taken from the first chapter and [90], while the parameters for the DC-DC converters are chosen according to guidelines in [20, 65]. Both are described and given in the following Table 2.3.

It should be noted, that the precise parameter values are not that important for the subsequent analysis. Instead, the qualitative relationship due to coupling between the fuel cell and the converter parameters is of deciding importance as will be shown in chapter 5.

Table 2.3: Used parameter values.

Quantity	**Value**
total concentration in cathode, χ_c^{tot}	$p_g/\varrho\vartheta$
equilibrium potential cathode, $\Delta\phi_{eq}$	$1.17\ V$
charge transfer coefficient cathode, φ_c	0.5
min. proton conductivity of membrane, σ_{p_0}	$1.3 \cdot 10^{-5}\ S/m$
cell temperature, ϑ	$353\ K$
cross-sectional area of fuel cell, A	$1.0 \cdot 10^{-4}\ m^2$
capacitance of DC-DC converters, C	$300 \cdot 10^{-6}\ F$
double layer capacitance, C_{dl}	$0.01\ F/m^2$
exchange current density (Tafel eq.), i_T^0	$0.01\ A/m^2$
inductivity of DC-DC converters, L	$82 \cdot 10^{-5}\ H$
gas pressure, p_g	$1.013 \cdot 10^5\ Pa$
saturation pressure of water vapor (at ϑ), p_{sat}	$4.7373 \cdot 10^4\ Pa$
duty period of DC-DC converters, T	$1 \cdot 10^{-4}\ s$
volume of gas cathode, V_c	$0.5 \cdot 10^{-6}\ m^{-3}$
volume flow rate of air, $\dot{V}_{c,b}$	$1.7873 \cdot 10^{-7}\ m^3/s$
molar fraction of water vapor at inlet, $x_{c,b}^{H_2O}$	0.14
molar fraction of oxygen at inlet, $x_{c,b}^{O_2}$	0.21

2.4 Distributed one-phase PEMFC model

Finally, the last considered model, used for the development and test of the passivity-based control approach, is presented in this section. It is a dynamic, distributed and one-phase model that consists of the detailed and distributed membrane model from chapter 3, where only the vapor phase is considered, and lumped electrode models for the anode and the cathode, similar to the electrode model in chapter 5. Therefore, the model assumptions are made up from the ones in section 2.1 and section 2.3 and read in summary:

- The model is isothermal.
- The gas phases are isobaric and behave like ideal gases.
- The anodic gas bulk is closed at the end, whereas the cathodic gas bulk is open there.

- The anodic and cathodic gas bulks, gas diffusion layers and catalyst layers are modeled as one perfectly mixed phase.
- The transport resistances for electrons in the GDLs and CATLs are neglected.
- The anodic reaction is in equilibrium and the anodic overpotential is zero.
- The electrochemical reaction in the cathodic catalyst layer is modeled by the equivalent electrical circuit proposed in [19].
- The transport of water vapor as well as the corresponding electro-osmotic drag of water through the membrane are considered using the membrane model from chapter 3.

In the following, the model equations are presented. For a description of the appearing quantities, please see also the list of symbols.

2.4.1 Cathode

For the modeling of the cathode, a lumped model approach considering the GDL, the CATL and the gas bulk is used. This is done in the same way as in section 2.3 with the only exception that the mass flow of water vapor to the membrane ($N_c^{H_2O}$) is additionally considered here. Because the fuel cell is fed with air again at the cathode side, oxygen, water vapor and nitrogen are present there. The balance equation for oxygen reads:

$$\frac{dx_c^{O_2}}{dt} = \frac{A}{\chi_c^{tot} V_c} \left(x_c^{O_2} N_c^{H_2O} - \left(1 + x_c^{O_2}\right) \frac{i_T}{2\zeta_c F} \right) + \left(x_{c,b}^{O_2} - x_c^{O_2}\right) \frac{\dot{V}_{c,b}}{V_c} , \tag{2.66}$$

where $x_c^{O_2}$ denotes the oxygen content inside the cathode and $N_c^{H_2O}$ denotes the flux of water vapor from the cathode to the membrane. The current produced by the electrochemical reaction is described with the Tafel kinetics i_T given in Eqn. 2.63, and $\dot{V}_{c,b}$ models the volume flow rate of air that enters the electrode. The other appearing quantities are constant model parameters.

In contrast to the molar description of the water content in Eqn. 2.62, the activity of water is used here instead. It is defined in the same manner as in Eqn. 2.59 and is calculated from the following equation:

$$\begin{aligned} \frac{da_c^{H_2O}}{dt} =& \frac{A}{\chi_c^{tot} V_c} \left(\left(2\frac{p_c^g}{p_{sat}} - a_c^{H_2O} \right) \frac{i_T}{2\zeta_c F} - \left(\frac{p_c^g}{p_{sat}} - a_c^{H_2O} \right) N_c^{H_2O} \right) \\ &+ \left(a_{c,b}^{H_2O} - a_c^{H_2O}\right) \frac{\dot{V}_{c,b}}{V_c} . \end{aligned} \tag{2.67}$$

The activity of water vapor is related to its molar fraction by the following equation: $a_c^{H_2O} := x_c^{H_2O} p_c^g / p_{sat}$ where p_c^g and p_{sat} denote the total gas pressure in the cathode and the saturation pressure of water vapor there. The activity at the cathodic inlet, $a_{c,b}^{H_2O}$, is defined in the same way. Finally, the electrochemical reaction in the catalyst layer is also considered in the above equation and modeled with the Tafel kinetics i_T.

2.4.2 Anode

The modeling of the anode is also done with a lumped approach for the gas diffusion layer, the catalyst layer and the gas bulk. In contrast to the cathode side, the anodic gas bulk is closed at the end. This represents a common approach in fuel cell design, if one neither want to recycle nor waste the unreacted hydrogen fed at the anode side. At the anode, hydrogen and water vapor are present. The activity of water in the anode is modeled with the following differential equation:

$$\frac{da_a^{H_2O}}{dt} = -\frac{A}{\chi_a^{tot} V_a} \frac{p_a^g}{p_{sat}} N_a^{H_2O} + \frac{A}{\chi_a^{tot} V_a} \left(\frac{i_{cell}}{\zeta_c F} + N_a^{H_2O} \right) a_{a,b}^{H_2O} \,, \tag{2.68}$$

where $a_a^{H_2O}$ and $a_{a,b}^{H_2O}$ describe the activity of water vapor inside the anode and the anodic bulk respectively. Further important quantities above are the delivered current of the PEMFC, i_{cell}, and the flux of vapor from the anode towards the membrane: $N_a^{H_2O}$.

2.4.3 Membrane

In the membrane the transport of protons and water vapor is modeled. The membrane model described in chapter 3 can be used for this purpose. Therefore, the balance equation for the transport of protons is given by Eqn. 2.3, for $\kappa = 3$, where in the following the subscript 3 of the quantities is replaced by m in order to improve the readability of the equations. The boundary conditions for Eqn. 2.3 read

$$\tilde{j}_m^p|_{d\Omega_3} = \tilde{j}_m^p|_{d\Omega_4} \triangleq i_{cell} \,, \tag{2.69}$$

$$\tilde{\phi}_m^p|_{d\Omega_3} \triangleq 0 \,, \tag{2.70}$$

$$\tilde{\phi}_m^p|_{d\Omega_4} \triangleq U_{cell} - \Delta\phi_{eq} - \eta_c \,, \tag{2.71}$$

and can be obtained with the given model assumptions from the corresponding boundary conditions in chapter 3. In the above equation the quantities i_{cell}, U_{cell} and η_c denote the cell current, the cell voltage and the overvoltage of the cell again.

The content of water vapor in the membrane is described by the model from Weber given in chapter 3, if only the transport of water vapor is considered. Therefore, the water balance in Eqn. 2.16 is also used in this chapter, with the exception that the flux of water vapor through the membrane is determined only by the vapor part and reads

$$\tilde{N}_{H_2O} = -\left(\tilde{\alpha}_g + \frac{\tilde{\sigma}_m^p \xi_g^2}{F^2} \right) \frac{\varrho \vartheta}{\tilde{a}_m^{H_2O}} \frac{\partial \tilde{a}_m^{H_2O}}{\partial z} - \frac{\tilde{\sigma}_m^p \xi_g}{F} \frac{\partial \tilde{\phi}_m^p}{\partial z} \,, \tag{2.72}$$

where the dependence of the electrochemical potential from the activity of water vapor from Eqn. 2.24 is inserted for simplicity. The above flux of water vapor considers two transport mechanisms: The first term denotes the activity-based transport of water by $\tilde{a}_m^{H_2O}$, whereas the second term describes the electro-osmotic drag of water molecules. The water content $\tilde{\lambda}$ of the membrane and the activity $\tilde{a}_m^{H_2O}$ are coupled

with Eqn. 2.25 again. The other quantities in the above equation are calculated in the same manner as in chapter 3. Finally, the boundary conditions for the balance of water vapor are given by:

$$\tilde{N}_{H_2O}|_{d\Omega_3} \triangleq N_a^{H_2O} \quad \text{and} \quad \tilde{N}_{H_2O}|_{d\Omega_4} \triangleq -N_c^{H_2O} \,, \tag{2.73}$$

$$\tilde{a}_m^{H_2O}|_{d\Omega_3} \triangleq a_a^{H_2O} \quad \text{and} \quad \tilde{a}_m^{H_2O}|_{d\Omega_4} \triangleq a_c^{H_2O} \,, \tag{2.74}$$

where the variables $N_a^{H_2O}$ and $N_c^{H_2O}$ denote the flux of water vapor from the anode and the cathode, and $a_a^{H_2O}$ and $a_c^{H_2O}$ stand for the activities of water vapor there.

2.4.4 Operating conditions

In the previous chapter we outlined that PEM fuel cells are in generally coupled with power conditioning units and are operated in rheostatic mode. This mode of operation is also considered in this chapter and therefore the above model equations are extended by

$$0 = r_{cell}\, i_{cell} - U_{cell} \,, \tag{2.75}$$

where r_{cell} denotes the ohmic load resistance of the PEMFC and can be interpreted as the input resistance of the succeeding power conditioning unit. Besides the rheostatic operation, the same parameter values as in chapter 3 and chapter 5 are used for the following control design. They are summarized for clarity in Table 2.4.

Table 2.4: Used parameter values and constants.

Quantity	**Value**
total concentration in anode, χ_a^{tot}	$p_a^g/\varrho\vartheta$
total concentration in cathode, χ_c^{tot}	$p_c^g/\varrho\vartheta$
equilibrium potential of the cathodic reaction, $\Delta\phi_{eq}$	$1.17\ V$
charge transfer coefficient at anode, φ_a	0.5
charge transfer coefficient at cathode, φ_c	0.5
density of the dry membrane, ρ_m	$1980\ kg/m^3$
cell temperature, ϑ	$353\ K$
reference temperature, ϑ_{ref}	$298\ K$
no. of exchanged electrons at cathodic reaction, ζ_c	2
cross-sectional area of fuel cell, A	$1.0 \cdot 10^{-4}\ m^2$
thickness of the membrane, d_m	$25 \cdot 10^{-6}\ m$
equivalent weight of the dry membrane, EW	$0.909\ kg/mol$
exchange current density (Tafel Eqn.), i_T^0	$0.01\ A/m^2$
overall gas pressure in anode, p_a^g	$1.013 \cdot 10^5\ Pa$
overall gas pressure in cathode, p_c^g	$1.013 \cdot 10^5\ Pa$
saturation pressure of water vapor (at ϑ), p_{sat}	$4.7373 \cdot 10^4\ Pa$

continued ...

Quantity	Value
volume of gas in anode, V_a	$0.5 \cdot 10^{-6}\ m^{-3}$
volume of gas in cathode, V_c	$0.5 \cdot 10^{-6}\ m^{-3}$
molar fraction of oxygen at inlet, $x_{c,b}^{O_2}$	0.21

2.4.5 Numerical treatment

In summary, the model consists of one partial differential equation, one ODE in space, four ODEs in time and an additional algebraic equation. The model is discretized using the method of finite volume elements with an equidistant grid. This results in a differential algebraic system of equations:

$$\dot{\mathbf{z}}_D = \mathbf{f_D}\left(\mathbf{z}_D, \mathbf{z}_A, \mathbf{u}\right) , \tag{2.76}$$

$$\mathbf{0} = \mathbf{f_A}\left(\mathbf{z}_D, \mathbf{z}_A, v\right) , \tag{2.77}$$

$$\mathbf{y} = \mathbf{h}\left(\mathbf{z}_D, \mathbf{z}_A\right) . \tag{2.78}$$

The dynamic and algebraic states are denoted with $\mathbf{z}_D\ (\in \mathbb{R}^{N+5})$ and $\mathbf{z}_A\ (\in \mathbb{R}^{2N+1})$ respectively. They are given by

$$\mathbf{z}_D := \left(a_a^{H_2O}\ a_c^{H_2O}\ x_c^{O_2}\ \eta_c\ \tilde{\lambda}[1]\ \ldots\ \tilde{\lambda}[N]\right)^T , \tag{2.79}$$

$$\mathbf{z}_A := \left(i_{cell}\ \tilde{a}_m^{H_2O}[1]\ \ldots\ \tilde{a}_m^{H_2O}[N]\ \tilde{\phi}_m^{p}[1]\ \ldots\ \tilde{\phi}_m^{p}[N]\right)^T , \tag{2.80}$$

where the quantities $\tilde{\lambda}[k]$, $\tilde{a}_m^{H_2O}[k]$ and $\tilde{\phi}_m^{p}[k]$ from $k \in \{1 \ldots N\}$ denote the discretized local variables of the membrane humidity, the activity of water vapor and the potential of the proton conducting phase in the membrane. The input variables of the system in Eqn. 2.76 are denoted with $\mathbf{u}\ (\in \mathbb{R}^3)$ and are defined by

$$\mathbf{u} := \left(a_{a,b}^{H_2O}\ \dot{V}_{c,b}\ a_{c,b}^{H_2O}\right)^T . \tag{2.81}$$

They include the activity of water vapor at the inlet of the anodic gas bulk, the volume flow rate of air that enters the cathode and the activity of vapor at the inlet of the cathodic gas bulk. The state equations in Eqn. 2.76 and Eqn. 2.77 are completed by an output equation (2.78), where the important state variables for the operation of the PEMFC are gathered in the following manner:

$$\mathbf{y} := \left(a_a^{H_2O}\ \overline{a}_m^{H_2O}\ x_c^{O_2}\ a_c^{H_2O}\ i_{cell}\ U_{cell}\ p_{cell}\right)^T . \tag{2.82}$$

The output vector $\mathbf{y}(\in \mathbb{R}^7)$ is made up from seven variables, where $\overline{a} := \frac{1}{N}\sum_{k=1}^{N} \tilde{a}_m^{H_2O}[k]$ denotes the average activity of water vapor in the membrane and $p_{cell} := U_{cell}\, i_{cell}$ the electrical power that the fuel cell can deliver. Finally, the last undeclared variable in state Eqn. 2.76 and Eqn. 2.77 is the disturbance $v := r_{cell}$ that is equal to the ohmic load resistance connected to the PEMFC. In summary, the DAE system from Eqn. 2.76 to Eqn. 2.78 consists of $N + 5$ dynamic and $2N + 1$ algebraic states. This system is used as basis for the control approach in chapter 6.

CHAPTER 3

Nonlinear analysis of two-phase PEM fuel cells

Polymer electrolyte membrane fuel cells (PEMFCs) are a promising technology for the electrical power generation. However, as was pointed out in chapter 1, there are still some problems that have to be solved before PEMFCs can realize their full potential. One major problem is the water management, i.e. the flooding and the drying out of the cell. In both cases the performance of the fuel cell decreases [18, 39]. Therefore it is of major interest to hold the balance between flooding and drying out in fuel cell operation. In order to do so, a detailed knowledge about the water household of PEMFCs is necessary. One suitable way to obtain further information is via a thorough analysis based upon a detailed model of the cell. With this approach possible multiplicities and instabilities in the water household can be detected, explained and their impact can be investigated. In the last few years different mechanisms leading to instabilities and multiplicities in PEM fuel cells have been identified by various authors. Benziger et al. [8] investigated the effect of varying membrane conductivity of auto-humidified PEMFCs in experimental and theoretical studies. The transport of protons through the polymer membrane and its effect on steady state stability was investigated by Katsaounis et al. [37]. Kulikovsky [41] showed that bistabilities may occur due to a varying oxygen content on the cathode side. Zhang et al. [88] studied instabilities due to CO poisoning on the anode side and most recently Hanke-Rauschenbach et al. [28] discovered bistable current-voltage characteristics in PEMFCs when operated with a reduced feed stream humidification. This chapter tries to extend the results in literature by performing a bifurcation analysis of the detailed two-phase PEMFC model introduced in section 2.1. The analysis of two-phase models has not been addressed before in detail and allows us to gain further information about the effect of flooding and drying out in PEMFCs.

This chapter is divided in three parts. Due to the earlier introduction of the used two-phase PEMFC model in section 2.1, the following section directly turns its focus towards the bifurcation analysis and its results, while the subsequent section 3.2 presents dynamic simulation results of the two-phase model. Finally, the content of this chapter is summarized in section 3.3.

3.1 Bifurcation analysis

In this section the results of the bifurcation analysis are presented. In a first step, the concept of a bifurcation analysis is shortly summarized in subsection 3.1.1. In a second step, the appearance of multiple steady states under galvanostatic operation is discussed in subsection 3.1.2. The galvanostatic operation is chosen, because it permits a simple physical interpretation of the observed multiplicity. However, in real life applications a fuel cell is rarely operated under a constant current. Therefore, the case of a rheostatic operation, i.e. the operation with a constant external ohmic resistance is studied in detail in the further analysis in subsection 3.1.3.

Throughout this analysis only the model parameters $c_{a,b}^{H_2O}$, $c_{c,b}^{H_2O}$, f_{HI}, π and K are modified, while the other parameters are hold at their values given in Table 2.1. The water contents in the gas bulks denoted by the mass fractions $c_{a,b}^{H_2O}$ and $c_{c,b}^{H_2O}$ and the fraction of hydrophilic pores f_{HI} are chosen due to their strong influence on the water management of the fuel cell, i.e. the water vapor and liquid water flow out of the PEMFC. The porosity π and the permeability K are chosen, because little is known about the porosity and permeability of a compressed fuel cell and their influence upon the water household in a PEM fuel cell.

3.1.1 Introduction to bifurcation analysis

Bifurcation theory [44, 66] is a mathematical concept for the analysis of nonlinear dynamical systems. The basic term in this is bifurcation. A bifurcation happens in a nonlinear dynamical system if the system behavior changes qualitatively upon parameter changes, i.e. the stability of the solutions and/or its number alters. A bifurcation analysis is carried out to find and classify bifurcations in a nonlinear dynamical system. Such an analysis can be performed analytically or numerically. In this contribution it is performed numerically with parameter continuation methods in DIVA [52]. The class of systems treated in DIVA are differential algebraic equations (DAE) of differential index one[1] in semi-explicit form:

$$\mathbf{B}\left(\mathbf{x},\mathbf{p}\right)\dot{\mathbf{x}} = \mathbf{f}\left(\mathbf{x},\mathbf{p}\right) \quad \text{with} \quad \mathbf{x} \in \mathbb{D}_x \subseteq \mathbb{R}^n \text{ and } \mathbf{p} \in \mathbb{D}_p \subseteq \mathbb{R}^p\,, \tag{3.1}$$

where $\mathbf{x}$ and $\mathbf{p}$ represent the state and parameter vector of the system respectively. The simplest continuation that can be performed is a continuation of steady state

[1] The differential index is defined as the minimum number of times that the algebraic equations of a DAE system have to be differentiated with respect to time in order to transform the DAE into an ODE system [10].

solutions of Eqn. 3.1 in one parameter $\lambda \in \mathbf{p}$. For this, the solutions of the nonlinear algebraic problem $0 = \mathbf{f}(\mathbf{x}, \lambda)$ have to be determined by the continuation algorithm. The stability of the steady-state solutions is analyzed by computing the eigenvalues of the linearized system of equations at the steady states. If during the one parameter continuation the real part of at least one eigenvalue vanishes then a local bifurcation occurs. The system behavior can then be further examined with a two-parameter continuation starting at the found bifurcation. In summary, a bifurcation analysis is a powerful tool to predict and distinguish between different model behaviors and can be used to improve both process design and operation.

3.1.2 Galvanostatic operation

First of all, it is assumed that the fuel cell is operated in galvanostatic mode. This means that the cell current i_{cell} is used as continuation parameter. Figure 3.1 shows the steady-state results of the fuel cell model for nominal parameter values. For small to medium cell currents the current-voltage plot in Fig. 3.1 has the shape that is typical for most fuel cells. But at very high cell currents, e.g. around $5000\,A/m^2$, two steady state solutions are found to coexist. A stability analysis reveals that steady state solutions on the upper solution branch (solid line in Fig. 3.1a) are stable whereas solutions on the lower branch (dashed line) are unstable. This result can be understood by comparing the state of the fuel cell at two coexisting steady states, say state 1 and state 2 in Fig. 3.1b,c,d.

At equilibrium 1 there is a low liquid water saturation (Fig. 3.1c) and therefore a small transport resistance for the gas diffusion in the cathodic catalyst layer (see Eqn. 2.13). This results in a high oxygen concentration (Fig. 3.1d) and also leads to a large active catalyst area (see Eqn. 2.42) in the cathodic catalyst. Both effects together combine to give the high cell voltage (Fig. 3.1b) at equilibrium 1.

At equilibrium 2 there is a high liquid water saturation (Fig. 3.1c) and therefore a high transport resistance for the gas diffusion in the cathodic catalyst. Conversely, this leads to a low oxygen content (Fig. 3.1d) and to a small area of the catalyst. Together with the fact that the same cell current is required at steady state 2 and 1 the cell voltage at equilibrium 2 must be smaller than at equilibrium 1.

It should be noted that the stability property of the steady states and the number of coexisting steady states depends on the operation mode of the fuel cell. If potentiostatic operation is considered, i.e. the cell voltage U_{cell} is used as continuation parameter, then the PEMFC has only one steady state that is always stable. If the fuel cell is connected with an ohmic resistance (rheostatic operation), then up to three coexisting steady states may lie on the same line $r_{cell} := U_{cell}/i_{cell} = const.$ The case of rheostatic operation is due to its practical relevance studied in more detail in the next section.

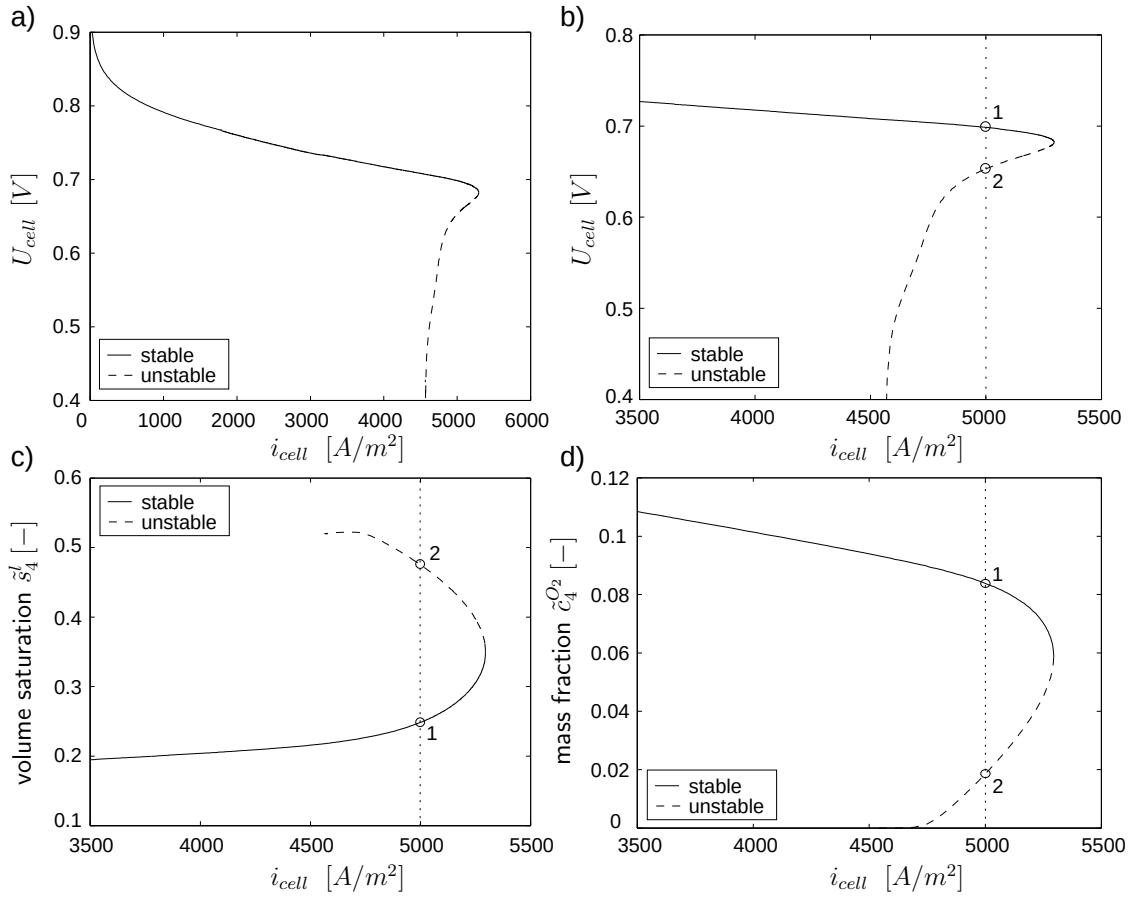

Figure 3.1: 1-parameter continuation of the cell current i_{cell}: a) shows the overall (steady-state) voltage-current profile. In b) a detail of a) is depicted. In c) and d) the liquid water saturation and the mass fraction of oxygen at the left border of the cathodic catalyst are shown respectively.

3.1.3 Rheostatic operation

In this subsection the results of the bifurcation analysis are presented if the fuel cell is operated in rheostatic mode, with the load resistance r_{cell} used as continuation parameter.

Influence of the water content. The influence of the water content in the anodic and cathodic gas bulk is examined at first. This is done by considering the activity of water vapor there. The content of water vapor in the gas phase of catalyst layers and gas diffusion layers can be described by the activity of water vapor. It can be defined as the quotient between the actual partial pressure of water vapor and its saturation pressure:

$$\tilde{a}_{\kappa}^{H_2O} := \frac{\tilde{p}_{\kappa}^{H_2O}}{p_{sat}} , \tag{3.2}$$

where the partial pressure of water vapor is given by Eqn. 2.39 and depends on the gas composition, while the saturation pressure is calculated from Eqn. 2.40 and mainly depends on the cell temperature. The activity in the gas bulks can be defined in the same way: $a_{\kappa,b}^{H_2O} := p_{\kappa,b}^{H_2O}/p_{sat}$ and can be varied by changing the partial pressure of water via the mass fractions of water vapor in the anode and cathode bulk, i.e. $c_{a,b}^{H_2O}$ and $c_{c,b}^{H_2O}$ respectively. This is done in the following analysis, where activities in the anode and cathode bulk of 0.86 and 0.93 are used respectively, while the other parameters in Table 2.1 are at nominal values. Figure 3.2 shows the results of the bifurcation analysis for this study. From Fig. 3.2a we can identify a region of steady state multiplicities between points 1 and 2 that is fairly small. If we look at the corresponding 1-parameter continuation of the load resistance r_{cell} in Fig. 3.2b we can distinguish between three branches of steady states: Two stable branches and one unstable branch. They are also shown as voltage-current profile in Fig. 3.2c. In case II the activity in the cathode bulk is increased to 0.97 whereas the activity in the anode bulk is kept constant at 0.86. In Fig. 3.2a there is a multiplicity region between points 3 and 4 which is clearly larger than the multiplicity region of case I. This is also confirmed if we compare both cases in Fig. 3.2b,c with each other. In case III the activity in the cathode bulk is kept constant at 0.97 and the activity in the anode bulk is decreased to 0.8. It can be seen that the multiplicity region between points 5 and 6 in Fig. 3.2a is much smaller than for case II. The 1-parameter continuation in Fig. 3.2b and the voltage current profile in Fig. 3.2c give the same impression. If the activity in the anode bulk is further decreased then the multiplicity vanishes.

In summary, the found steady state multiplicity appears only at high activities of water vapor. Its magnitude increases with rising relative humidity in the anode and cathode bulk and vice versa. An operation of the fuel cell model at very high activities in the anode bulk leads to steady state multiplicities for smaller activities in the cathode bulk. Parameter changes of the hydrogen content in the anode bulk and the oxygen content in the cathode bulk may also change the activity in the bulks and therefore the region of multiple steady states.

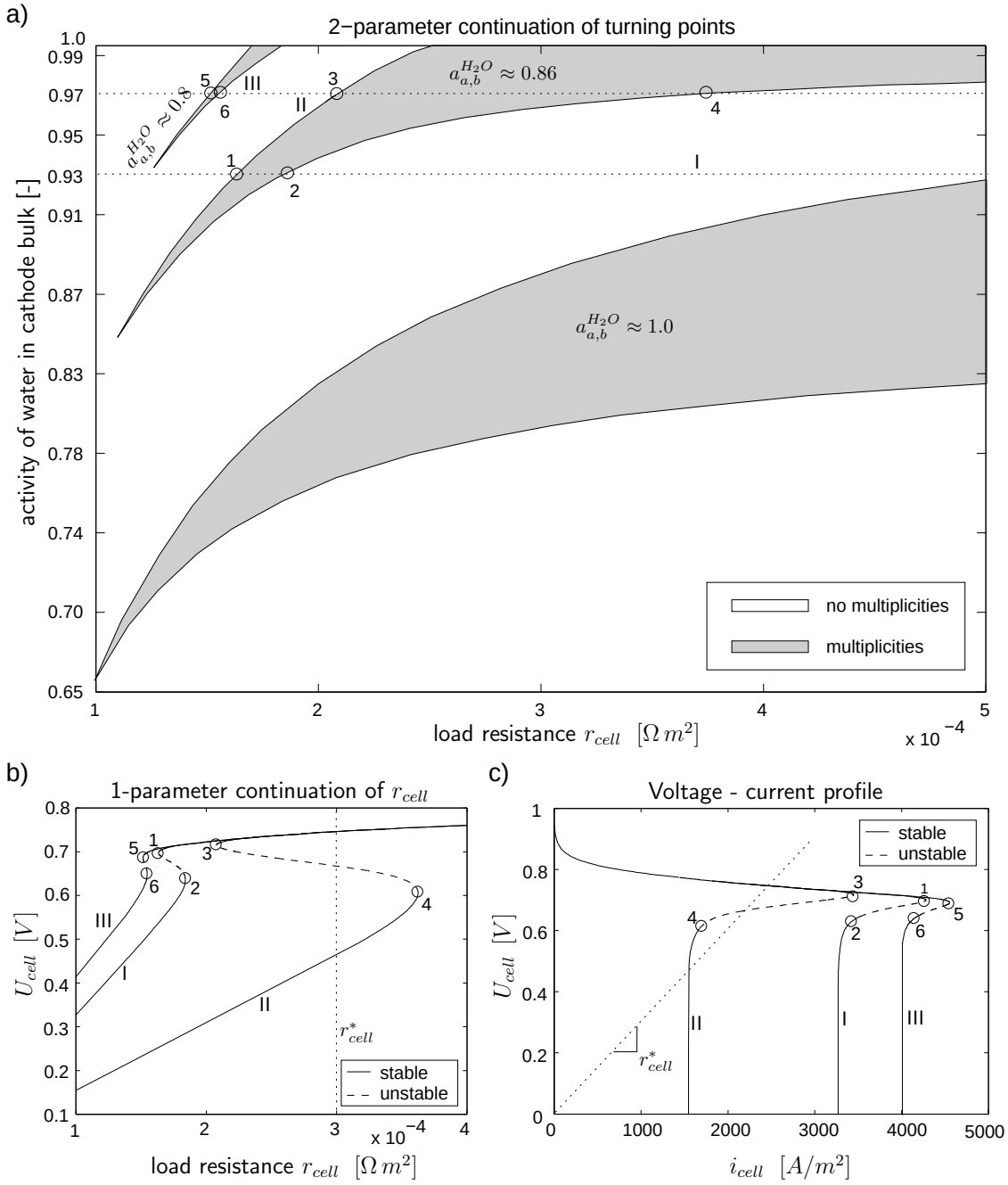

Figure 3.2: Influence of the activity of water vapor in the anode and cathode bulk upon the found steady state multiplicity: a) shows the resulting parameter portrait when the load resistance and the activity in the cathode bulk and anode bulk are changed. In b), three to a) corresponding 1-parameter continuations of the load resistance are depicted, and c) shows the corresponding voltage-current profiles for the three 1-parameter continuations of b).

Influence of the liquid water outflow. In a second study the influence of the liquid water outflow from the fuel cell on the multiplicity is investigated. The liquid water flow is changed by varying the model parameter f_{HI}. For $f_{HI} = 0$ there is no liquid water outflow from the PEMFC, whereas for $f_{HI} > 0$ there is a liquid water flow as described in section 2.1. The other model parameters listed in Table 2.1 are at their nominal values. The results of this study are given in Fig. 3.3.

First of all, case I in Fig. 3.3 is considered: f_{HI} is held at its nominal value, at zero. It can be seen from Fig. 3.3a that there is a multiplicity region between points 1 and 2. Figure 3.3b shows the corresponding 1-parameter continuation with three branches: Two stable branches and one unstable branch of steady states. If case II in Fig. 3.3 is examined, where f_{HI} is set to 4×10^{-3}, there is also a multiplicity region between points 3 and 4, but this one is clearly smaller than that for case I. If f_{HI} is further increased then the multiplicity vanishes. The values for f_{HI} in this study are quite small if they are compared to that of Weber [80]. This may be due to the fact that in this work an other relationship for the capillary pressure is used as in [80]. The determination of capillary pressure correlations in GDLs is still an active area of research. There may exist a dependency of the absolute values of f_{HI} on different capillary pressure approaches but this has still to be analyzed. In summary, the region of stationary multiplicities decreases and vanishes with rising liquid water outflow from the cell and vice versa.

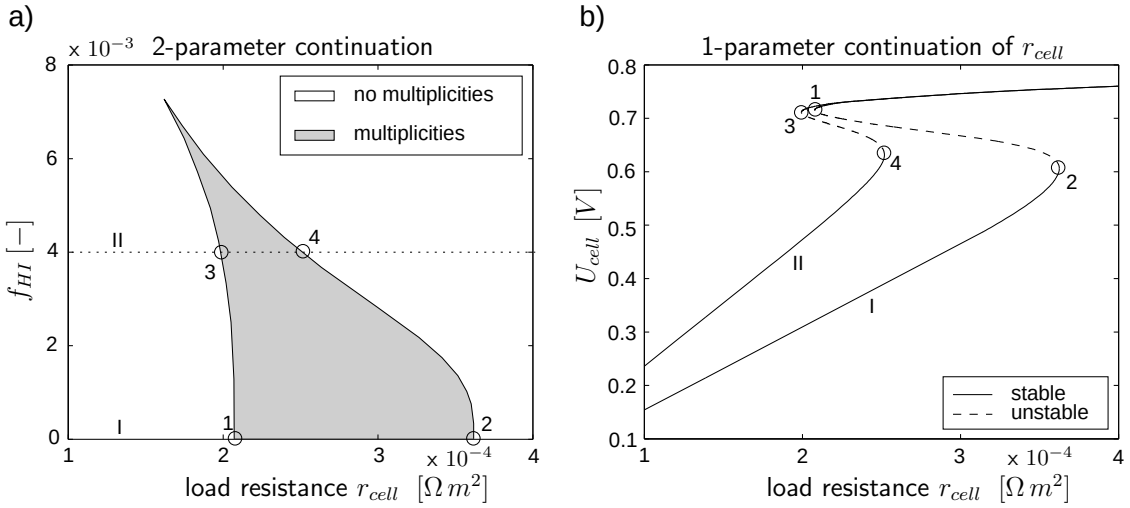

Figure 3.3: Influence of f_{HI} upon the found steady state multiplicity: a) shows the resulting parameter portrait when the load resistance r_{cell} and f_{HI} are varied. In b), two 1-parameter continuations corresponding to a) are shown.

Influence of the porosity. In the next step, the influence of the porosity upon the multiplicity is analyzed by a bifurcation analysis of the parameter π. The other parameters in Table 2.1 are held at their nominal values, while the results are shown

in Fig. 3.4. In case I, the porosity π is at its nominal value: $\pi = 0.4$. From Fig. 3.4a we can see that there is a multiplicity region between points 1 and 2. In Fig. 3.4b the corresponding 1-parameter continuation of r_{cell} is depicted, where the three possible steady states between 1 and 2 are clearly visible. For case II, the porosity π is decreased to 0.3. In Fig. 3.4a there is a multiplicity region recognizable between points 3 and 4. In Fig. 3.4b the corresponding 1-parameter continuation is shown. The multiplicity region for case II is clearly larger than that for case I. The physical explanation for this effect is that a lower porosity π leads to a higher transport resistance for the gas diffusion in the GDLs and, at the cathode side, to a lower oxygen content in the catalyst layer. This results in a lower possible cell current that can be drawn from the fuel cell. Therefore, the whole multiplicity is shifted to smaller cell currents, i.e. to larger values for the load resistances and to a larger area for the multiplicity in terms of the load resistance.

In summary, the magnitude of the multiplicity region rises with decreasing porosity and vice versa. This means that a desirable high compression of the fuel cell layers in order to decrease the contact resistances and therefore the ohmic losses between them can result in a lower porosity and an increased magnitude of the region of steady state multiplicities.

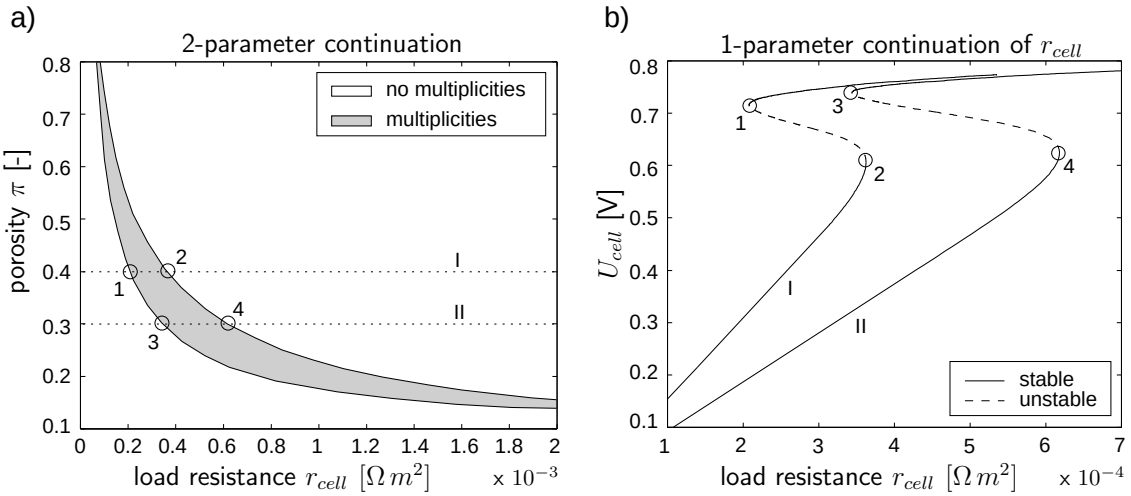

Figure 3.4: Influence of the porosity π on the multiplicity: a) shows the resulting parameter portrait when the load resistance and the porosity are changed. In b), two 1-parameter continuations corresponding to a) are depicted.

Influence of the permeability. Finally, the influence of the permeability upon the multiplicity is examined. This is done by a bifurcation analysis of the parameter K. The other parameters in Table 2.1 are set to their nominal values again. The results of this study are shown in Fig. 3.5. In case I the permeability K is at its nominal value: $K = 10^{-14}\, m^2$. In Fig. 3.5a a multiplicity region between points

1 and 2 can be seen and the corresponding 1-parameter continuation is given in Fig. 3.5b. For case II, the permeability is decreased, i.e. $K = 3 \cdot 10^{-15}$, to a order of magnitude which is used e.g. in [80]. In Fig. 3.5a we can see a multiplicity region between points 3 and 4 which is clearly larger than that for case I. This is confirmed if we compare the 1-parameter continuations I and II in Fig. 3.5b. The physical explanation for this effect is a lower liquid water flow towards the GDLs due to a lower permeability. This results in a decreased liquid water saturation in the GDLs and is especially the case for steady states with a former high liquid water saturation, i.e. the unstable steady states in Fig. 3.1c. The consequence at the cathode side is a smaller transport resistance of oxygen which leads to a higher oxygen content there. Finally, a larger area of multiplicity in terms of the load resistance is the result.

In summary, the magnitude of the multiplicity region increases with decreasing permeability of the fuel cell model and vice versa. This means that a desirable high compression of the fuel cell layers could decrease the permeability and therefore could lead to an increased magnitude of the steady state multiplicity region.

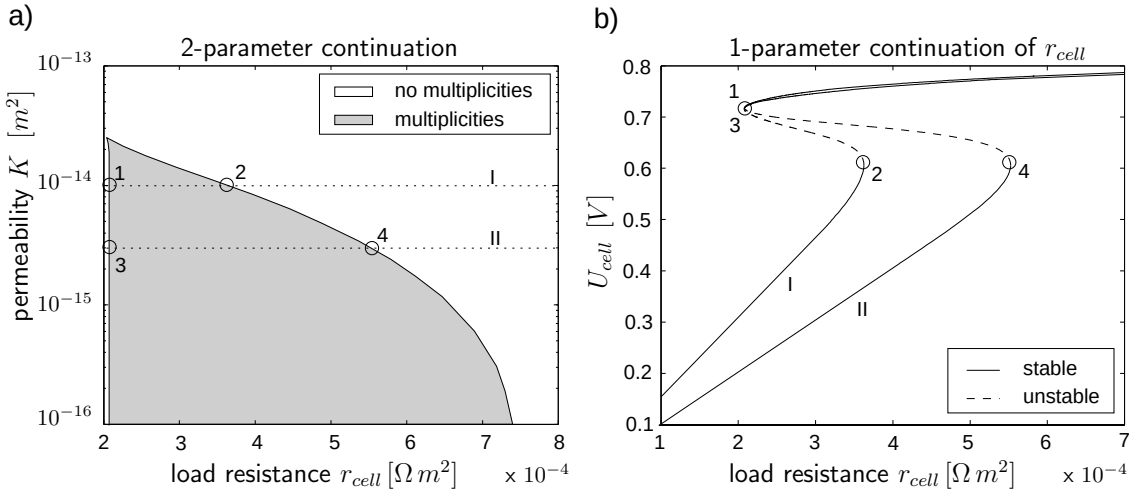

Figure 3.5: Influence of the permeability upon the multiplicity: a) shows the resulting parameter portrait when the load resistance and the permeability are changed. In b), two 1-parameter continuations corresponding to a) are shown.

3.2 Dynamic simulation

Finally, the fuel cell model is tested in a dynamic simulation in order to characterize the transient behavior of the fuel cell under conditions where multiple steady states occur. For this purpose, the fuel cell model is operated in rheostatic mode again. The load resistance r_{cell} serves as input and is kept piecewise constant. Figure 3.6 shows the results of the simulation. At the start of the simulation, the fuel cell model is in steady state $\boxed{1}$ with $r_{cell} = r_{cell}^I$. First of all, the load resistance is

decreased to $r_{cell} = r_{cell}^{II}$. The transition to steady state $\boxed{2}$ involves an increase in the liquid water saturation (Fig. 3.6d) and a drop in the cell voltage (Fig. 3.6c). This demands about 10^4 seconds due to the slow increase in $\tilde{s}_4^l$. After that, the load resistance is set back to $r_{cell} = r_{cell}^{I}$. Note the fast transition from steady state $\boxed{2}$ to $\boxed{3}$, because no significant liquid water decrease is involved (Fig. 3.6c,d). In the next step, the load resistance is increased to $r_{cell} = r_{cell}^{III}$. The following transition from steady state $\boxed{3}$ to $\boxed{4}$ includes a time-consuming significant decrease in the liquid water saturation (Fig. 3.6d) which demands about 10^4 seconds again. The last step is back to the first load resistance. Note again the small transition time to get from steady state $\boxed{4}$ to $\boxed{1}$ due to the negligible liquid water dynamic there.

In summary, the performed simulation shows that the transition time increases dramatically if a transition is done from one stable branch of the found steady state multiplicity to the other stable branch due to the slow liquid water dynamic. A fuel cell operation under such sluggish dynamic conditions is not desirable and should be clearly avoided.

3.3 Summary

In this chapter a bifurcation analysis is performed for a rigorous two-phase PEMFC model. A steady state multiplicity is found during this analysis. It turns out that it results from different oxygen contents in the fuel cell due to different saturation levels of liquid water inside the PEMFC. After the explanation, the multiplicity's dependency on several practical relevant fuel cell parameters is investigated. This is done for the anodic and cathodic humidity in the gas bulk, the fraction of hydrophilic pores as well as for the porosity and the permeability of the gas diffusion and catalyst layers. It is shown that the multiplicity becomes larger for high humidities in the bulks, for low fractions of hydrophilic pores and for small values of porosity and permeability. The multiplicity is also studied in a dynamic simulation in order characterize the transitional behavior there. It is found that the dynamic behavior of the fuel cell becomes quite sluggish due to the slow liquid water dynamics near the multiplicity. In summary, the found, explained and outlined nonlinear behavior increases the knowledge about two-phase PEMFCs especially at flooding conditions and can therefore be used to improve the performance of these fuel cells there.

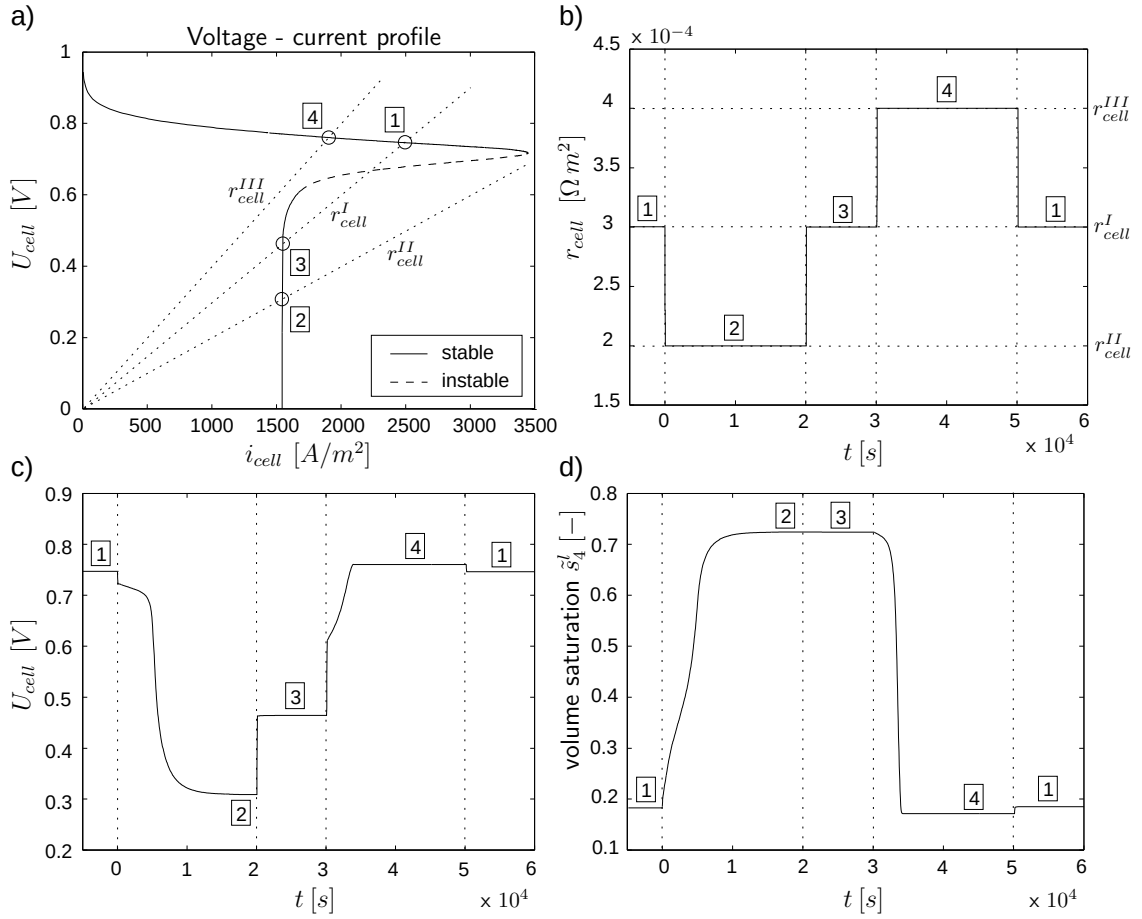

Figure 3.6: Step response of the fuel cell model: a) shows the steady state voltage-current profile and the three considered load cases: $r_{cell} = r^I_{cell}, r^{II}_{cell}, r^{III}_{cell}$. In b), c) and d) the time plots of the load resistance, the cell voltage and the liquid water saturation at the left border of the cathodic catalyst layer are displayed. The framed numbers mark the steady states reached during the dynamic simulation. Note the large time scale in b), c) and d).

CHAPTER 4

Model reduction of two-phase PEM fuel cells

In the previous chapter a bifurcation analysis for a two-phase PEMFC model was carried out. A stationary multiplicity was found that is connected to the flooding of the fuel cell. The avoidance of flooding and drying out is of major interest in the operation of PEMFCs as was pointed out in the first chapter and a model-based process control strategy is a suitable way to do this, e.g. [27, 58]. Such an approach can lead to a better fuel cell performance and increased efficiency of the system, but requires an appropriate dynamic fuel cell model. There are two counteracting conditions that have to be fulfilled. On the one hand, the model should be detailed enough to capture the main process characteristics. On the other hand, it should be simple enough to remain solvable in a real-time environment. Today, the majority of the dynamic two-phase PEMFC models in literature like [1, 82, 90] usually consist of algebraic and partial differential equations in one or more space coordinates, which are too complex for many process control purposes. Up to now there are only a few dynamic, mostly empirical, two-phase PEMFC models that could be used for model-based control approaches, like [24, 27]. The reduced model discussed in this chapter could be used as basis for the development of model-based control approaches for PEMFCs, especially to counteract flooding phenomena. The model is derived from the rigorous one-dimensional two-phase model in section 2.1 and incorporates the found nonlinear effects due to liquid water flooding. The result of this model reduction, the reduced two-phase model, has already been presented in section 2.2 and therefore the following section directly focuses on the comparison between detailed and reduced two-phase PEMFC model, while the last section in this chapter summarize the main points of the model reduction.

4.1 Model comparison

The basis of the model reduction are simulation studies performed during the bifurcation analysis in chapter 3. This analysis showed the occurrence of steady state multiplicities at cell flooding. The reduced model should now (I) capture these multiplicities, (II) be of low order and (III) show acceptable quantitative agreement with the detailed model. These three points form the aims of the following model comparison which is done in two steps. In a first step, the comparison is done by means of steady-state simulations in subsection 4.1.1, while in a second step the dynamic behavior of both models is shown in subsection 4.1.2.

4.1.1 Steady-state simulation

In this section the reduced model is compared to the detailed model in steady-state simulations. For this purpose, a bifurcation analysis of the reduced model is performed and brought into comparison to the results of the bifurcation analysis of the detailed model. This is done for two aspects. The first aspect is the influence of the activities in the gas bulks and the second one is the influence of the liquid water outflow on the fuel cell behavior.

Influence of the activities in the gas bulks. The activities of water vapor in the gas bulks are varied by changing the mass fractions of water vapor $c_{\epsilon,b}^{H_2O}$ there. The other varied parameter in this comparison, the fraction of hydrophilic pores f_{HI}, is at its nominal value given in Table 2.1. The results of the bifurcation analysis with the detailed model are shown in Fig. 4.1a,b and are taken from Fig. 3.2 in the last chapter. Figure 4.1a shows the bifurcation diagram where the area of multiplicity is highlighted in grey. Figure 4.1b displays three 1-parameter continuations of the load resistance r_{cell} for selected activities in the bulk shown in Fig. 4.1a. In Fig. 4.1c,d the influence of the activities upon the reduced model is shown. Figure 4.1c displays the bifurcation diagram and Fig. 4.1d shows the corresponding 1-parameter continuations. It can be seen that the bifurcation diagrams of the detailed (Fig. 4.1a) and the reduced model (Fig. 4.1c) look qualitatively very similar. There are some differences for smaller activities where the multiplicity region of the reduced model is smaller but the overall effect of the varying activities in the bulk upon the multiplicity is captured by the reduced model and can be reproduced by it. This is confirmed by the corresponding 1-parameter continuations in Fig. 4.1b and Fig. 4.1d.

Influence of the liquid water outflow of the cell. The liquid water outflow is varied by changing the fraction of hydrophilic pores, f_{HI}, while the other model parameters remain at their nominal values given in Table 2.1. The outcome of the bifurcation analysis for the detailed model is shown in Fig. 4.2a,b and is taken from Fig. 3.3 in the last chapter. Figure 4.2a depicts the bifurcation diagram, where the area of multiplicity is highlighted in grey and Fig. 4.2b shows two 1-

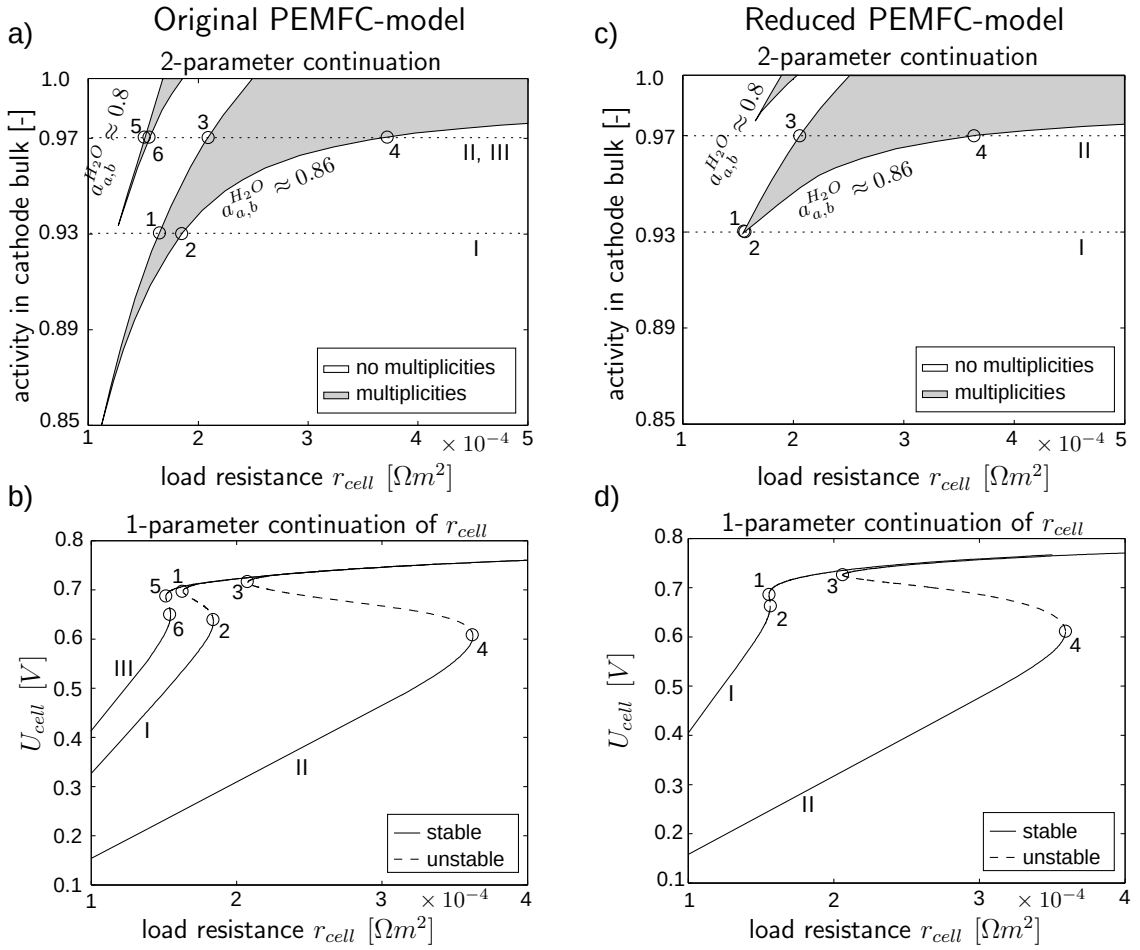

Figure 4.1: Comparison between detailed and reduced model with respect to the influence of the activities of water vapor in the gas bulks upon the multiplicity. In a) and c) the corresponding bifurcation diagrams for the detailed and reduced model are shown respectively. In b) and d) related 1-parameter continuations of steady-states are shown.

parameter continuations of r_{cell} for selected values of f_{HI}. The corresponding results of the bifurcation analysis with the reduced model are given in Fig. 4.2c,d, where Fig. 4.2c displays the bifurcation diagram and Fig. 4.2d displays the 1-parameter continuations. It can be seen that both bifurcation diagrams look qualitatively very similar with only small quantitative differences. This is also confirmed by the 1-parameter continuations in Fig. 4.2b and Fig. 4.2d.

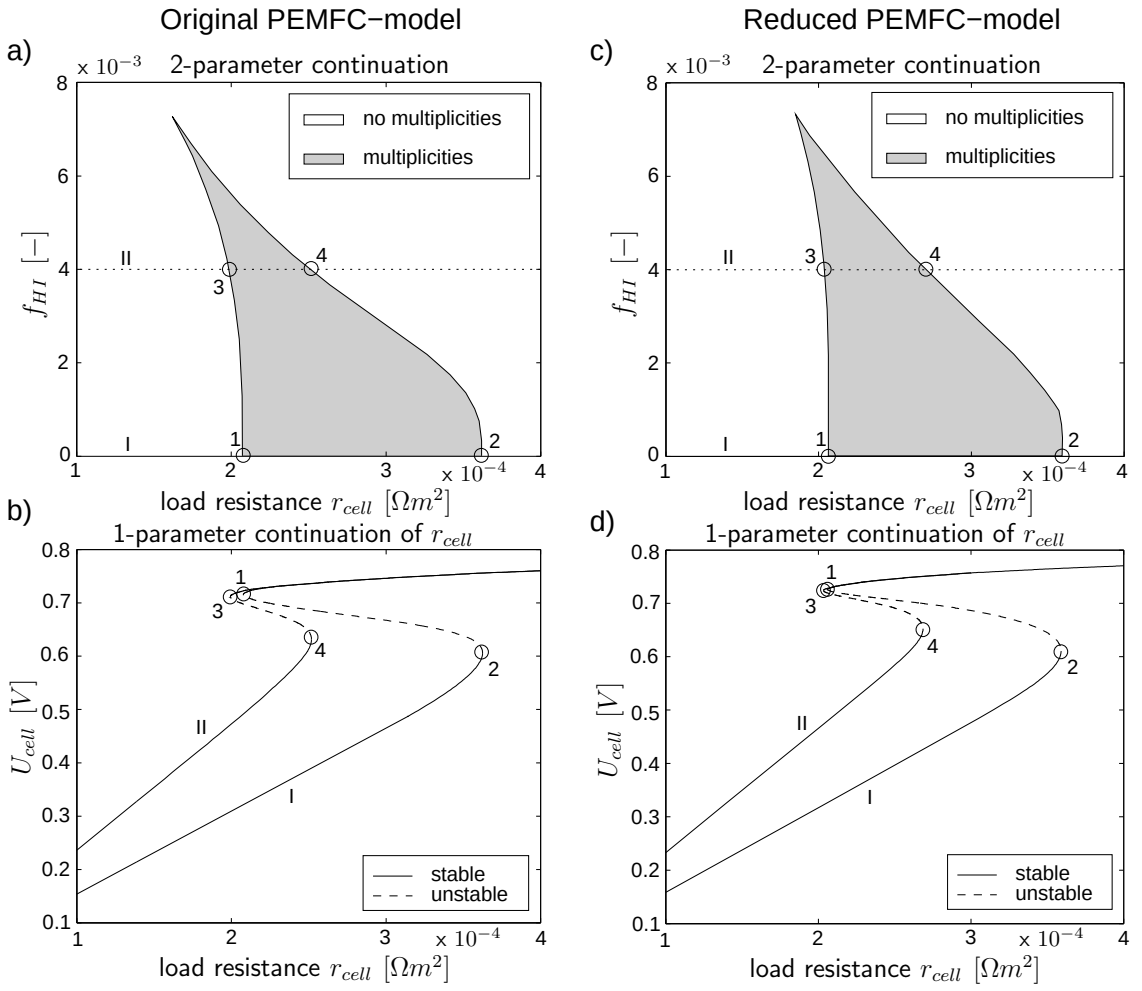

Figure 4.2: Comparison between detailed and reduced model with respect to the influence of the liquid water outflow upon the multiplicity. In a) and c) the corresponding bifurcation diagrams for the detailed and reduced model are shown respectively. In b) and d) related 1-parameter continuations of steady states are displayed.

4.1.2 Dynamic simulation

In this section the dynamic behavior of the reduced and detailed model is compared. For this purpose, both models are operated in rheostatic mode. The model param-

eters $c_{a,b}^{H_2O}$, $c_{c,b}^{H_2O}$ and f_{HI} used in the previous steady-state comparison are at their nominal values. Instead, the load resistance serves as input to both models and is kept piecewise constant. Figure 4.3 shows the stationary voltage-current profiles of both models together with the load lines r_{cell}^{I}, r_{cell}^{II} and r_{cell}^{III} reached by the load resistance r_{cell}, while the encircled points mark the encountered steady-states during the simulation. Figure 4.4 shows the transient behavior of both models for selected

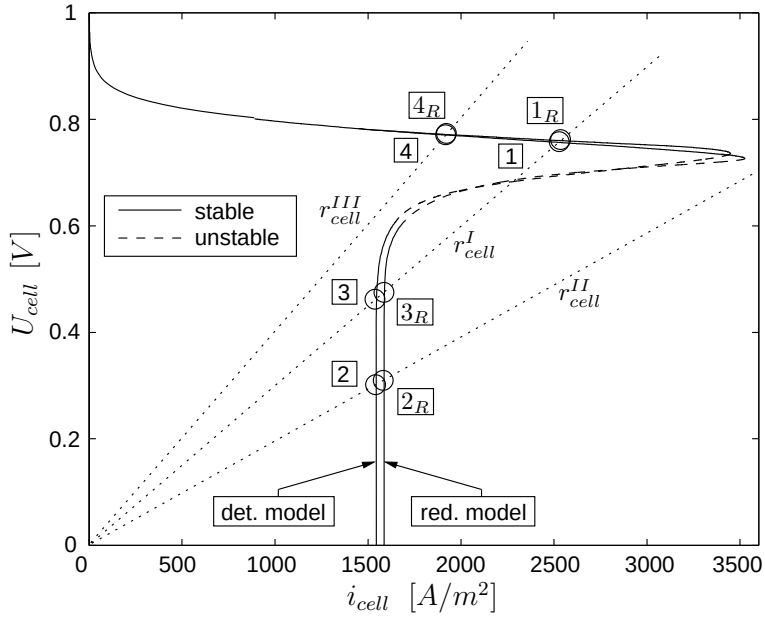

Figure 4.3: Stationary voltage-current profiles of the detailed and the reduced model. r_{cell}^{I}, r_{cell}^{II} and r_{cell}^{III} mark the load lines and the boxed numbers indicate the steady-states of the detailed and of the reduced model respectively.

fuel cell quantities. The simulation is started in steady-state $\boxed{1}$ and $\boxed{1_R}$ respectively with $r_{cell} = r_{cell}^{I}$. In a first step, the load resistance is decreased to $r_{cell} = r_{cell}^{II}$. This load change is accompanied by an increase in the liquid water saturation (Fig. 4.4b), a drop in the cell voltage (Fig. 4.4c) and a decrease in the cell current (Fig. 4.4d) until the steady-states $\boxed{2}$ and $\boxed{2_R}$ are reached. This transition is relatively slow due to the slow increase of the liquid water saturation. After that, the load resistance is set back to $r_{cell} = r_{cell}^{II}$ and the steady-states $\boxed{3}$ and $\boxed{3_R}$ are reached. This transition is quick because no significant change of the liquid water saturation is involved. In a next step, the load resistance is increased to $r_{cell} = r_{cell}^{III}$, where a time-consuming decrease of the liquid water saturation can be observed until the steady-states $\boxed{4}$ and $\boxed{4_R}$ are reached. Finally, the load resistance is set back to $r_{cell} = r_{cell}^{I}$ and both models end up in the steady-states at simulation start $\boxed{1}$ and $\boxed{1_R}$.

It can be seen from Fig. 4.4 that the dynamic behavior of both models is qualitatively the same. The slow liquid water dynamic is captured and in the case of the cell voltage (Fig. 4.4c) and the cell current (Fig. 4.4d) there is also a acceptable

quantitative agreement observable. The present steady state errors in the cell voltage and in the cell current especially at the steady states $\boxed{2_R}$ and $\boxed{3_R}$ are due to a too small liquid water saturation in the reduced model compared to the detailed model as can be seen from Fig. 4.4b. The reason for this difference is that the water vapor flow from the cell to the bulks is larger in the reduced model than it is in the detailed model. That is especially valid at the cathode side. This discrepancy in the vapor flows between both models comes from the fact that only one fitting parameter is used for the gradient approximation of the water vapor towards both bulks: β_{H_2O} in Eqn. 2.50 and Eqn. 2.52. If two fitting parameter were used for this purpose then these steady state errors would be clearly smaller.

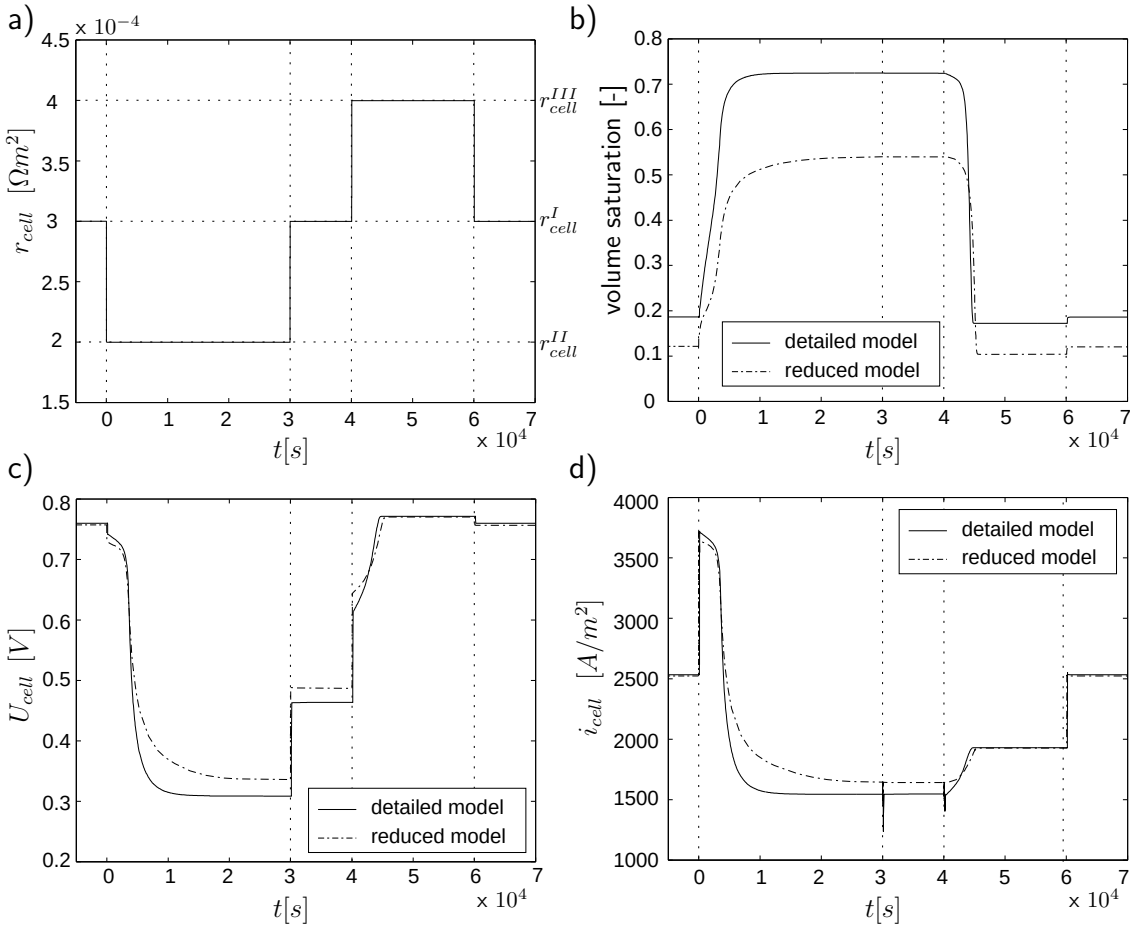

Figure 4.4: Step response of the detailed and the reduced fuel cell models; a) shows the input signal, the load resistance r_{cell}. In b), c) and d) the time plots of the liquid water saturation, the cell voltage and the cell current of both models are depicted.

4.2 Summary

In this chapter the model reduction of a two-phase PEMFC model is discussed. The steady-state multiplicity found in the original model is captured by the reduced model and can be reproduced by it. The simplified model is compared to the detailed one in steady-state and dynamic simulations where good qualitative and acceptable quantitative agreement is observed. The reduced model is of considerably lower order than the detailed model: The number of dynamic states is decreased from 130 of the detailed model to 5 of the reduced model. This means a reduction in the systems ODEs by a factor of 26 and a reduction in computation time that is in the same order of magnitude. Moreover, the reduced model order also eases the application of nonlinear control approaches to PEMFCs.

CHAPTER 5

Coupling behavior of PEM fuel cells and DC-DC converters

In the last chapter a reduced PEMFC model suitable for real-time process control was developed. Before the focus of this work changes towards the control design of PEMFCs, an intermediate step is taken in this chapter: The consideration of the so far not inspected coupling behavior of PEM fuel cells and DC-DC converters and its impact on the control design of fuel cells.

A fuel cell is electrically connected to its load via a power conditioning unit (PCU) [13]. This is done for the purpose of power transfer and power conversion. A PCU is generally made up from storage units and/or conversion units and is typically designed and operated according to requirements and characteristics of the load. While storage units buffer electrical energy, conversion units or converters are used to adapt the DC electricity from the fuel cell to the load's demands. Two types of converters are suitable for fuel cell operation: DC-DC and DC-AC converters. If a fuel cell is connected to a load via a PCU a complex dynamic system is created. Such a connection might lead to phenomena like multiplicities or oscillations, which are not present in the single systems. These phenomena can contribute to the performance of the whole system either in a positive or in a negative way. Therefore, a detailed investigation of the coupling is necessary to adapt and improve the design and operation of the whole system, especially if the original design was based on single separate subsystems. The coupling behavior of PEMFCs and PCUs is a current field of research. First results have been obtained for the coupling of PEMFCs and DC-AC converters [13, 25, 67]. The coupling of these systems leads to a ripple in the fuel cell current at a frequency that is twice the output frequency of the converter. This effect was analyzed in [13, 25, 67] and may contribute to fuel cell degradation. In [87] the control of a PEMFC connected to a buck-boost converter was investigated. Emphasis was on converter control and the coupling phenomena were hardly considered. This chapter tries to extend the results in literature by

analyzing the coupling phenomena between PEMFCs and DC-DC converters. For this model-based analysis, a quite simple PEMFC model incorporating the fast dynamics of the electrochemical reactions is sufficient, as motivated in chapter 2. This model has already been introduced in section 2.3 and therefore the following section immediately takes the next necessary step by introducing the used DC-DC converter models. After that, the results of this analysis are presented in section 5.2. Finally, the contents of this chapter are summarized in a conclusion.

5.1 Modeling of DC-DC converters

The purpose of DC-DC converters is the transformation of direct electricity. They are built up from power electronic devices and are operated as switched systems. Due to the switched operation, the output quantities of these systems show an unavoidable ripple which should be small. Three DC-DC converters are considered in this contribution: boost, buck and buck-boost converters [20]. The converters are assumed to be lossless and are modeled with resistive loads. In order to examine the coupling effects between PEMFC and converters due to switching, the DC-DC converters are modeled via switched differential equations. In the case of the boost converter (Fig. 5.1) they read:

$$L\,\dot{I}_{ind} = U_{in} - (1-q)\,U_{cap}\,, \tag{5.1}$$

$$C\,\dot{U}_{cap} = (1-q)\,I_{ind} - U_{cap}/R_{load}\,, \tag{5.2}$$

where I_{ind} is the inductor current, U_{cap} the capacitor voltage and q is the switching

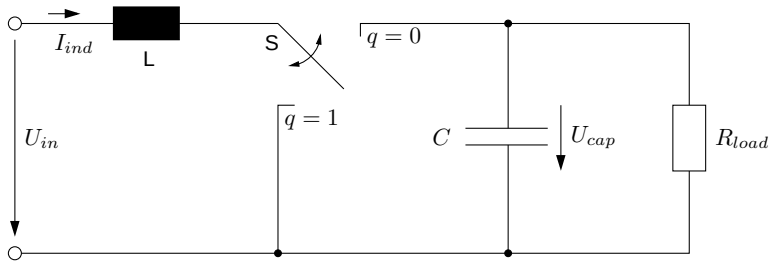

Figure 5.1: Lossless boost converter with resistive load.

function shown in Fig. 5.2. The load resistance R_{load} is assumed to be constant over one switching period T. Note that the input current of the converter, denoted with I_{in}, is equal to the inductor current: $I_{in} = I_{ind}$. Another widely used DC-DC converter is the buck converter (Fig. 5.3). It can be modeled with the following equations:

$$L\,\dot{I}_{ind} = q\,U_{in} - U_{cap}\,, \tag{5.3}$$

$$C\,\dot{U}_{cap} = I_{ind} - U_{cap}/R_{load}\,, \tag{5.4}$$

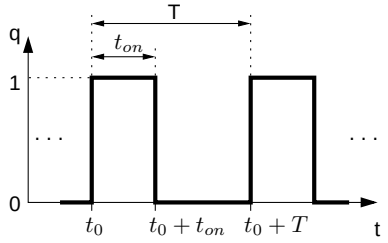

Figure 5.2: Duty cycle of the DC-DC converters.

where I_{ind} denotes the converter's inductor current and U_{cap} its capacitor voltage. The switching function q is the same as for the boost converter (Fig. 5.2). The input current I_{in} to the converter in this case is equal to: $I_{in} = q\, I_{ind}$. The buck-boost

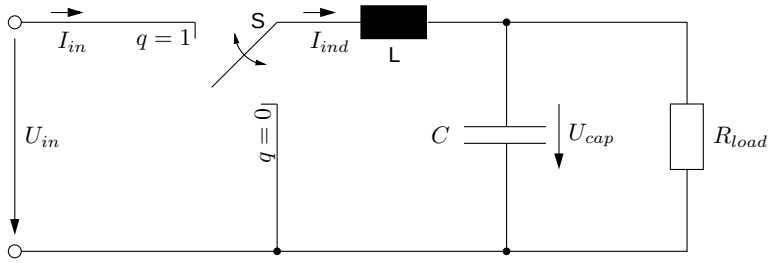

Figure 5.3: Lossless buck converter with resistive load.

converter (Fig. 5.4) is the last considered converter and can also be modeled by switched differential equations:

$$L\,\dot{I}_{ind} = q\,U_{in} + (1-q)\,U_{cap}\,, \tag{5.5}$$

$$C\,\dot{U}_{cap} = -(1-q)\,I_{ind} - U_{cap}/R_{load}\,. \tag{5.6}$$

Again, the inductor current of the converter is denoted by I_{ind}, the capacitor voltage by U_{cap} and the switching function q is given by Fig. 5.2. For the input current I_{in} the same statement as for the buck converter is true: $I_{in} = qI_{ind}$.

DC-DC converters can also be described by averaged model equations [20] if the intrinsic ripple is negligible. The structure of these equations is the same as for the switched models, only the time-dependent quantities are substituted by their averaged counterparts, where the average is taken over one duty cycle T, i.e.

$$\left[\overline{q}(t_0)\,,\,\overline{I}_{ind}(t_0)\,,\,\overline{U}_{cap}(t_0)\,,\,\overline{U}_{in}(t_0)\right] := \frac{1}{T}\int_{t_0}^{t_0+T} \left[q(t)\,,\,I_{ind}(t)\,,\,U_{cap}(t)\,,\,U_{in}(t)\right]\,dt\,. \tag{5.7}$$

The input current I_{in} is also integrated to be $\overline{I}_{in}(t_0) = \overline{I}_{ind}(t_0)$ for the boost and $\overline{I}_{in}(t_0) = \overline{q}(t_0)\,\overline{I}_{ind}(t_0)$ for the buck and buck-boost converter. The averaged model

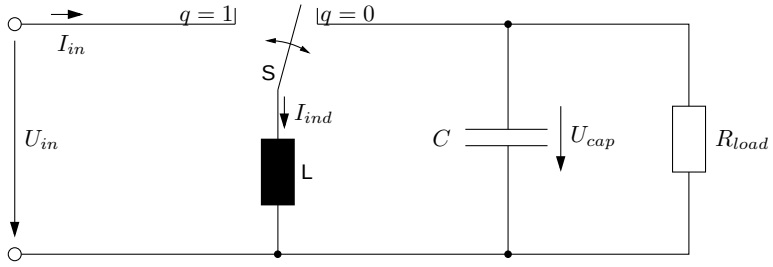

Figure 5.4: Lossless buck-boost converter with resistive load.

equations allow a simple characterization of the specified DC-DC converters in terms of their input/output behavior. In Fig. 5.5a the stationary output voltages $\overline{U}_{cap}$ of the three converters are shown. One can see that a boost (buck) converter can

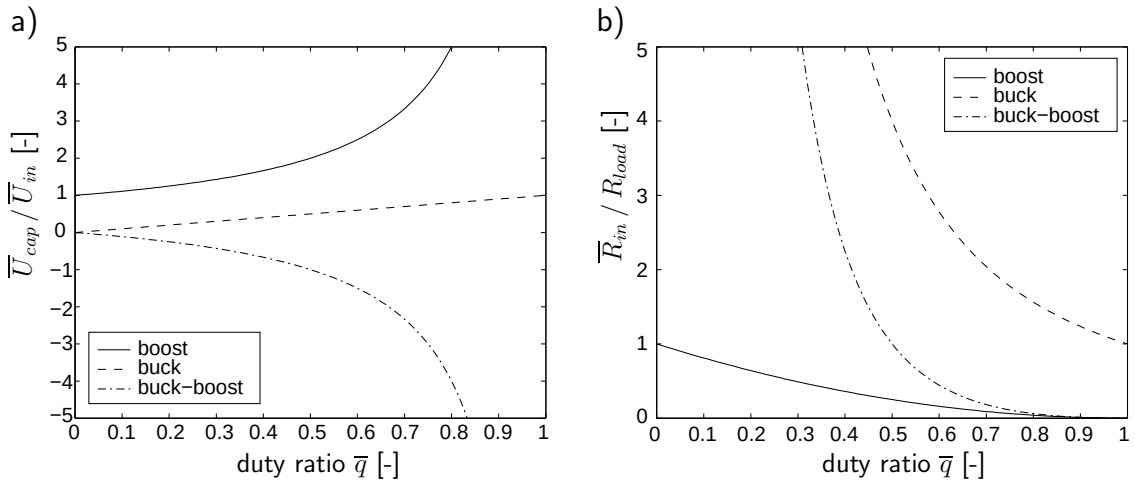

Figure 5.5: Stationary and averaged output voltages $\overline{U}_{cap}$ (a) and input resistances $\overline{R}_{in}$ (b) of boost, buck and buck-boost converters with respect to their duty ratio $\overline{q}$.

be used to produce an output voltage U_{cap} that is greater (smaller) in magnitude than the input voltage U_{in}. The buck-boost converter is a mixed form and is used to invert the output voltage U_{cap} and decrease or increase its magnitude with respect to the input voltage U_{in}. In Fig. 5.5b the stationary input resistances of the converters $\overline{R}_{in} := \overline{U}_{in}/\overline{I}_{in}$ are depicted.

5.2 Interconnection analysis of PEM fuel cell and DC-DC converters

In this section the connections between PEMFC and DC-DC converters is analyzed. First of all, the coupling conditions are specified. For the coupling between the PEM fuel cell (Eqn. 2.61-Eqn. 2.65) and the converters (Eqn. 5.1-Eqn. 5.6) the following conditions apply:

$$U_{cell} \triangleq U_{in} \quad \text{and} \quad i_{cell} \triangleq I_{in}/A \,. \tag{5.8}$$

With the above equation, the fuel cell and the converters are connected and a feedback of the converter's input current I_{in} to itself via the cell voltage U_{cell} (Eqn. 2.65) is established. It is the aim of this contribution to analyze the effect and extent of this feedback. This is done for each connection in three steps. In a first step, the effect of the converter ripple upon the PEMFC is shown and explained, while in the second step the found effect is discussed. In the last step, the overall behavior of the connected PEMFC - converter system is examined in order to check for the appearance of stationary multiplicities and oscillations due to the coupling.

5.2.1 PEMFC and Boost-converter

The interconnection analysis starts with the study of the coupling between the PEM fuel cell and the boost converter.

Effect of the converter ripple upon the PEMFC. In a first step, the effect of the converter ripple upon the PEMFC is shown. For this purpose, the PEMFC (Eqn. 2.61-Eqn. 2.63) and the boost converter model (Eqn. 5.1 and Eqn. 5.2) are coupled via Eqn. 5.8 and form a system of switched differential equations. This system is dynamically simulated using step changes of the load resistance R_{load} depicted in Fig. 5.6. The converter's duty ratio $\overline{q}$ is set to 0.2 and the other model parameters are kept constant at their nominal values given in Table 2.3. Three simulations are performed with the same initial value R^I_{load}. In simulation I the load resistance is kept constant at R^I_{load}, whereas in simulations II and III the load is stepped to R^{II}_{load} and R^{III}_{load} respectively. The simulation scenario can be further illustrated with the stationary voltage-current profile of the PEMFC together with the considered operating points OP_I, OP_{II} and OP_{III} shown inside of Fig. 5.6. The operating points are determined by the load resistance R_{load}. The relationship between the average load resistance of the fuel cell and the boost converter, i.e. $\overline{R}_{in}$ and R_{load}, can be derived from the averaged version of the boost converter model in Eqn. 5.1 and Eqn. 5.2 and reads:

$$\begin{aligned} L\,\dot{\overline{I}}_{ind}(t_0) &= \overline{U}_{in}(t_0) - (1-\overline{q}(t_0))\,\overline{U}_{cap}(t_0)\,, \\ C\,\dot{\overline{U}}_{cap}(t_0) &= (1-\overline{q}(t_0))\,\overline{I}_{ind}(t_0) - \overline{U}_{cap}(t_0)/R_{load}\,. \end{aligned}$$

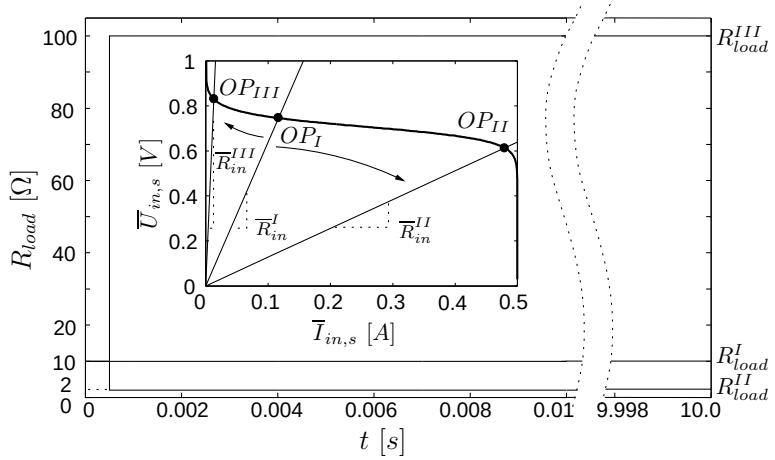

Figure 5.6: Time plot of the load resistance R_{load} and the stationary voltage-current profile of the PEM fuel cell with assigned operating points.

For the stationary operation of the converter one obtains: $\overline{U}_{in} = (1-\overline{q})\,\overline{U}_{cap}$ and $\overline{I}_{ind} = \overline{U}_{cap}/(1-\overline{q})R_{load}$. The average input resistance of the boost converter is given by $\overline{R}_{in} = \overline{U}_{in}/\overline{I}_{in}$ and with the dependency $\overline{I}_{in} = \overline{I}_{ind}$ one finally obtains from the previous statements $\overline{R}_{in} = R_{load}(1-\overline{q})^2$.

The simulation results are shown in Fig. 5.7 and Fig. 5.8. The diagrams are split into two parts. The first part shows the time plots from the simulation start to the settlement of the electrical transients of the coupled system. The second part shows stationary simulations after the transients for mass transport of oxygen and water vapor have settled. It can be seen, that during simulations I and II

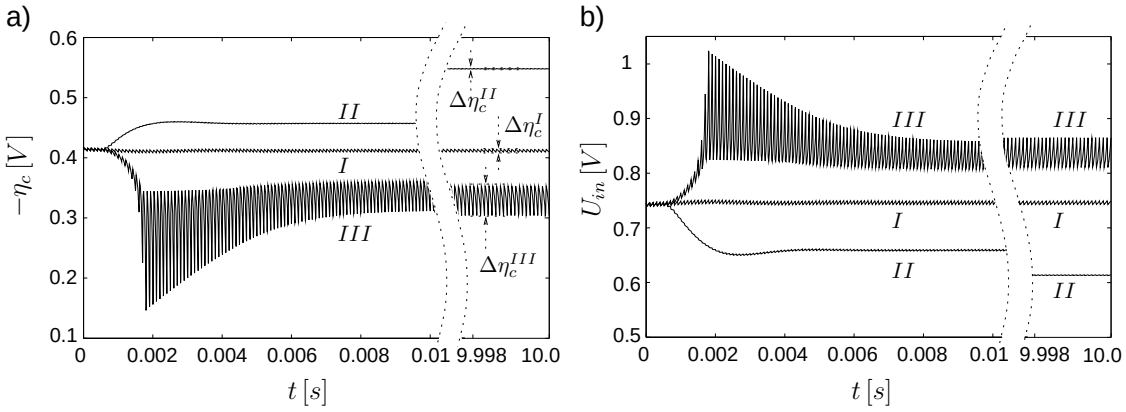

Figure 5.7: a) Step response of the overpotential η_c and b) the cell voltage and converter input voltage U_{in}.

no significant impact from the PEMFC to the boost converter or vice versa can be

found. After the applied step the simulation settles and finally reaches a steady state. The oscillations of the quantities are small and can be neglected.

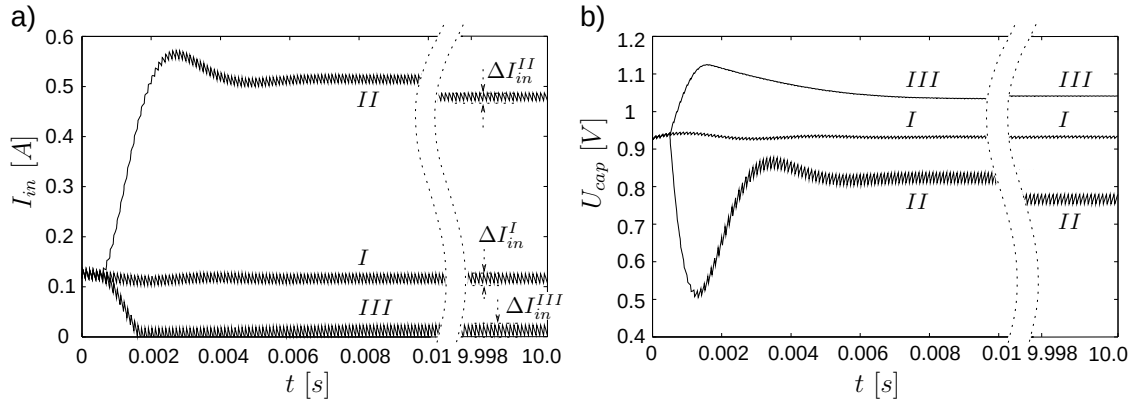

Figure 5.8: a) Step response of converter input and inductor current I_{in} and b) the capacitor and converter output voltage U_{cap}.

In contrast, if simulation III is considered, a clear interaction of PEMFC and converter can be observed. The overpotential η_c and the cell voltage U_{in} in Fig. 5.7 show relatively large oscillations compared to the cases I and II. The oscillations are present immediately after the applied step and also at steady state. This is not the case for the converter input current I_{in} and the capacitor voltage U_{cap} in Fig. 5.8. Both of them show only small oscillations in case III, similar to the simulation cases I and II. The given interaction is therefore one-sided in direction from boost converter to PEMFC and is located at small cell currents in the activation polarization region of the fuel cell (Fig. 5.6). The reason for this interaction can be found from Eqn. 2.63, the model equation of the overpotential. A linearization of this equation at an averaged and stationary operating point ($\overline{x}_{c,s}^{O_2}$, $\overline{x}_{c,s}^{H_2O}$, $\overline{\eta}_{c,s}$, $\overline{I}_{in,s}$, $\overline{U}_{cap,s}$) of the coupled system leads to

$$\underbrace{\frac{C_{dl}}{b\,\overline{I}_{in,s}/A}}_{\tau:=}\,\delta\dot{\eta}_c + \delta\eta_c = -\frac{\delta I_{in}}{b\,\overline{I}_{in,s}} \tag{5.9}$$

$$\text{with} \quad \overline{I}_{in,s} = A\, i_T^0\, \overline{x}_{c,s}^{O_2}\, \exp(-b\overline{\eta}_{c,s})\,, \tag{5.10}$$

where $\delta\eta_c$ and δI_{in} are the variations of the overpotential and the converter input current around the operating point respectively. It is assumed that the variation of the oxygen content $x_c^{O_2}$ due to the converter switching can be neglected. The variation δI_{in} of the converter input current is considered as an input quantity in Eqn. 5.9, which is independent from $\delta\eta_c$ because of the observed one-sided interaction from converter to PEMFC. Equation 5.9 is therefore a linear ordinary differential equation of first order with constant coefficients whose transient behavior is determined by its time constant τ. If the time constant τ is small compared to the given time

interval of the duty cycle T then the variation $\delta\eta_c$ can be approximately calculated by

$$\delta\eta_c \approx -\frac{1}{b\overline{I}_{in,s}}\delta I_{in} = -\frac{\partial(-\overline{\eta}_{c,s})}{\partial\overline{I}_{in,s}}\delta I_{in}\,. \tag{5.11}$$

This relationship is determined from the Tafel kinetic in Eqn. 5.10, where the above partial derivative denotes the sensitivity of the overpotential $-\overline{\eta}_{c,s}$ with respect to the cell current $\overline{I}_{in,s}$. It can be seen that the sensitivity increases with decreasing cell current. If the variation δI_{in} does not change very much at different cell currents $\overline{I}_{in,s}$, the change of the variation $\delta\eta_c$ can be approximately determined by the changed sensitivity. This is exactly the case for the three simulation experiments above. The oscillations ΔI_{in}^{ι}, $\iota \in \{I, II, III\}$ in the cell current (Fig. 5.8a) are nearly the same for all three simulation cases, but the average values are clearly different. For simulation case III the average cell current is the smallest resulting in the largest sensitivity of the three cases. The large oscillations in the overpotential for case III (Fig. 5.7a) are the consequence. In Fig. 5.9 the above statements are illustrated. The Tafel equation (Eqn. 5.10), the oscillation amplitudes of the cell current ΔI_{in}^{ι} (Fig. 5.8a) and the corresponding amplitudes of the overpotential $\Delta\eta_c^{\iota}$ (Fig. 5.7a) are shown for the three simulation cases I, II and III.

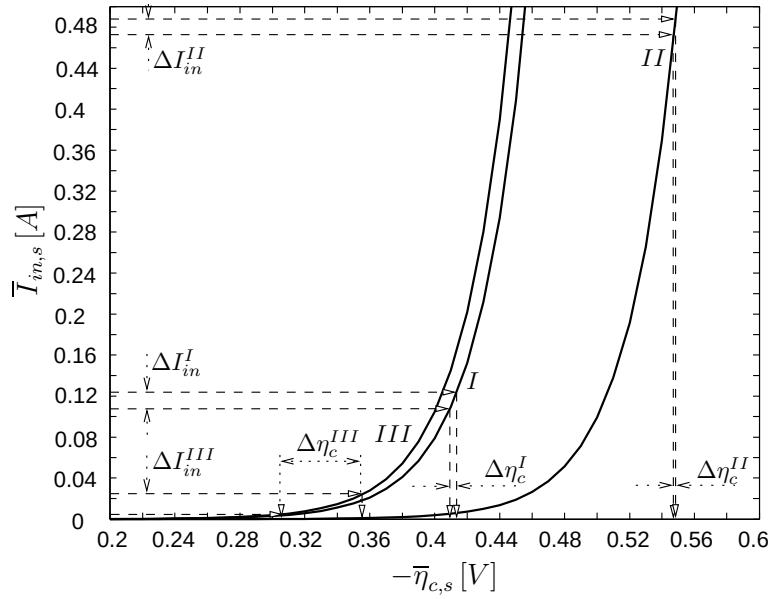

Figure 5.9: Tafel equation for simulation cases I, II and III.

We have seen that the reason for the large oscillation $\Delta\eta_c^{III}$ is a too small time constant τ with respect to the duty period T. From Eqn. 5.9 we can see, that the time constant τ is proportional to the double layer capacitance C_{dl} and (with Eqn. 5.11) to the sensitivity $\partial(-\overline{\eta}_{c,s})/\partial\overline{I}_{in,s}$. The sensitivity in simulation III is the

largest, so the double layer capacitance C_{dl} of the fuel cell is responsible for the small τ. Therefore, the oscillations in the activation polarization region of the PEMFC in III are caused by an insufficient adaption of the double layer capacitance C_{dl} and the duty period T to each other.

Discussion of the effect. We have shown and explained in the previous paragraphs that the converter ripple introduces oscillations in the activation polarization region of the fuel cell. This statement is true for the used double layer capacitance C_{dl} and duty period T, but it is also in general valid as long as the ratio between C_{dl} and T is less or equal to the given one. This means for example that we cannot increase T in order to decrease switching losses in the boost converter because this will result in larger oscillations in the fuel cell. This also means that if the fuel cell owns a larger double layer capacitance C_{dl} and we use the same duty period T the oscillations will vanish. If we go on and increase the duty period T (and the boost converter's inductivity L and capacitance C to stay at the same ripple in the output voltage U_{cap}) the oscillations will reoccur.

The impact of converter introduced oscillations in the overpotential is currently under research and up to now it is not clear if they lead to cell degradation, as long as no reactant depletion appears [17]. Anyway, in order to avoid oscillations in the fuel cell we have to take suitable measures which are presented in the following. For the above simulations we used a small double layer capacitance in the order of magnitude as in [5, 11]. In other publications like in [51, 61] a larger double layer capacitance in the PEMFC is observed. For the latter case, the oscillations in the fuel cell vanish for the given duty period and no further effort has to be taken to avoid them. In the first case, there are two simple possibilities to avoid oscillations. The first is to decrease the duty period T. This has a smaller variation ΔI_{in} of the cell current and a larger impact of the time constant τ within the time interval T as a consequence, but can also lead to larger switching losses in the converter. The second alternative is to increase the double layer capacitance C_{dl} of the PEMFC and therefore the time constant τ. The first point can be achieved via the control of the boost converter. After the boost converter has been designed [20] and the duty period T has been adjusted to meet the boost converter's requirements, a minimal cell current $\overline{I}_{in,s}^{min} \leq \overline{I}_{in,s}$ has to be specified. This puts an upper bound on the sensitivity in Eqn. 5.11. If the double layer capacitance and all other necessary parameters are roughly known then the relevant time constant $C_{dl}A/b\overline{I}_{in,s}^{min}$ can be estimated. If $T \gg C_{dl}A/b\overline{I}_{in,s}^{min}$ and the fuel cell is operated in the activation polarization region then oscillations are expected to appear. In order to avoid these oscillations, the duty period T can be decreased, e.g. $T \leq C_{dl}A/b\overline{I}_{in,s}^{min}$. The second possibility can be implemented for example by inserting a capacitor between PEMFC and boost converter. This leads to an increased double layer capacitance and is shown in appendix A.4.

Overall behavior of the coupled system. With the above suggestions the impact of the converter ripple can be suppressed and we can describe the connection between the PEMFC and the boost converter with averaged model equations, and

can finally check the overall behavior of this coupled system for the occurrence of stationary multiplicities and oscillations.

At first, we consider the stationary operation of PEMFC and boost converter. Therefore, the stationary and averaged relationship for the boost converter given in Fig. 5.5 is valid. Due to the coupling in Eqn. 5.8, the input resistance of the converter $\overline{R}_{in}$ serves as load resistance of the PEMFC, i.e. $\overline{V}_{cell}/\overline{I}_{cell} = \overline{U}_{in}\,A/\overline{I}_{in} = \overline{R}_{in}A$ and forces a rheostatic operation of the cell. Moreover, the mapping between the converter's input resistance $\overline{R}_{in}$ and the load resistance R_{load} is unique as is indicated in Fig. 5.5b. Therefore, no further stationary multiplicities are added by the coupling PEMFC and boost converter to the ones that are already present in a rheostatic operated PEM fuel cell [8, 28].

However, oscillations induced by the coupling are still possible. They appear if a Hopf bifurcation occurs due to the coupling. A Hopf bifurcation appears in a nonlinear system $\dot{\mathbf{z}} = \mathbf{f}(\mathbf{z}, \mathbf{p})$ if a pure imaginary pair of eigenvalues of the Jacobian matrix $\mathbf{J} = \partial\mathbf{f}/\partial\mathbf{z}$ evaluated at the steady state $(\mathbf{z}_0, \mathbf{p}_0)$ arises at the parameter $\mathbf{p}_0$. Therefore, in order to search for the onset of oscillations, we have to check the Jacobian matrix of the coupled system. For this purpose we start with the following averaged model of PEMFC and boost converter:

$$\dot{\overline{x}}_c^{O_2} = -\frac{A}{2\chi_c^{tot}\zeta_c V_c F}(1+\overline{x}_c^{O_2})\,\overline{i}_T + (x_{c,b}^{O_2} - \overline{x}_c^{O_2})\,\frac{\dot{V}_{c,b}}{V_c}\,, \tag{5.12}$$

$$\dot{\overline{x}}_c^{H_2O} = \frac{A}{2\chi_c^{tot}\zeta_c V_c F}(2-\overline{x}_c^{H_2O})\,\overline{i}_T + (x_{c,b}^{H_2O} - \overline{x}_{h_2o})\,\frac{\dot{V}_{c,b}}{V_c}\,, \tag{5.13}$$

$$\dot{\overline{\eta}}_c = \frac{1}{C_{dl}}\left(\overline{i}_T - \frac{\overline{I}_{ind}}{A}\right) \quad \text{with} \quad \overline{i}_T = i_T^0\,\overline{x}_c^{O_2}\,\exp(-b\overline{\eta}_c)\,, \tag{5.14}$$

$$\dot{\overline{I}}_{ind} = \frac{1}{L}\left(\Delta\phi_{eq} + \overline{\eta}_c - r_m(\overline{x}_c^{H_2O})\,\frac{\overline{I}_{ind}}{A}\right) - (1-\overline{q})\,\frac{\overline{U}_{cap}}{L}\,, \tag{5.15}$$

$$\dot{\overline{U}}_{cap} = \frac{1}{C}\left((1-\overline{q})\,\overline{I}_{ind} - \frac{\overline{U}_{cap}}{R_{load}}\right)\,. \tag{5.16}$$

It is derived by coupling Eqn. 2.61-Eqn. 5.2 using Eqn. 5.8 and averaging, like in Eqn. 5.7, the resulting model over one duty cycle. For this purpose, it is assumed that the states $x_c^{O_2}, x_c^{H_2O}, \eta_c, I_{ind}, U_{cap}$ are approximately constant during one duty cycle. This is a valid assumption due to the negligible impact of the converter ripple. The above system of equations includes averaged model equations for oxygen and water transport (Eqn. 5.12 and Eqn. 5.13). This mass transport typically shows transient times in the order of magnitude of seconds while the resonant behavior of the converter is in the order of magnitude of milli seconds and smaller. Due to this, we consider Eqn. 5.12 and Eqn. 5.13 as static and use only Eqn. 5.14 till Eqn. 5.16 to search for the appearance of a Hopf bifurcation. The first step in order to detect a Hopf bifurcation is the calculation of the Jacobian matrix. If we calculate the Jacobian matrix of Eqn. 5.14 till Eqn. 5.16 at the steady state ($\overline{x}_{c,s}^{O_2}$, $\overline{x}_{c,s}^{H_2O}$, $\overline{\eta}_{c,s}$,

$\overline{I}_{ind,s}$, $\overline{U}_{cap,s}$, $R_{load,s}$, $\overline{q}_s$) we get

$$\mathbf{J} := \begin{bmatrix} -b_{11} & -b_{12} & 0 \\ b_{21} & -b_{22} & -b_{23} \\ 0 & b_{32} & -b_{33} \end{bmatrix} = \begin{bmatrix} -b\overline{I}_{ind,s}/AC_{dl} & -1/AC_{dl} & 0 \\ 1/L & -r_m(\overline{x}_{c,s}^{H_2O})/AL & -(1-\overline{q}_s)/L \\ 0 & (1-\overline{q}_s)/C & -1/R_{load,s}C \end{bmatrix}. \tag{5.17}$$

The duty ratio $\overline{q}_s$ of the boost converter is typically between $0 \leq \overline{q}_s < 1$ and therefore, the coefficients b_{ij} of $\mathbf{J}$ are always greater than zero. In the next step, we have to check the location of the eigenvalues of the Jacobian matrix $\mathbf{J}$. The eigenvalues of $\mathbf{J}$ are the roots of the characteristic polynomial $P(\lambda) = det(\lambda\mathbf{I} - \mathbf{J})$ which is given by

$$P(\lambda) = \lambda^3 + c_2\lambda^2 + c_1\lambda + c_0 \tag{5.18}$$

$$\text{with} \quad c_2 := b_{11} + b_{22} + b_{33}\,, \tag{5.19}$$

$$c_1 := b_{11}b_{22} + b_{11}b_{33} + b_{22}b_{33} + b_{23}b_{32} + b_{12}b_{21}\,, \tag{5.20}$$

$$c_0 := b_{11}b_{22}b_{33} + b_{11}b_{32}b_{23} + b_{21}b_{12}b_{33}\,. \tag{5.21}$$

The location of the roots of $P(\lambda)$ can be determined with the criterion of LIÉNARD-CHIPART [49]. The polynomial has only roots with negative real parts if the following necessary and sufficient conditions are fulfilled: $c_0 > 0$, $c_2 > 0$ and $c_2\,c_1 - c_0 > 0$. The first two conditions are fulfilled through Eqn. 5.19 and Eqn. 5.21, because the coefficients c_2, c_1 and c_0 of the polynomial are always positive. The third condition is also valid because of

$$\begin{aligned} c_2c_1 - c_0 = {} & b_{11}^2b_{22} + b_{11}^2b_{33} + b_{11}b_{12}b_{21} + b_{11}b_{22}^2 + b_{11}b_{22}b_{33} + b_{22}^2b_{33} + \\ & b_{22}b_{23}b_{32} + b_{12}b_{21}b_{22} + b_{11}b_{22}b_{33} + b_{11}b_{33}^2 + b_{22}b_{33}^2 + b_{23}b_{32}b_{33} > 0. \end{aligned} \tag{5.22}$$

Therefore, the characteristic polynomial $P(\lambda)$ (Jacobian matrix $\mathbf{J}$) has always roots (eigenvalues) with negative real parts and because of this, the connection between a PEMFC and a boost converter cannot lead to a Hopf bifurcation in the coupled PEMFC - boost converter system.

5.2.2 PEMFC and Buck-converter

After the previous analysis of PEMFC and boost converter, the coupling between the PEMFC and the buck converter is examined. This is done in three steps again.

Effect of the converter ripple upon the PEMFC. In the first step we consider the effect of the buck converter ripple upon the fuel cell. For this purpose, we couple the modeling equations of the PEMFC, i.e. Eqn. 2.61 - Eqn. 2.63 with the buck converter model in Eqn. 5.3 and Eqn. 5.4 via the coupling condition in Eqn. 5.8 and apply step changes of the duty ratio $\overline{q}$ again. The step changes are shown in Fig. 5.10. The load resistance R_{load} is chosen so that the fuel cell is operated close to the maximum power point. The other model parameters are at their nominal

values. Two simulations denoted with I and II are carried out. In simulation I the duty ratio $\overline{q}$ is kept constant at $\overline{q}_I$ and in II the duty ratio is stepped to $\overline{q}_{II}$. The simulation scenario can be further illustrated by the stationary voltage current profile of the fuel cell and the considered operating points OP_I and OP_{II}. It is shown inside of Fig. 5.10. The operating points are determined by the buck converter's input resistance $\overline{R}_{in}$ that depends on the duty ratio and the load resistance in the following manner: $\overline{R}_{in}^{\iota} = R_{load}/\overline{q}_{\iota}^2$ with $\iota \in \{I, II\}$. This relationship can be derived in an analogous manner from an averaged and stationary version of the buck converter model like it was done for the boost converter in section subsection 5.2.1.

The step responses are shown in Fig. 5.11 and Fig. 5.12. The diagrams are split into two parts. As in subsection 5.2.1, the first part of the diagrams show the fast dynamics due to electrical effects in the fuel cell, while the second part shows the long term behavior of the cell and includes the settling of the the mass transport transients. In simulation I the duty ratio is equal to $\overline{q} = \overline{q}_I = 1$. This means that

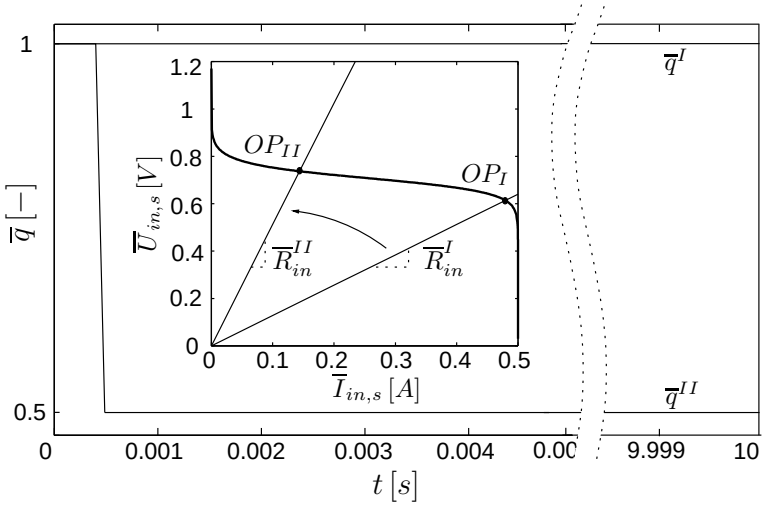

Figure 5.10: Time plot of duty ratio $\overline{q}$ and, inside, the stationary voltage-current profile of the fuel cell with considered operating points.

the switch S of the buck converter is always in position $q = 1$ and no oscillations occur. In contrast, if simulation II is considered, relative large oscillations in the overpotential η_c^{II} (Fig. 5.11), the cell current I_{in}^{II} (Fig. 5.12a) and the cell voltage U_{in}^{II} (Fig. 5.12b) appear. The large oscillations are present immediately after the applied step and also at the steady state. This is not the case for the inductor current I_{ind}^{II} (Fig. 5.12a) and the capacitor voltage U_{cap}^{II} (Fig. 5.12b) of the converter. Both of them show only small oscillations. The given interaction is therefore one-sided in direction from buck converter to the PEMFC. The reason for these large oscillations is due to the presence of the switching function q in the coupling of the fuel cell and buck converter: $i_{cell} = I_{in}/A = q\, I_{ind}/A$. This leads to a switched ODE for the

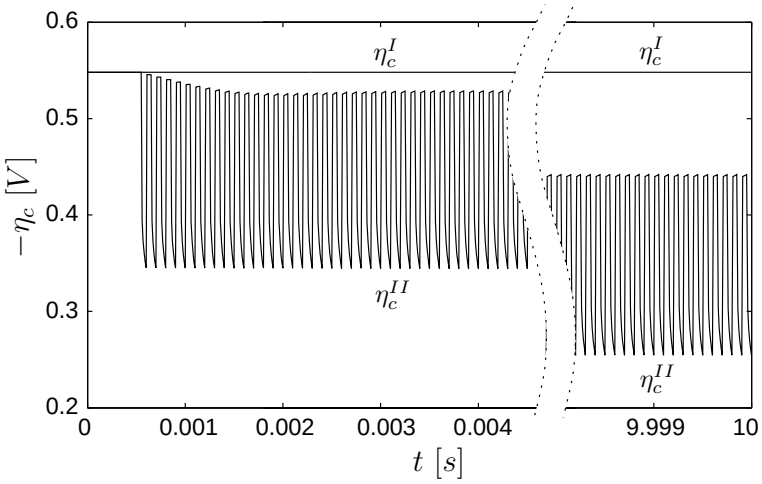

Figure 5.11: Time plot of the overvoltage η_c.

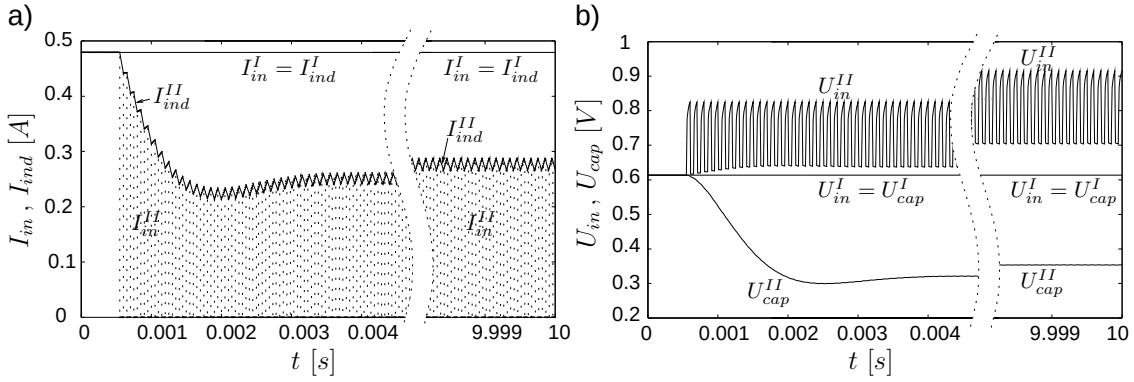

Figure 5.12: a) Step response of the inductor current I_{ind} and the cell and converter input current I_{in}. In b) the step responses of cell and converter input voltage U_{in} and capacitor, i.e. converter output voltage U_{cap} are shown.

overpotential:

$$C_{dl}\,\dot{\eta}_c = i_T^0 x_c^{O_2} \exp(-b\eta_c) - q\,I_{ind}/A \tag{5.23}$$

that causes the large oscillations in the overpotential and in the cell voltage.

Discussion of the effect. The above equation can be used to further discuss the oscillation amplitudes of the overpotential. With the above observation that the interaction is one-sided from buck converter to the fuel cell and the assumptions that the changes in the inductor current I_{ind} and the oxygen content $x_c^{O_2}$ are small over one duty period T and can be approximately described by their average values $\overline{I}_{ind}$ and $\overline{x}_c^{O_2}$, the following formula can be derived for the stationary oscillation amplitudes $\Delta\eta_c$ of the overpotential:

$$\Delta\eta_c = \frac{1}{b}\ln\left(1 + \frac{g(1-\overline{q})T\left(\frac{g}{h}\exp(-h\,\overline{q}\,T) - 1\right)}{\frac{g}{h}\left(\frac{g}{h}\exp(-h\,\overline{q}\,T) - 1\right) + \exp(-h\,\overline{q}\,T)\left(\frac{g}{h} - g(1-\overline{q})T\right)}\right) \tag{5.24}$$

$$\text{with} \quad g := b\,i_T^0\,\overline{x}_c^{O_2}\,/\,C_{dl}\,,\; h := b\,\overline{I}_{ind}\,/\,A\,C_{dl} \quad \text{and} \quad (1-\overline{q})Th > 1\,.$$

The derivation of this relationship is given in Appendix A.5 and it can be used to further investigate the oscillations in the fuel cell. Figure 5.13a shows the oscillation amplitudes $\Delta\eta_c$ calculated with Eqn. 5.24 at different duty ratios $\overline{q}$. The ratio of duty period and double layer capacitance: T/C_{dl} is used as parameter, while the other quantities are constant at their nominal values. It can be seen that a

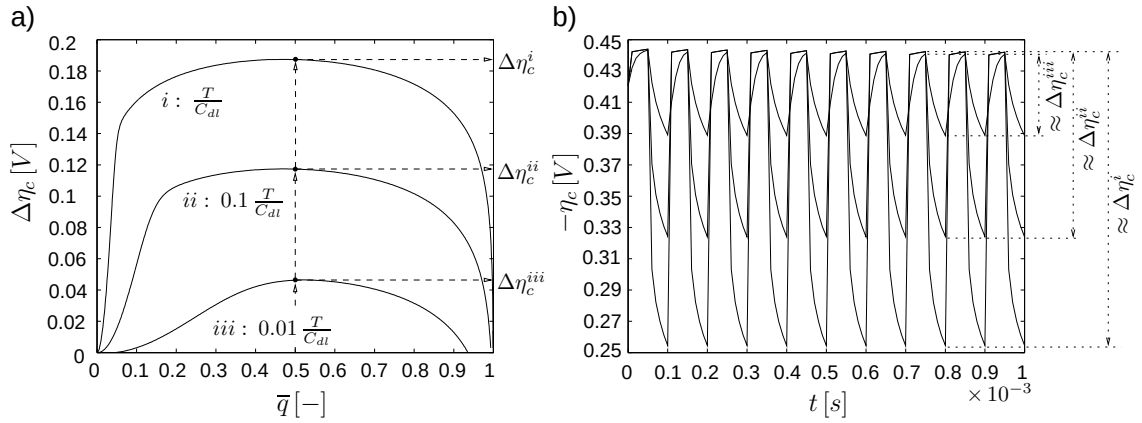

Figure 5.13: a) Stationary oscillation amplitudes $\Delta\eta_c$ of the overpotential with respect to the buck converter's duty ratio $\overline{q}$ at different ratios of duty period and double layer capacitance T/C_{dl}. In b) stationary simulations of the overpotential for the cases i to iii at a duty ratio $\overline{q} = 0.5$ are depicted.

decreasing ratio of T/C_{dl} leads to smaller oscillations in the overpotential and vice versa. Therefore, in order to reduce oscillations in the fuel cell, either the duty period

T of the buck converter has to be decreased or the double layer capacitance C_{dl} of the PEMFC has to be increased or both things have to be done. As was discussed in subsection 5.2.1, this can be achieved either by adjusting the switching period of the converter or by adding a capacitor. In Fig. 5.13b, an increased double layer capacitance is used. Shown are stationary simulation results of the overpotential η_c for the coupled PEMFC and buck converter model at a duty ratio of $\overline{q} = 0.5$. The duty period T is held constant and the double layer capacitance is increased from its nominal value in case i to $10C_{dl}$ in case ii and $100C_{dl}$ in case iii. It can be seen that the oscillation amplitudes of the overpotential decrease ($\Delta\eta_c^i > \Delta\eta_c^{ii} > \Delta\eta_c^{iii}$) as it is predicted in Fig. 5.13a.

The oscillations in the overpotential due to the coupling of PEMFC and buck converter may also be used to estimate parameters of the fuel cell. This may be useful for monitoring or control purposes of the PEMFC. Rather expensive to obtain are the parameters describing the reaction kinetics of the fuel cell. Their identification is usually done in experiments using the impedance spectroscopy [4, 56], the current interrupt technique [62] and the electrochemical parameter identification [14]. Equation 5.24 may also be useful for this purpose. For an estimation of the fuel cell's reaction kinetics the exchange current density together with the cell's oxygen content $i_T^0\,\overline{x}_c^{O_2}$, the exponent in the Tafel equation b and the double layer capacitance C_{dl} have to be determined. If we want to identify these parameters from Eqn. 5.24 we need to know the average inductor current $\overline{I}_{ind}$ and the oscillation amplitude $\Delta\eta_c$ of the overpotential, while the other quantities are rather well known. The quantity $\overline{I}_{ind}$ can be obtained by measuring and averaging the inductor current. The oscillation amplitude $\Delta\eta_c$ can be obtained by measuring the oscillation amplitude ΔU_{in} of the cell voltage. If the fuel cell is well humidified the ohmic and concentration losses are negligible and we have $\Delta\eta_c \approx \Delta U_{in}$.

Besides the actual measurements of $\overline{I}_{ind}$ and $\Delta\eta_c$, we have to analyze the sensitivity of these measurements with respect to the unknown parameters in Eqn. 5.24 in order to get an indication about the quality of the obtainable estimation results. For the double layer capacitance C_{dl} we can use Fig. 5.13 for this purpose. If we define the changes of the oscillation amplitude $\Delta\eta_c$ with respect to changes in C_{dl} at some fixed duty ratio $\overline{q}$ as sensitivity $|\Delta(\Delta\eta_c)/\Delta C_{dl}|_{\overline{q}}$ we can see from Fig. 5.13a that this sensitivity should be large enough for all duty ratios to get acceptable estimation results about the order of magnitude of C_{dl}. The sensitivity with respect to the exchange current density i_T^0 is analyzed in Fig. 5.14. If we consider the changes of the oscillation amplitude $\Delta\eta_c$ with respect to the changes in i_T^0 at some duty ratio $\overline{q}$ as sensitivity $|\Delta(\Delta\eta_c)/\Delta i_T^0|_{\overline{q}}$ it can be seen that this sensitivity is rather small and we cannot expect to get an acceptable indication about the order of magnitude of $i_T^0\,\overline{x}_c^{O_2}$ from Eqn. 5.24. Finally, in Fig. 5.15 the sensitivity with regard to the parameter b (Eqn. 2.64) is examined. Again, we consider the changes of the stationary oscillation amplitude $\Delta\eta_c$ with respect to the changes in b at a duty ratio $\overline{q}$ as sensitivity $|\Delta(\Delta\eta_c)/\Delta b|_{\overline{q}}$. It can be seen from Fig. 5.15 that this sensitivity should be large enough for duty ratios between 0.1 and 0.9 to get an acceptable estimation for the parameter b. The estimation results for b can be used to determine the transfer

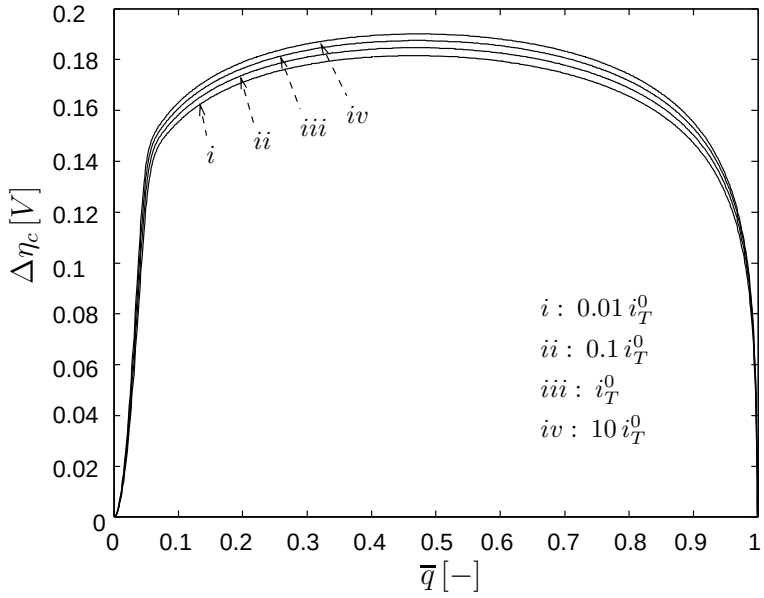

Figure 5.14: Stationary oscillation amplitudes $\Delta\eta_c$ of the overpotential with respect to the buck converter's duty ratio $\overline{q}$ at different exchange current densities i_T^0.

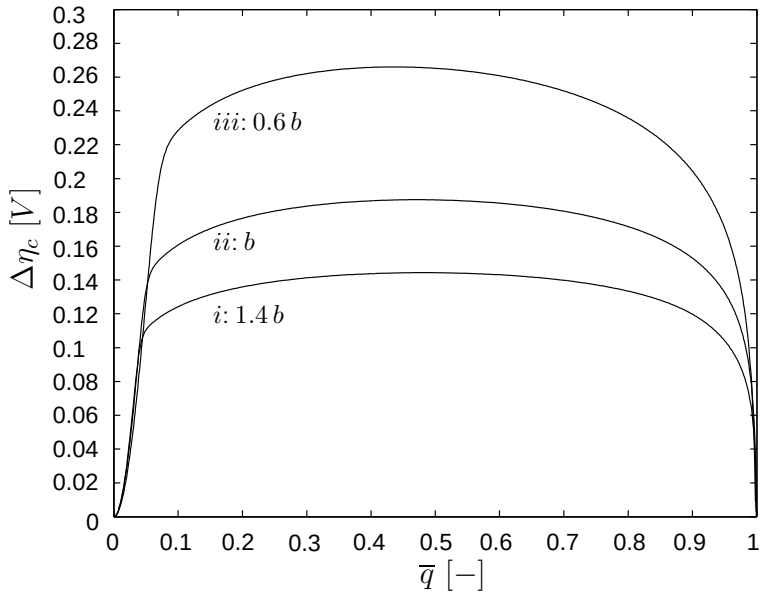

Figure 5.15: Stationary oscillation amplitudes $\Delta\eta_c$ of the overpotential with respect to the buck converter's duty ratio $\overline{q}$ at different values of b.

coefficient φ_c from Eqn. 2.64, since the relative change of ± 0.4 in b corresponds to a relative change of ∓ 0.2 in the transfer coefficient. To determine φ_c from Eqn. 2.64, the cell temperature ϑ has to be roughly known, e.g. from measurements.

In summary, the sensitivity analysis reveals that acceptable estimation results about the order of magnitude can be expected for the double layer capacitance C_{dl} and the parameter b. The exchange current density cannot be estimated due to its too small sensitivity. It should be noted, that due to this fact the precise value of the exchange current density as well as the precise value of the oxygen content in the cathodic catalyst is not necessary for an estimation of C_{dl} and b. The estimation requires the measurement of the average inductor current and the oscillation amplitude of the cell voltage at a highly humidified fuel cell. It should not be carried out at too small oscillation amplitudes $\Delta\eta_c$ to reduce the impact of the neglected inductor current ripple in Eqn. 5.24.

Overall behavior of the coupled system. If we suppress the oscillations in the fuel cell and neglect the impact of the buck converter ripple, we can describe and analyze the coupling between the PEMFC and the buck converter with averaged model equations in order to check the overall behavior of the coupling for the appearance of stationary multiplicities and oscillations.

First of all, the stationary operation of PEMFC and buck converter is considered. Therefore, the stationary and averaged relationship in Fig. 5.5 for the buck converter is valid. Like in the case of the PEMFC and the boost converter, the same reasoning is true and therefore the coupling between PEMFC and buck converter cannot introduce further stationary multiplicities as are already present in the PEMFC. However, oscillations induced by the coupling are still possible. In order to analyze the onset of oscillations we start with the following averaged model of PEMFC and buck converter:

$$\dot{\overline{x}}_c^{O_2} = -\frac{A}{2\chi_c^{tot}\zeta_c V_c F}(1+\overline{x}_c^{O_2})\,\overline{i}_T + (x_{c,b}^{O_2} - \overline{x}_c^{O_2})\,\frac{\dot{V}_{c,b}}{V_c}\,, \tag{5.25}$$

$$\dot{\overline{x}}_c^{H_2O} = \frac{A}{2\chi_c^{tot}\zeta_c V_c F}(2-\overline{x}_c^{H_2O})\,\overline{i}_T + (x_{c,b}^{H_2O} - \overline{x}_c^{H_2O})\,\frac{\dot{V}_{c,b}}{V_c}\,, \tag{5.26}$$

$$\dot{\overline{\eta}}_c = \frac{1}{C_{dl}}\left(\overline{i}_T - \overline{q}\,\frac{\overline{I}_{ind}}{A}\right) \quad \text{with} \quad \overline{i}_T = i_T^0\,\overline{x}_c^{O_2}\,\exp(-b\overline{\eta}_c)\,, \tag{5.27}$$

$$\dot{\overline{I}}_{ind} = \frac{\overline{q}}{L}\left(\Delta\phi_{eq} + \overline{\eta}_c - r_m(\overline{x}_c^{H_2O})\,\overline{q}\,\frac{\overline{I}_{ind}}{A}\right) - \frac{\overline{U}_{cap}}{L}\,, \tag{5.28}$$

$$\dot{\overline{U}}_{cap} = \frac{1}{C}\left(\overline{I}_{ind} - \frac{\overline{U}_{cap}}{R_{load}}\right)\,. \tag{5.29}$$

It is derived by coupling the model equations of the PEMFC (Eqn. 2.61-Eqn. 2.63) and the buck converter (Eqn. 5.3, Eqn. 5.4) via Eqn. 5.8 and averaging the resulting equations over one duty cycle. This is done in the same way as for the boost converter above. Like there, we consider the equations for the mass transport (Eqn. 5.25, Eqn. 5.26) as static and use only the averaged model equations for the fuel cell

kinetics and the boost converter model, i.e. Eqn. 5.27 till Eqn. 5.29. The Jacobian matrix of these equations evaluated at the steady state ($\overline{x}_{c,s}^{O_2}$, $\overline{x}_{c,s}^{H_2O}$, $\overline{\eta}_{c,s}$, $\overline{I}_{ind,s}$, $\overline{U}_{cap,s}$, $R_{load,s}$, $\overline{q}_s$) is given by

$$\begin{aligned}\mathbf{J} :&= \begin{bmatrix} -b_{11} & -b_{12} & 0 \\ b_{21} & -b_{22} & -b_{23} \\ 0 & b_{32} & -b_{33} \end{bmatrix} \\ &= \begin{bmatrix} -b\,\overline{q}_s\overline{I}_{ind,s}/AC_{dl} & -\overline{q}_s/AC_{dl} & 0 \\ \overline{q}_s/L & -\overline{q}_s^2\, r_m(\overline{x}_{c,s}^{H_2O})/AL & -1/L \\ 0 & 1/C & -1/R_{load,s}C \end{bmatrix}. \end{aligned} \tag{5.30}$$

The duty ratio for a buck converter is typically between $0 < \overline{q}_s \leq 1$. With this, the coefficients b_{ij} in $\mathbf{J}$ are always positive and therefore the same reasoning as in the previous analysis of PEMFC and boost converter is true: The connection between a PEMFC and a buck converter cannot introduce a Hopf bifurcation in the coupled PEMFC - buck converter system.

5.2.3 PEMFC and Buck-Boost-Converter

Finally in this chapter, the coupling behavior of the PEMFC with the last considered converter, the buck-boost converter, is examined.

Effect of the converter ripple upon the PEMFC. Like in the previous two analysis, the effect of the converter ripple upon the fuel cell is considered in a first step. This is done by analyzing the coupled system of switched differential equations made up from the PEMFC (Eqn. 2.61-Eqn. 2.63) and the switched buck-boost converter model (Eqn. 5.5, Eqn. 5.6). The analysis reveals that the buck-boost converter introduces oscillations in the fuel cell in the same way as the buck converter does. As in this previous case, the reason is due to the presence of the switching function q in the coupling of the fuel cell and the buck-boost converter: $i_{cell} = q\, I_{ind}/A$. This leads to the same switched ODE for the overpotential (Eqn. 5.23) and causes the oscillations in the fuel cell.

Discussion of the effect. The formula for the oscillation amplitude $\Delta\eta_c$ in (Eqn. 5.24) can also be used to describe the stationary oscillations introduced by a buck-boost converter. Figure 5.16 shows the oscillation amplitude of the overpotential calculated with this formula at different duty ratios. The ratio of the duty period and the double layer capacitance T/C_{dl} is used as parameter and the load resistance R_{load} is set to $7\,\Omega$ while the other quantities remain constant at their nominal values. It can be seen from Fig. 5.16 that a decreasing ratio of T/C_{dl} leads to smaller oscillations in the overpotential and vice versa. This is the same qualitative behavior as in the case of the buck converter in subsection 5.2.2. Therefore, the same possibilities to reduce the oscillations are applicable.

The connection between the PEMFC and the buck-boost converter can also be used to estimate parameters of the fuel cell. We can use Eqn. 5.24 for this purpose

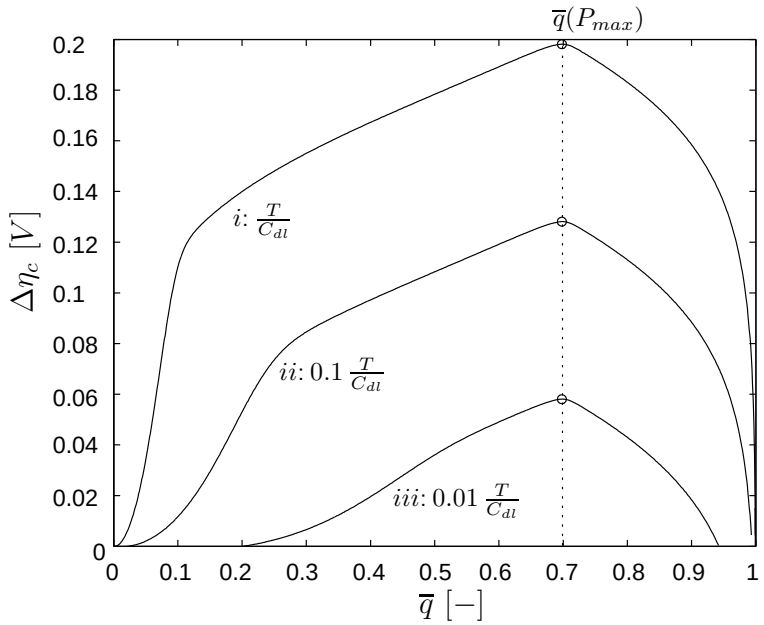

Figure 5.16: Stationary oscillation amplitudes of the overpotential with respect to the buck-boost converter's duty ratio $\overline{q}$ at different ratios of duty period and double layer capacitance T/C_{dl}. The quantity $\overline{q}(P_{max})$ denotes the duty ratio at the maximal cell power P_{max}.

again. In detail, the double layer capacitance C_{dl} and the exponent of the Tafel kinetics b can be estimated. In the case of the double layer capacitance this can be seen from Fig. 5.16. The sensitivity $|\Delta(\Delta\eta_c)/\Delta C_{dl}|_{\overline{q}}$ of the oscillation amplitude with respect to the double layer capacitance should be large enough to get acceptable estimation results for C_{dl}. In the case of the parameter b we can use Fig. 5.17. We see that the sensitivity $|\Delta(\Delta\eta_c)/\Delta b|_{\overline{q}}$ of the oscillation amplitude $\Delta\eta_c$ with respect to b should be large enough to get rough estimation results for b too.

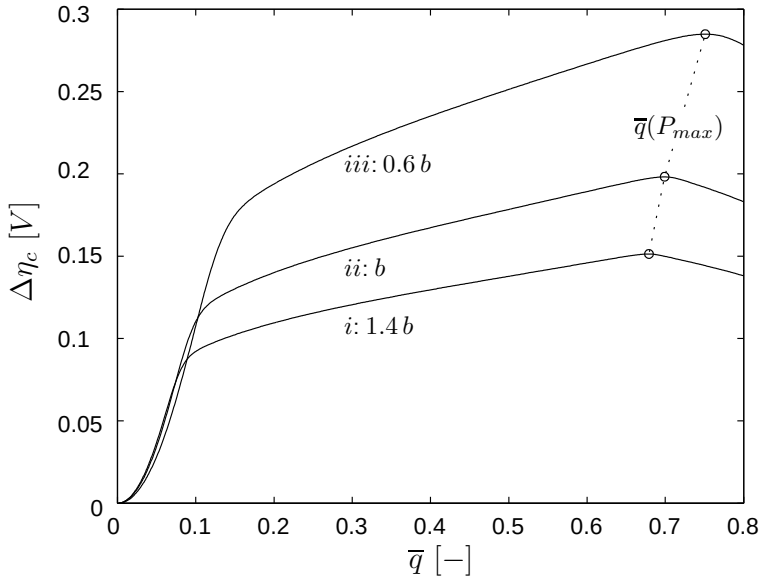

Figure 5.17: Stationary oscillation amplitudes $\Delta\eta_c$ of the overpotential with respect to the buck-boost converter's duty ratio $\overline{q}$ at different values of b. The quantity $a(P_{max})$ denotes the duty ratio at the maximal cell power P_{max}.

Overall behavior of the coupled system. If we reduce the oscillations and are able to neglect the impact of the converter ripple we can finally analyze the overall behavior of the coupled PEMFC and buck-boost converter with averaged model equations. First of all, the stationary operation of PEMFC and buck-boost converter is considered. Like for the previous two converters the same reasoning is true and therefore the coupling between PEMFC and buck-boost converter cannot introduce further stationary multiplicities as are already present in the PEMFC. However, oscillations are still possible and their appearance has to be analyzed. This is done by coupling and averaging the model equations of the PEMFC (Eqn. 2.61-Eqn. 2.63) and the buck-boost converter (Eqn. 5.5, Eqn. 5.6) in the same way like in the previous two cases. We obtain the same mass transport equations for oxygen and water vapor like in the case of the buck converter (Eqn. 5.25, Eqn. 5.26). Like there, we assume them as static and use only the model equations for the overpotential

and the buck-boost converter's inductor current and capacitor voltage:

$$\dot{\overline{\eta}}_c = \frac{1}{C_{dl}} \left(i_T^0 \, \overline{x}_c^{O_2} \, \exp(-b\overline{\eta}_c) - \overline{q} \, \frac{\overline{I}_{ind}}{A} \right) , \tag{5.31}$$

$$\dot{\overline{I}}_{ind} = \frac{\overline{q}}{L} \left(\Delta\phi_{eq} + \overline{\eta}_c - r_m(\overline{x}_c^{H_2O}) \, \overline{q} \, \frac{\overline{I}_{ind}}{A} \right) + (1 - \overline{q}) \frac{\overline{U}_{cap}}{L} , \tag{5.32}$$

$$\dot{\overline{U}}_{cap} = \frac{1}{C} \left(-(1 - \overline{q}) \overline{I}_{ind} - \frac{\overline{U}_{cap}}{R_{load}} \right) . \tag{5.33}$$

If we calculate the Jacobian matrix of the above system at the steady state ($\overline{x}_{c,s}^{O_2}$, $\overline{x}_{c,s}^{H_2O}$, $\overline{\eta}_{c,s}$, $\overline{I}_{ind,s}$, $\overline{U}_{cap,s}$, $R_{load,s}$, $\overline{q}_s$) we get

$$\begin{aligned} \mathbf{J} :&= \begin{bmatrix} -b_{11} & -b_{12} & 0 \\ b_{21} & -b_{22} & -\tilde{b}_{23} \\ 0 & \tilde{b}_{32} & -b_{33} \end{bmatrix} \\ &= \begin{bmatrix} -b\,\overline{q}_s \overline{I}_{ind,s}/AC_{dl} & -\overline{q}_s/AC_{dl} & 0 \\ \overline{q}_s/L & -\overline{q}_s^2 \, r_m(\overline{x}_{c,s}^{H_2O})/AL & (1-\overline{q}_s)/L \\ 0 & -(1-\overline{q}_s)/C & -1/R_{load,s}C \end{bmatrix} . \end{aligned} \tag{5.34}$$

The duty ratio of the buck-boost converter is typically between $0 < \overline{q}_s < 1$. With this, the coefficients b_{ij} of $\mathbf{J}$ are always positive with the exception of $\tilde{b}_{23}$ and $\tilde{b}_{32}$ which are always negative. If we calculate the characteristic polynomial of $\mathbf{J}$ we get the equations (Eqn. 5.18-Eqn. 5.21) with negative quantities $b_{23} = \tilde{b}_{23}$ and $b_{32} = \tilde{b}_{32}$. Despite this difference, the coefficients c_0, c_1, c_2 of the characteristic polynomial and the condition $c_2c_1 - c_0$ are still positive due to the fact that only the positive product $b_{23}b_{32} = \tilde{b}_{23}\tilde{b}_{32} > 0$ enters the determining equations (Eqn. 5.19-Eqn. 5.22). Therefore, the same conclusion as in the case of the PEMFC and the boost converter applys: The connection of a PEMFC and a buck-boost converter cannot induce a Hopf bifurcation in the coupled system.

5.3 Summary

The connection of PEM fuel cells and DC-DC converters is analyzed in this chapter. The analysis is done for common DC-DC converters like the boost, buck and buck-boost converters. First of all, the effect of the converter ripples are shown. They introduce oscillations in the fuel cell. Their origin is explained, discussed and possibilities for their suppression are given. In the case of the coupling between PEMFC and buck and buck-boost converter it is shown, that the oscillations may also be useful to estimate parameter of the fuel cell's Tafel kinetics.

Finally, the overall behaviors of the coupled systems are examined. This is a necessary step, because PEM fuel cells can show a complex nonlinear behavior like multiplicities, instabilities and oscillations shown in chapter 3 and in [28, 37, 40, 88]. The coupling with the DC-DC converters might have introduced additional nonlinear effects. We have shown mathematically that this is not the case: The connection

between PEM fuel cells and boost, buck and buck-boost converters can neither lead to stationary multiplicities nor to oscillations in the coupled systems. As a consequence, it is not necessary to develop integrated control approaches for the couplings. Instead, we can concentrate ourselves on the development of control strategies considering only the PEMFC and we can use existing control approaches for the DC-DC converters [20, 26, 46] in order to control both subsystems.

Although the PEMFC model used in this contribution is quite simple, the obtained results are also valid for PEMFC stacks in general. This is due to the fact that in PEMFC stacks the electrochemical reactions in the catalysts can also be described by the modeling approach we use in our analysis. Other transient effects that appear in PEMFC stacks like the mass transport of gases and liquid water through the gas diffusion layers, the catalyst layers or the membrane as well as the transient behavior of the operating temperature of the fuel cell are orders of magnitudes slower than the electrochemical processes and can therefore be neglected.

CHAPTER 6

Nonlinear control of PEMFCs

In the last chapter the coupling behavior between PEM fuel cells and DC-DC converters was addressed. This analysis showed that the design of separate control approaches for the fuel cell and the DC-DC converters are possible. Therefore, this chapter turns its focus towards the development of a control approach for the PEMFC and refers to [20, 26, 46] for the setup of suitable control strategies for DC-DC converters.

In chapter one, the necessity for the development of control approaches for PEM fuel cells was pointed out. Critical challenges in the operation of PEMFCs are the avoidance of reactant starvation, overheating, drying out and flooding of the fuel cell which can lead both to a deteriorated cell performance and to the promotion of degradation effects. Up to now, the control of PEM fuel cells is mainly based on heuristic and linear control approaches, e.g. [31, 45, 58, 64, 81]. Although these approaches show solid results they could not fully exploit the potential of the PEM fuel cells due to their complex nonlinear behavior. For this purpose, nonlinear and model-based control approaches are more promising. Unfortunately, there are only a few approaches in literature that deal with this difficult task [16, 27, 54], but the treatment of the water household there is mainly done by using simple models that typically neglect the complex and dynamic characteristics of the water household, although these effects play a vital role in the water management of PEM fuel cells, like the electro-osmotic drag of the membrane for example. Therefore, in order to enhance the results in literature, a nonlinear model-based control approach for the water management of PEMFCs is developed in this chapter that explicitly considers the dynamic impacts of the electro-osmotic drag by using an evaluated, detailed and dynamic model of the membrane. The development of the controller is done in this contribution by assuming a one-phase operation of the PEMFC like in chapter 5 and the two-phase operation is not considered in this work. This is done, because a proper controller development there demands not only a two-phase model of the PEM fuel cell but also a two-phase modeling of the reactant gas supply in the gas

bulks as experimental investigations of the liquid water build-up in low-temperature PEM fuel cells show, e.g. [6, 72, 74]. A first step in order to address this topic has already been done by the modeling of the two-phase water household in gas bulks within the scope of a student research project [60] parallel to the development of the control approach in this last chapter.

This chapter is divided in five sections. The distributed one-phase model that forms the basis of the model-based control approach has already been presented in section 2.4. Therefore, the next section directly deals with the control objectives of the proposed strategy. After that, in section 6.2, the controllability of the considered PEMFC model is analyzed. In the subsequent section 6.3, the control approach is introduced and applied, while the results of this approach are shown and explained for the case of set point control and servo control in section 6.4 and section 6.5. Finally, the results of this chapter are summarized in section 6.6.

6.1 Control objectives

The operation of PEM fuel cells can be divided in three phases: A start-up phase in order to bring the PEMFC to a system state where it can be run at high performance and efficiency. A working phase, where the fuel cell can be used to supply the varying power demand of an external load. Finally, a shut-down phase were the power supply is no longer necessary and the PEMFC can be brought down, e.g. to its initial state.

The most important phase of operation is the working phase. In this phase the fuel cell can be run with high performance and efficiency if the impact of the time varying power demand towards the humidity in the fuel cell, its operating temperature and the supply level of oxygen and hydrogen can be compensated. For this purpose, a model-based control approach towards disturbance rejection is suitable that should fulfill the following control objectives:

1. The avoidance of flooding in anode and cathode.
2. The avoidance of undersupply of the anode and cathode with hydrogen and oxygen.
3. The securing of a desired, high humidity in the membrane.

The above three points form the goals for the controller design towards disturbance rejection. These conditions should be fulfilled despite the appearance of the time-varying disturbance v. The above considerations lead to the introduction of four potential control variables[1]

$$\mathbf{y}_c := \left(a_a^{H_2O}\ \overline{a}_m^{H_2O}\ x_c^{O_2}\ a_c^{H_2O}\right)^T \tag{6.1}$$

[1]The hydrogen content in the anode can be controlled by controlling the activity of water vapor in the anode: $a_a^{H_2O}$. This is due to the closed anode and the assumed isothermic and isobaric conditions of the gas there.

that should comply the following state constraints:

$$0 \ll a_a^{H_2O},\ \overline{a}_m^{H_2O},\ a_c^{H_2O} < 1 \quad \text{and} \tag{6.2}$$

$$0 < x_c^{O_2} < x_{c,b}^{O_2}\,. \tag{6.3}$$

For the fulfillment of the control objectives the three input variables in Eqn. 2.81 are available that underlie the subsequent input constraints:

$$0 \leq a_{a,b}^{H_2O} \leq a_{a,b,max}^{H_2O} < 1\,, \tag{6.4}$$

$$0 \leq a_{c,b}^{H_2O} \leq a_{c,b,max}^{H_2O} < 1 \quad \text{and} \tag{6.5}$$

$$0 < \dot{V}_{c,b}\,. \tag{6.6}$$

in order to avoid the appearance of liquid water in the anodic and cathodic inlets and to include the fact that the direction of the volume flow rate of air could not be reversed. Note that the operating temperature of the fuel cell is not included in the control objectives above and is therefore not considered for the control design. Instead it is assumed, that a separate control loop is available to hold the temperature of the fuel cell close to its operating temperature. This assumption is not difficult to fulfill with a suitable cooling and control strategy [2, 3] due to the slow transient behavior of the temperature. The operating temperature of the cell is therefore used as a parameter in the proposed control approach. Nevertheless, the impact of a varying operating temperature upon the control design is considered by parameter variations in order to test the robustness of the proposed approach.

Besides the disturbance rejection, the developed controller should also be useful for servocontrol during the start-up and the shut-down phase of the PEMFC. For this purpose, the same control objectives, the same control variables and constraints and of course the same input variables and associated constraints as above are considered.

6.2 Controllability analysis

In section 2.4 the equations of the PEMFC model were stated. This model describes the relationship between the state, the input and the output variables. In this section a controllability analysis prior to the later control design is carried out. This is a necessary step that has to be done before the solution of every control problem in order to ensure that the state variables can be influenced in a desired way by the input variables. The controllability analysis for the given system can be carried out in two ways. Due to the fact that our system is nonlinear, we can either examine its nonlinear reachability [55] or the linear controllability [49]. The nonlinear reachability can be checked by transforming the given DAE system into an equivalent system of nonlinear ordinary differential equations. This can be done by differentiating the algebraic state equations once with respect to time, because the given DAE system is of differential index one [42]. After this, the nonlinear reachability of the equivalent ODE system can be checked. Unfortunately, a successful check in this case does only mean that reversals in time may be necessary to ensure that the

system is able to reach the desired system states [55]. This examination is therefore only of minor importance and will not be carried out in the following. Instead, the linear controllability of the system will be tested.

6.2.1 Model

The controllability analysis is performed using a linear and time-invariant (LTI) model of the PEM fuel cell. The first step towards this analysis is the linearization of the fuel cell model in Eqn. 2.76 to Eqn. 2.78. This linearization is done at stationary solutions of the PEMFC. If we use the definition of the control variables in Eqn. 6.1, we can rewrite the output relation of the PEMFC model in Eqn. 2.78 to $\mathbf{y} = (\mathbf{y}_c \mathbf{y}_{nc})^T = (\mathbf{h}_c(\mathbf{z}_D, \mathbf{z}_A)\, \mathbf{h}_{nc}(\mathbf{z}_D, \mathbf{z}_A))^T$ with controlled and uncontrolled variables $\mathbf{y}_c$ and $\mathbf{y}_{nc}$. With this, the stationary solutions of the PEMFC can be computed from

$$\mathbf{0} = \mathbf{f}_D(\mathbf{z}_D, \mathbf{z}_A, \mathbf{u})|_s \,, \tag{6.7}$$

$$\mathbf{0} = \mathbf{f}_A(\mathbf{z}_D, \mathbf{z}_A, v)|_s \,, \tag{6.8}$$

$$\mathbf{y}_c^s = \mathbf{h}_c(\mathbf{z}_D, \mathbf{z}_A)|_s \,, \tag{6.9}$$

$$\mathbf{y}_{nc}^s = \mathbf{h}_{nc}(\mathbf{z}_D, \mathbf{z}_A)|_s \,. \tag{6.10}$$

A Taylor expansion of the modeling equations up to the first derivatives and taken at the previously given steady states results then in

$$\delta\dot{\mathbf{z}}_D = \left.\frac{\partial \mathbf{f}_D}{\partial \mathbf{z}_D}\right|_s \delta\mathbf{z}_D + \left.\frac{\partial \mathbf{f}_D}{\partial \mathbf{z}_A}\right|_s \delta\mathbf{z}_A + \left.\frac{\partial \mathbf{f}_D}{\partial \mathbf{u}}\right|_s \delta\mathbf{u} \,, \tag{6.11}$$

$$\mathbf{0} = \left.\frac{\partial \mathbf{f}_A}{\partial \mathbf{z}_D}\right|_s \delta\mathbf{z}_D + \left.\frac{\partial \mathbf{f}_A}{\partial \mathbf{z}_A}\right|_s \delta\mathbf{z}_A + \left.\frac{\partial \mathbf{f}_A}{\partial v}\right|_s \delta v \,, \tag{6.12}$$

$$\delta\mathbf{y}_c = \left.\frac{\partial \mathbf{h}_c}{\partial \mathbf{z}_D}\right|_s \delta\mathbf{z}_D + \left.\frac{\partial \mathbf{h}_c}{\partial \mathbf{z}_A}\right|_s \delta\mathbf{z}_A \,, \tag{6.13}$$

$$\delta\mathbf{y}_{nc} = \left.\frac{\partial \mathbf{h}_{nc}}{\partial \mathbf{z}_D}\right|_s \delta\mathbf{z}_D + \left.\frac{\partial \mathbf{h}_{nc}}{\partial \mathbf{z}_A}\right|_s \delta\mathbf{z}_A \,. \tag{6.14}$$

If the matrix $\partial\mathbf{f}_A/\partial\mathbf{z}_A$ is invertible, which is the case in this work, then Eqn. 6.12 can be solved for $\delta\mathbf{z}_A$ and the resulting equation can be substituted in Eqn. 6.11, Eqn. 6.13 and Eqn. 6.14. If we do this, we finally get a linear and time-invariant model of the PEM fuel cell

$$\delta\dot{\mathbf{z}}_D = \mathbf{A}\delta\mathbf{z}_D + \mathbf{B}\delta\mathbf{u} + \mathbf{e}\delta v \,, \tag{6.15}$$

$$\delta y_c = \mathbf{C}_c\delta\mathbf{z}_D + \mathbf{d}_c\delta v \,, \tag{6.16}$$

$$\delta y_{nc} = \mathbf{C}_{nc}\delta\mathbf{z}_D + \mathbf{d}_{nc}\delta v \tag{6.17}$$

that is valid around the given steady state with the following abbreviations for the state equation

$$\mathbf{A} := \left.\frac{\partial \mathbf{f}_D}{\partial \mathbf{z}_D}\right|_s - \left.\frac{\partial \mathbf{f}_D}{\partial \mathbf{z}_A}\right|_s \left(\left.\frac{\partial \mathbf{f}_A}{\partial \mathbf{z}_A}\right|_s\right)^{-1} \left.\frac{\partial \mathbf{f}_A}{\partial \mathbf{z}_D}\right|_s , \tag{6.18}$$

$$\mathbf{B} := \left.\frac{\partial \mathbf{f}_D}{\partial \mathbf{u}}\right|_s , \tag{6.19}$$

$$\mathbf{e} := - \left.\frac{\partial \mathbf{f}_D}{\partial \mathbf{z}_A}\right|_s \left(\left.\frac{\partial \mathbf{f}_A}{\partial \mathbf{z}_A}\right|_s\right)^{-1} \left.\frac{\partial \mathbf{f}_A}{\partial v}\right|_s , \tag{6.20}$$

and the output equation

$$\mathbf{C}_c := \left.\frac{\partial \mathbf{h}_c}{\partial \mathbf{z}_D}\right|_s - \left.\frac{\partial \mathbf{h}_c}{\partial \mathbf{z}_A}\right|_s \left(\left.\frac{\partial \mathbf{f}_A}{\partial \mathbf{z}_A}\right|_s\right)^{-1} \left.\frac{\partial \mathbf{f}_A}{\partial \mathbf{z}_D}\right|_s , \tag{6.21}$$

$$\mathbf{C}_{nc} := \left.\frac{\partial \mathbf{h}_{nc}}{\partial \mathbf{z}_D}\right|_s - \left.\frac{\partial \mathbf{h}_{nc}}{\partial \mathbf{z}_A}\right|_s \left(\left.\frac{\partial \mathbf{f}_A}{\partial \mathbf{z}_A}\right|_s\right)^{-1} \left.\frac{\partial \mathbf{f}_A}{\partial \mathbf{z}_D}\right|_s , \tag{6.22}$$

$$\mathbf{d}_c := - \left.\frac{\partial \mathbf{h}_c}{\partial \mathbf{z}_A}\right|_s \left(\left.\frac{\partial \mathbf{f}_A}{\partial \mathbf{z}_A}\right|_s\right)^{-1} \left.\frac{\partial \mathbf{f}_A}{\partial v}\right|_s , \tag{6.23}$$

$$\mathbf{d}_{nc} := - \left.\frac{\partial \mathbf{h}_{nc}}{\partial \mathbf{z}_A}\right|_s \left(\left.\frac{\partial \mathbf{f}_A}{\partial \mathbf{z}_A}\right|_s\right)^{-1} \left.\frac{\partial \mathbf{f}_A}{\partial v}\right|_s . \tag{6.24}$$

This model is used to analyze the controllability of the PEMFC. The criteria for this analysis are introduced in the next section.

6.2.2 Controllability

The controllability of the PEMFC model is examined in two steps. In the first step, a qualitative statement about the controllability is given using a criterion that is valid for LTI-systems. In a second step, the controllability is analyzed quantitatively using step changes of the input variables.

The controllability of LTI-systems, like the given one in Eqn. 6.15-6.20, is defined in the following manner [49]: An LTI-system is called completely controllable with respect to its input variables $\delta\mathbf{u}$ if it is possible to transfer the system from every arbitrary initial state within finite time to a prespecified final state by choosing appropriate trajectories for the input variables. This property can be easily tested for an LTI-system with the Kalman criterion [49]: An LTI-system with dynamic matrix $\mathbf{A}$ (Eqn. 6.18) and input matrix $\mathbf{B}$ (Eqn. 6.19) is completely controllable if and only if the controllability matrix

$$\mathbf{S} := \left(\mathbf{B}\ \mathbf{AB}\ \mathbf{A}^2\mathbf{B}\ \ldots\ \mathbf{A}^{N+5-1}\mathbf{B}\right) \tag{6.25}$$

has full rank: $rank(\mathbf{S}) = N + 5$. This check can be done very fast but supplies one only with a qualitative statement about the controllability of an LTI-system.

The design of a multivariable control system requires not only a qualitative but also a quantitative statement about the controllability. This is useful in order to determine the structure of the control design, i.e. if a multivariable controller is necessary to control the system or if it can be substituted by several decentralized controllers [50]. The criterion for this decision is a negligible mutual influence of the decentralized controllers upon each other. There are several empirical methods in literature that can be used to get a quantitative statement about the controllability of an LTI-system [50]. In this work step responses of the output variables due to step changes of the input variables are used for this purpose.

6.2.3 Results

In this section the results of the controllability analysis are shown. This analysis is done with the Kalman criterion and with step changes using the linearized PEMFC-model in Eqn. 6.15 to Eqn. 6.20. The controllability is tested at several different but typical operating points of the fuel cell. For this purpose, the fuel cell is well humidified and operated with constant input variables. The input variables are selected such that a high relative humidity in the cell is obtained but no flooding appears at high current densities. In Fig. 6.1 the underlying stationary profiles of the PEMFC for this analysis are shown. They are calculated from Eqn. 6.7 to Eqn. 6.10. In Fig. 6.1a the voltage-current and the power-current characteristic curves with marked steady states that are used for the controllability analysis are depicted. The corresponding activities of water vapor in the anode, the cathode and the membrane are displayed in Fig. 6.1b, while the content of oxygen and hydrogen is given in Fig. 6.1c. Finally, the used input variables are displayed in Fig. 6.1d. In a first step, the Kalman criterion is used. At each of the working points a linearized model is computed and the linear controllability criterion of Kalman from Eqn. 6.25 is examined. It turns out that the controllability matrix has full rank at each of the considered working points and therefore the PEMFC model is completely controllable there. Due to the dense grid of considered operating points it is therefore also probable that the PEMFC is in general completely controllable at every operating point for the given inputs.

The previous qualitative analysis is followed by a quantitative investigation of the fuel cell's controllability. This is done with step responses. At each of the marked steady states in Fig. 6.1a, a linearized model is computed and step changes are applied to each of the three input variables: $\delta\mathbf{u} = (\delta a_{a,b}^{H_2O}\ \delta\dot{V}_{c,b}\ \delta a_{c,b}^{H_2O})^T$. This is done consecutively with the following three input vectors arranged here in matrix notation: $(\delta\mathbf{u}_1(t)\ \delta\mathbf{u}_2(t)\ \delta\mathbf{u}_3(t)) := diag(\delta u_i)h(t)$. The step heights are denoted with δu_i and the quantity $h(t)$ describes the Heaviside step function. The step heights δu_i are defined so that the validity of the linearized PEMFC model is not left, i.e. the operation of the model close to its steady state and with a one-phase water household is still valid. For this purpose we choose a relative change in every input variable of 10 percent with respect to the stationary value. Therefore we get: $\delta u_1 := -0.1 a_{a,b,s}^{H_2O}$, $\delta u_2 := 0.1\dot{V}_{c,b,s}$ and $\delta u_3 := -0.1 a_{c,b,s}^{H_2O}$ in order to get comparable simulation results

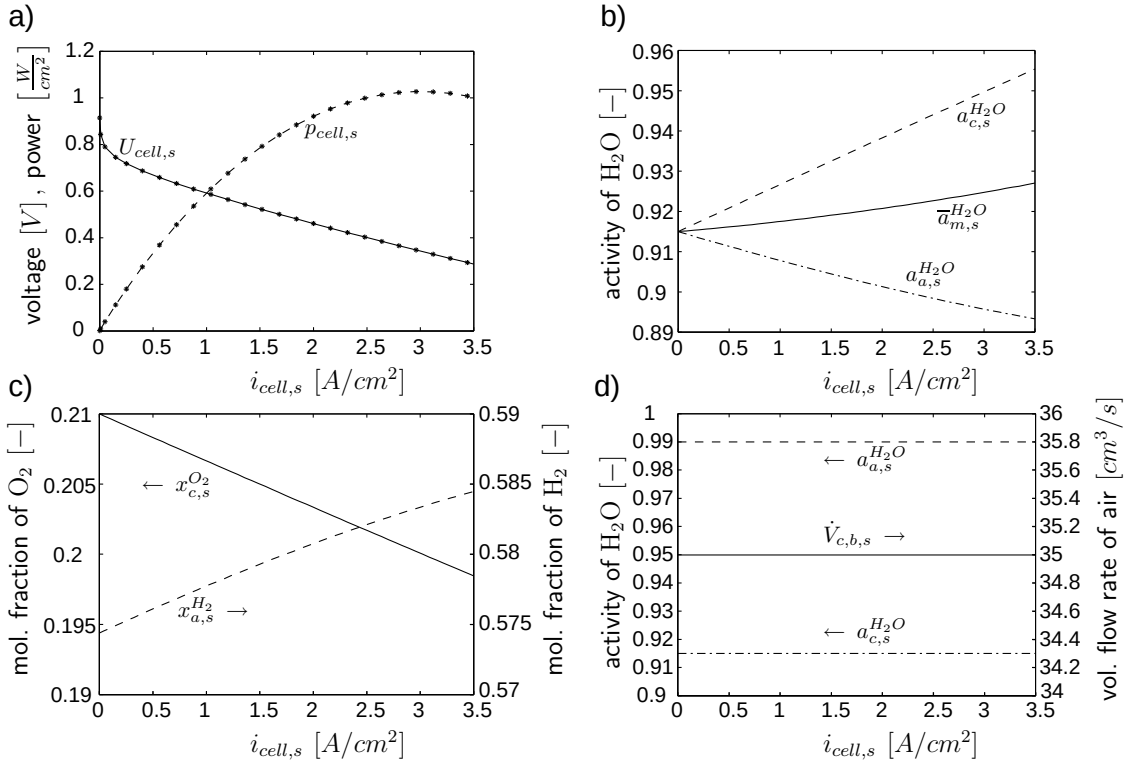

Figure 6.1: Steady state profiles of the PEM fuel cell used for the controllability analysis.

for the control variables.

The step responses of the linearized models are displayed in Fig. 6.2. Shown are the linearized control variables $\delta\mathbf{y}_c = (\delta a_a^{H_2O}\, \delta\overline{a}_m^{H_2O}\, \delta x_c^{O_2}\, \delta a_c^{H_2O})^T$ with respect to the input variables. The figure is arranged as a 4×3 matrix $(\delta\mathbf{y}_{c,1}(t)\, \delta\mathbf{y}_{c,2}(t)\, \delta\mathbf{y}_{c,3}(t))$, where the columns represent the step responses of the linearized control variables with respect to the three input variables. The diagram in Fig. 6.2 can now be used

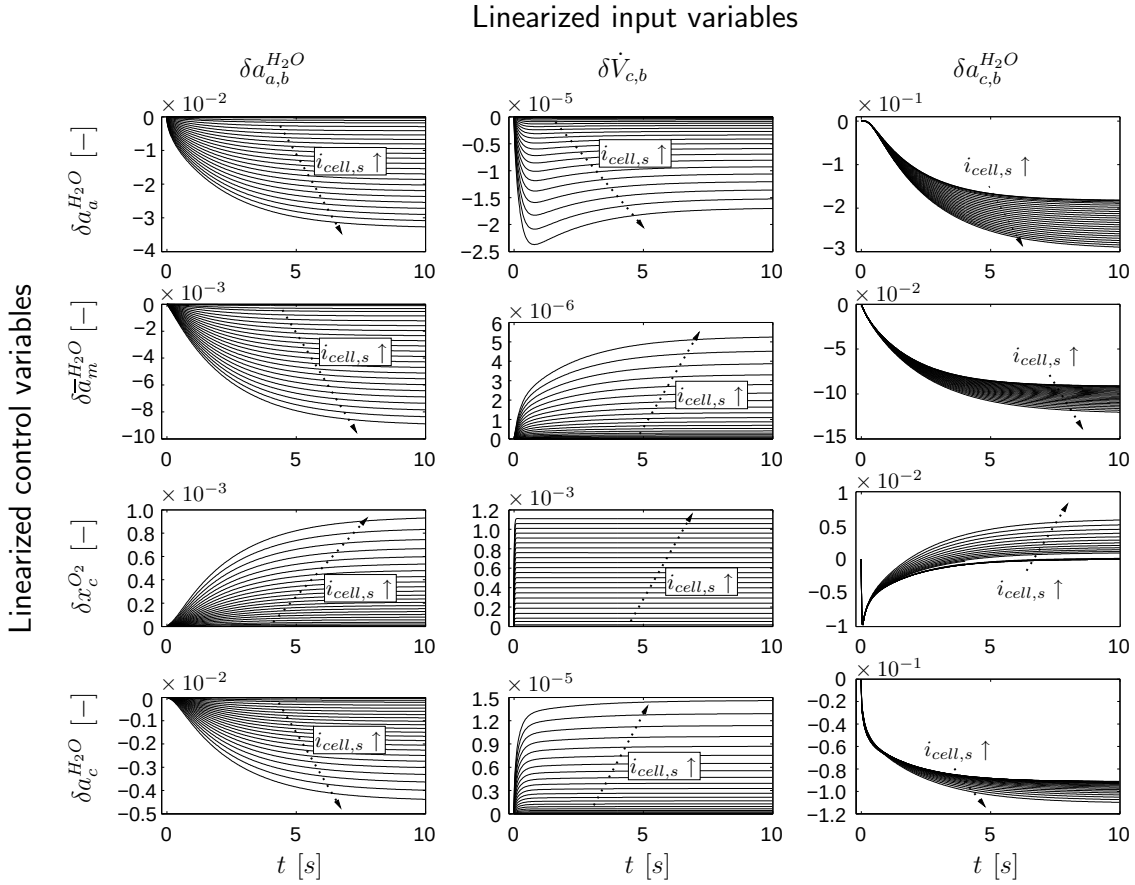

Figure 6.2: Step responses of the linearized fuel cell model at different steady states.

to determine the structure for the control design. The first question that has to be clarified is if a multivariable control approach is necessary or if it can be replaced by decentralized controllers. A suitable way to control the oxygen content in the PEMFC is by using the volume flow rate. This is because of the following two reasons that can be found from the third row in Fig. 6.2:

- The transient behavior of the oxygen content $\delta x_c^{O_2}$ is much faster with respect to the volume flow rate $\delta\dot{V}_{c,b}$ than with respect to the anodic and cathodic activities in the inlet $\delta a_{a,b}^{H_2O}$ and $\delta a_{c,b}^{H_2O}$ respectively.

- The stationary changes of $\delta x_c^{O_2}$ due to the steps in the input variables are in the same order of magnitude for all three input variables.

Therefore, if we choose the volume flow rate to control the oxygen content, we can expect to get quick control actions in order to fulfill the state constraint in Eqn. 6.3. For the control of the humidity in the fuel cell, the activities in the anodic and cathodic inlets namely $\delta a_{a,b}^{H_2O}$ and $\delta a_{c,b}^{H_2O}$ seem most suitable. This can be underlined by the following two reasons and can be seen from the first, second and the fourth row of Fig. 6.2:

- Both input variables are influencing the humidity in the fuel cell in the same direction: A decrease in the inlet humidities $\delta a_{a,b}^{H_2O}$ and $\delta a_{c,b}^{H_2O}$ leads to a decrease in the anodic, cathodic and the membrane humidity, namely in the linearized control variables $\delta a_{a,b}^{H_2O}$, $\delta \overline{a}_m^{H_2O}$ and $\delta a_c^{H_2O}$. This result is not surprising due to the water transport in the membrane and holds analogously for an increase in the inlet humidities too.

- The effect of the third input variable, the volume flow rate $\delta \dot{V}_{c,b}$ upon the humidity is orders of magnitudes smaller than the impact of the inlet activities $\delta a_{a,b}^{H_2O}$ and $\delta a_{c,b}^{H_2O}$.

Therefore, the multivariable control approach can be substituted with two decentralized controllers, one for the control of the oxygen content in the cathode and one for the control of the humidity in the entire fuel cell.

The second question that has to be answered is how the humidity in the fuel cell will be controlled in detail. An obvious approach is chosen for this: The anodic humidity is controlled with the anodic inlet activity and the cathodic humidity with the cathodic inlet activity. This is done for the following reasons:

- The control of the humidities in the electrodes will indirectly control the humidity in the membrane due to its strong dependency at the anodic and cathodic water content. This approach is chosen for two reasons. The first reason is disturbance rejection. Possible disturbance, such as changes of the ohmic load resistance or the cell temperature for example, lead to to a varying membrane humidity in an uncontrolled PEMFC and therefore to a varying power output of the fuel cell. The control of the gas bulks is aimed at the rejection of those disturbances by holding the humidities in the bulks and GDLs at their specified values. This leads to specified boundary conditions of the membrane and therefore to the avoidance of unwanted changes of its humidity. The other reason why the humidities in the gas bulks are controlled, and not directly the membrane humidity, is due to the electro-osmotic drag of the membrane and the limitations of the used passivity-based control approach. A direct passivity-based control approach may be able to hold the membrane humidity at its specified value but cannot concurrently prevent the accumulation of water vapor and the possible threat of flooding at the cathode side due to the electro-osmotic drag. This is due to the fact that the state constraint Eqn. 6.2 cannot be included in the passivity-based control approach.

- Disturbances in the gas pressure and the temperature have a large impact upon the water household in the electrodes. In order to avoid flooding there and to suffice the state constraint in Eqn. 6.2 the anodic and the cathodic humidities are controlled.

In summary, the following three assignments between input and control variables are used for the following control design: (i) The volume flow rate $\dot{V}_{c,b}$ is used to control the oxygen content $x_c^{O_2}$, (ii) the anodic inlet activity $a_{a,b}^{H_2O}$ controls the anodic humidity $a_a^{H_2O}$, and (iii) the cathodic inlet activity $a_{c,b}^{H_2O}$ is assigned to the humidity in the cathode $a_c^{H_2O}$.

6.3 Control approach

In this section a passivity-based control approach is proposed for the PEM fuel. In a first step, the principle of this control approach is introduced. After that, the approach is applied to the PEMFC and the obtained control results are presented and discussed.

6.3.1 Principle

The passivity-based control approach [38] is a useful tool for developing feedback control strategies for nonlinear systems of the form:

$$\dot{\mathbf{x}}_p = \mathbf{f}_p(\mathbf{x}_p, \mathbf{u}_p), \tag{6.26}$$

$$\mathbf{y}_p = \mathbf{h}_p(\mathbf{x}_p) \tag{6.27}$$

with state variables $\mathbf{x}_p \in \mathbb{D}_{xp} \subset \mathbb{R}^{n_{xp}}$, input variables $\mathbf{u}_p \in \mathbb{D}_{up} \subset \mathbb{R}^{n_{up}}$ and output variables $\mathbf{y}_p \in \mathbb{D}_{yp} \subset \mathbb{R}^{n_{yp}}$. For the solution of the above system the common assumptions about existence and uniqueness of ODEs shall be valid [38]. It is assumed that ($\mathbf{x}_p = \mathbf{0}$, $\mathbf{u}_p = \mathbf{0}$) is an equilibrium point of the above system with $\mathbf{0} = \mathbf{f}_p(\mathbf{0}, \mathbf{0})$ and $\mathbf{0} = \mathbf{h}_p(\mathbf{0})$. The system in Eqn. 6.26 and Eqn. 6.27 is called *passive* if there exists a differentiable positive semidefinite function[2] $\mathcal{V}(\mathbf{x}_p)$, called the storage function, such that

$$\mathbf{u}_p^T \mathbf{y}_p \geq \dot{\mathcal{V}} = \frac{\partial \mathcal{V}}{\partial \mathbf{x}_p} \mathbf{f}_p(\mathbf{x}_p, \mathbf{u}_p) \tag{6.28}$$

for all ($\mathbf{x}_p$, $\mathbf{u}_p$). It is called *zero-state observable* if no solution of $\dot{\mathbf{x}}_p = \mathbf{f}_p(\mathbf{x}_p, \mathbf{0})$ can stay identically in the set $\{\mathbf{x}_p \mid \mathbf{h}_p(\mathbf{x}_p) = \mathbf{0}\}$ other than the trivial solution $\mathbf{x}_p \equiv \mathbf{0}$. With these two definitions the basic idea of passivity-based control can be presented with the following theorem.

Theorem. *If the nonlinear system in Eqns. (6.26, 6.27) is*

[2] A function $\mathcal{V}(\mathbf{x}_p)$ satisfying $\mathcal{V}(\mathbf{0}) = 0$ and $\mathcal{V}(\mathbf{x}_p) > 0$ for $\mathbf{x}_p \neq \mathbf{0}$ is said to be positive definite. If it satisfies the weaker condition $\mathcal{V}(\mathbf{x}_p) \geq 0$ for $\mathbf{x}_p \neq \mathbf{0}$, it is said to be positive semidefinite.

(1) passive with a positive definite storage function and

(2) zero-state observable,

then the origin $\mathbf{x}_p = \mathbf{0}$ *can be stabilized by* $\mathbf{u}_p = -\boldsymbol{\phi}(\mathbf{y}_p)$*, where* $\boldsymbol{\phi}$ *is any locally Lipschitz function*[3] *such that* $\boldsymbol{\phi}(\mathbf{0}) = \mathbf{0}$ *and* $\mathbf{y}_p^T \boldsymbol{\phi}(\mathbf{y}_p) > 0$ *for all* $\mathbf{y}_p \neq \mathbf{0}$*.*

A proof for this theorem is given in [38]. In order to use the above theorem the considered system needs to be passive and zero-state observable. This can be achieved by transforming nonpassive systems into passive ones. This idea will be illustrated in the following. Given is a nonlinear system of the form:

$$\dot{\mathbf{x}}_{np} = \mathbf{f}_{np}(\mathbf{x}_{np}, \mathbf{d}_{np}) + \mathbf{g}_{np}(\mathbf{x}_{np}, \mathbf{u}_{np}, \mathbf{d}_{np}) \tag{6.29}$$

with state variables $\mathbf{x}_{np} \in \mathbb{D}_{xnp} \subset \mathbb{R}^{n_{xnp}}$, input variables $\mathbf{u}_{np} \in \mathbb{D}_{unp} \subset \mathbb{R}^{n_{unp}}$ and disturbances $\mathbf{d}_{np} \in \mathbb{R}^{n_{dnp}}$ that needs to be suppressed. The control variables are identical with the state variables and the desired state variables should be given by $\mathbf{x}_{np}^* \in \mathbb{R}^{n_{xnp}}$. In a first step, we choose the positive definite storage function

$$\mathcal{V} := \frac{1}{2} \left(\mathbf{x}_{np} - \mathbf{x}_{np}^*\right)^T diag(\mathcal{K}_i^{-1}) \left(\mathbf{x}_{np} - \mathbf{x}_{np}^*\right) \tag{6.30}$$

with $\mathcal{K}_i > 0, i = 1...n_{xnp}$. If we calculate the time derivative of $\mathcal{V}$ and insert Eqn. 6.29 in it we get

$$\dot{\mathcal{V}} = \underbrace{\left(\mathbf{x}_{np} - \mathbf{x}_{np}^*\right)^T}_{\mathbf{y}_p^T :=} \underbrace{diag(\mathcal{K}_i^{-1}) \left(\mathbf{f}_{np}(\mathbf{x}_{np}) + \mathbf{g}_{np}(\mathbf{x}_{np}, \mathbf{u}_{np}, \mathbf{d}_{np}) - \dot{\mathbf{x}}_{np}^*\right)}_{\mathbf{u}_p :=} . \tag{6.31}$$

The definition of $\mathbf{u}_p$ can be solved for $\mathbf{g}_{np}$ and one obtains

$$\mathbf{g}_{np}(\mathbf{x}_{np}, \mathbf{u}_{np}, \mathbf{d}_{np}) = diag(\mathcal{K}_i)\mathbf{u}_p + \dot{\mathbf{x}}_p^* - \mathbf{f}_{np}(\mathbf{x}_{np}, \mathbf{d}_{np}) . \tag{6.32}$$

If we use this result in the state Eqn. 6.29 and the definition of $\mathbf{y}_p$ from Eqn. 6.31 together with the definition

$$\mathbf{e}_p := \mathbf{x}_{np} - \mathbf{x}_{np}^* \tag{6.33}$$

that denotes the difference between the state and the desired state variables the following transformed system can be obtained:

$$\dot{\mathbf{e}}_p = diag(\mathcal{K}_i)\, \mathbf{u}_p , \tag{6.34}$$

$$\mathbf{y}_p = \mathbf{e}_p . \tag{6.35}$$

Note that ($\mathbf{e}_p = \mathbf{0}$, $\mathbf{u}_p = \mathbf{0}$) is an equilibrium point of this system and that it is both passive and zero-state observable because of Eqn. 6.31 and because of $\{\mathbf{e}_p \mid \mathbf{y}_p =$

[3] A function $\boldsymbol{\phi}(\mathbf{y}_p)$ is called locally Lipschitz on an open and connected domain $\mathbb{D}_{yp} \subset \mathbb{R}^{n_{yp}}$ if each point of $\mathbb{D}_{yp}$ has a neighborhood $\mathbb{D}_0$ such that $\boldsymbol{\phi}$ satisfies the Lipschitz condition $||\boldsymbol{\phi}(\mathbf{y}_{p,1}) - \boldsymbol{\phi}(\mathbf{y}_{p,2})|| \leq L||\mathbf{y}_{p,1} - \mathbf{y}_{p,2}||$ for all points in $\mathbb{D}_0$ with some Lipschitz constant L_0. A sufficient condition for this is the continuity of $\boldsymbol{\phi}(\mathbf{y}_p)$ and $\partial\boldsymbol{\phi}/\partial\mathbf{y}_p$ on $\mathbb{D}_{yp}$ [38].

$\mathbf{0}\} = \{\mathbf{0}\}$. Therefore, we can use the above theorem to find a stabilizing input $\mathbf{u}_p = -\boldsymbol{\phi}(\mathbf{y}_p)$ for this system. An obvious choice for this is

$$\boldsymbol{\phi}(\mathbf{y}_p) = \mathbf{y}_p \tag{6.36}$$

which is a local Lipschitz function and fulfills both $\boldsymbol{\phi}(\mathbf{0}) = \mathbf{0}$ and $\mathbf{y}_p^T \boldsymbol{\phi}(\mathbf{y}_p) = \mathbf{y}_p^T \mathbf{y}_p > 0$ for all $\mathbf{y}_p \neq \mathbf{0}$. If we use this choice in the passive system in Eqn. 6.34 and Eqn. 6.35) we obtain a system of first order ODEs $\dot{\mathbf{e}}_p + diag(\mathcal{K}_i)\mathbf{e}_p = \mathbf{0}$ that leads to an exponential decrease in the control error $\mathbf{e}_p$ and stabilizes the system in Eqn. 6.29. The positive parameters $\mathcal{K}_i$ can be used to tune the convergence rate of the error. Note that the control law for the input variables is computed by solving Eqn. 6.32 after $\mathbf{u}_{np}$, and that the validity of the stated passivity-based control approach requires this solutions to be inside the domain $\mathbb{D}_{unp}$. Passivity-based control is applied in the following to control the PEM fuel cell.

6.3.2 Application to the PEMFC

During the controllability analysis in section 6.2 we have seen that a suitable way to fulfill the control objectives is to control the humidity in the fuel cell and the oxygen content. This can be achieved by controlling the gas compositions in the anode and in the cathode. Therefore, the proposed passivity based control approach is applied at the anode and at the cathode side. First of all, the control of the cathode is shown.

Control law for the cathode. The compositions in the cathode are described by the balance equations for oxygen and water vapor in Eqn. 2.66 and Eqn. 2.67. Both equations together form a system given in Eqn. 6.29 with states $\mathbf{x}_{np} := (x_c^{O_2}\, a_c^{H_2O})^T$, input variables $\mathbf{u}_{np} := (\dot{V}_{c,b}\, a_{c,b}^{H_2O})^T$ and disturbances like the current density i_T and the flux $N_c^{H_2O}$. Moreover, the domains $\mathbb{D}_{xnp}$ and $\mathbb{D}_{unp}$ of the state and the input variables are given by the constraints in Eqn. 6.2 and Eqn. 6.3, and Eqn. 6.5 and Eqn. 6.6.

In the cathode we want to control the activity of water vapor and the oxygen content. Their desired values should be denoted with $\mathbf{x}_{np}^* := (x_{c,*}^{O_2}\, a_{c,*}^{H_2O})^T$. If we apply the reasoning in the last section to introduce a stabilizing input $\mathbf{u}_p = -\boldsymbol{\phi}$ we get

$$\mathbf{y}_p = -\left(\begin{pmatrix} x_c^{O_2} \\ a_c^{H_2O} \end{pmatrix} - \begin{pmatrix} x_{c,*}^{O_2} \\ a_{c,*}^{H_2O} \end{pmatrix} \right) \tag{6.37}$$

according to Eqn. 6.36, Eqn. 6.35 and Eqn. 6.33. If we insert this choice in Eqn. 6.32 and solve for $\mathbf{u}_{np}$ we come up with the following control laws for the input variables:

$$\dot{V}_{c,b} = \frac{V_c}{x_{c,b}^{O_2} - x_c^{O_2}} \left[\frac{A}{\chi_c^{tot} V_c} \left(\left(1 + x_c^{O_2}\right) \frac{i_T}{2\zeta_c F} - x_c^{O_2} N_c^{H_2O} \right) + \dot{x}_{c,*}^{O_2} - \mathcal{K}_c^{O_2} \left(x_c^{O_2} - x_{c,*}^{O_2} \right) \right] \tag{6.38}$$

where $x_{c,b}^{O_2} - x_c^{O_2} \neq 0$ is assumed, and

$$a_{c,b}^{H_2O} = a_c^{H_2O} + \frac{V_c}{\dot{V}_{c,b}} \left[\frac{A}{\chi_c^{tot} V_c} \left(\left(\frac{p_c^g}{p_{sat}} - a_c^{H_2O} \right) N_c^{H_2O} - \left(2\frac{p_c^g}{p_{sat}} - a_c^{H_2O} \right) \frac{i_T}{2\zeta_c F} \right) + \dot{a}_{c,*}^{H_2O} - \mathcal{K}_c^{H_2O} \left(a_c^{H_2O} - a_{c,*}^{H_2O} \right) \right]. \tag{6.39}$$

In the above equations the volume flow rate $\dot{V}_{c,b}$ is used to control the oxygen content $x_c^{O_2}$ and the activity in the cathodic inlet $a_{c,b}^{H_2O}$ controls the activity in the cathode $a_c^{H_2O}$. This is done according to the results of the controllability analysis. The positive parameters $\mathcal{K}_c^{O_2}$ and $\mathcal{K}_c^{H_2O}$ in the control laws can be used to tune the control approach.

With the above control laws the composition in the cathode can be controlled and stabilized towards the desired values $x_{c,*}^{O_2}$ and $a_{c,*}^{H_2O}$. This is true as long as the calculated input variables in Eqn. 6.38 and Eqn. 6.39 stay in their corresponding domain $\mathbb{D}_{unp}$ given by the input constraints in Eqn. 6.5 and Eqn. 6.6. Unfortunately, the passivity-based control approach does not include input constraints in its design. Therefore, simulation studies have to be carried out to ensure the validity of these constraints for the input variables.

Control law for the anode. In this section the control approach for the anode side is shown. At the anode, the humidity will be controlled. It is given by the activity of water vapor there and described by Eqn. 2.68. If we compare this equation with the system given by Eqn. 6.29 like at the cathode side, we can identify the system's state $x_{np} = a_a^{H_2O}$, its input variable $u_{np} = a_{a,b}^{H_2O}$ and the present disturbances i_{cell} and $N_a^{H_2O}$. Finally, the domains $\mathbb{D}_{xnp}$ and $\mathbb{D}_{unp}$ of the state and input variable are given by the constraints in Eqn. 6.2 and Eqn. 6.4.

If we denote the desired activity in the anode with $x_{np}^* := a_{a,*}^{H_2O}$ and apply the passivity-based control approach like at the cathode side we can find a stabilizing input $u_p = -\phi$ that is given by

$$y_p = -\left(a_a^{H_2O} - a_{a,*}^{H_2O} \right) \tag{6.40}$$

from Eqn. 6.36, Eqn. 6.35 and Eqn. 6.33. If this choice is inserted in Eqn. 6.32 and solved for u_{np} we get a passivity-based control law at the anode side:

$$u_{np} = \frac{\chi_a^{tot} V_a}{A \left(N_a^{H_2O} + \frac{i_{cell}}{\zeta_c F} \right)} \left[\frac{A}{\chi_a^{tot} V_a} \frac{p_a^g}{p_{sat}} N_a^{H_2O} + \dot{a}_{a,*}^{H_2O} - \mathcal{K}_a^{H_2O} \left(a_a^{H_2O} - a_{a,*}^{H_2O} \right) \right] \tag{6.41}$$

where $N_a^{H_2O} + i_{cell}/\zeta_c F \neq 0$ is assumed. This is in general the case in a fuel cell with a closed anode due to the electro-osmotic drag. The positive parameter $\mathcal{K}_a^{H_2O}$ is used to tune the controller. The above control law is valid as long as the calculated value for u_{np} lies inside its domain $\mathbb{D}_{unp}$. Unfortunately, this is not the case here in general as will be explained in the following.

In PEM fuel cells the transport of protons from the anode to the cathode side and through the membrane causes the electro-osmotic drag of water molecules. This effect is contained in the used PEMFC model and causes together with the commonly used closed anode a dehydration of the anode despite the fact that the activity in the anodic inlet is at its maximum. This is shown for the uncontrolled PEMFC in Fig. 6.1. In Fig. 6.1d the activity in the anodic inlet is set to its maximum $a_{a,b,s}^{H_2O} = a_{a,b,max}^{H_2O} = 0.99$. Despite this, the activity in the anode $a_{a,s}^{H_2O}$ decreases due to the electro-osmotic drag in the cell as can be seen from Fig. 6.1b. Therefore, it is not possible to avoid dehydration in a closed anode by using the anodic inlet activity. This cannot be prevented either by increasing the activity at the cathode $a_{c,s}^{H_2O}$ by stepping up the inlet activity $a_{c,b,s}^{H_2O}$ there. This would only shift the characteristic curves in Fig. 6.1b to higher values, but would not avoid a dehydration of the anode. Indeed, the electro-osmotic drag and therefore the dehydration of the anode would be larger in this case due to the increased humidity and proton conductivity of the membrane. Therefore, the passivity based control law in Eqn. 6.42 cannot be used to avoid a dehydration of the anode by simultaneously staying with the input variable u_{np} inside its domain $\mathbb{D}$.

Nevertheless, the reverse case, i.e. the hindrance of flooding in the anode can still be accomplished by the above control law. In order to include this, the following control law for the anode is proposed:

$$a_{a,b}^{H_2O} = \begin{cases} a_{a,b,max}^{H_2O} & \text{for} \quad a_a^{H_2O} - a_{a,*}^{H_2O} \leq 0\,, \\ \min\left(u_{np}(\mathcal{K}_a^{H_2O} = 0), a_{a,b,max}^{H_2O}\right) & \text{for} \quad 0 < a_a^{H_2O} - a_{a,*}^{H_2O} \leq e_+\,, \\ 0 & \text{for} \quad a_a^{H_2O} - a_{a,*}^{H_2O} > e_+\,. \end{cases} \tag{6.42}$$

It is separated into three parts determined by the error between actual and desired anode activity and the thresholds $e_+ > 0$ and 0. In the first part of the control law in Eqn. 6.42, i.e. for $a_a^{H_2O} - a_{a,*}^{H_2O} \leq 0$ the maximum value for the input variable $a_{a,b}^{H_2O}$ is chosen. In this case no further control action at the anode side is possible due to the previously stated considerations. The second part of the control law in Eqn. 6.42, i.e. for $0 < a_a^{H_2O} - a_{a,*}^{H_2O} \leq e_+$ is introduced to avoid a switching behavior between the first and the third part of the control law. It can be seen as a feedforward control action that is obtained by setting the tuning parameter $\mathcal{K}_a^{H_2O}$ in Eqn. 6.41 to zero. This is valid as long the calculated value is smaller than the maximum value $a_{a,b,max}^{H_2O}$ of the input variable, otherwise this value is chosen as in the first part of the control law. The third part of the control law, i.e. for $a_a^{H_2O} - a_{a,*}^{H_2O} > e_+$ can be obtained form the passivity based control law in Eqn. 6.41 by selecting

$$\mathcal{K}_a^{H_2O} = \frac{\frac{A}{\chi_a^{tot} V_a} \frac{p_a^g}{p_{sat}} N_a^{H_2O} + \dot{a}_{a,*}^{H_2O}}{a_a^{H_2O} - a_{a,*}^{H_2O}} \tag{6.43}$$

for the tuning parameter $\mathcal{K}_a^{H_2O}$. This is done to include the lower bound of the input constraint (see Eqn. 6.4) of the input variable $a_{a,b}^{H_2O}$ in the control law. The above substitution is valid as long as $\mathcal{K}_a^{H_2O}$ stays positive. The denominator is positive due to the considered positive error. The numerator must also be positive. If set point

control is considered, i.e. $\dot{a}_{a,*}^{H_2O} = 0$ than $N_a^{H_2O}$ must be positive. This assumption is in general valid in a fuel cell operating with a closed anode, where the water of the humidified hydrogen stream can only leave the anode through the membrane. If servo control is considered, then the desired trajectory $a_{a,*}^{H_2O}$ must be chosen, so that the numerator of Eqn. 6.43 including $\dot{a}_{a,*}^{H_2O}$ stays positive.

In summary, the proposed control approach is simply structured and its behavior can be easily reproduced as will be underlined in the following section. The implementation of the control laws requires the measurement and/or the estimation of state variables of the fuel cell, like the activity of water and the oxygen content. For the estimation an observer like the extended Luenberger observer or the extended Kalman filter can be designed for example. In the next two sections the results of the control study are shown. This is done for set point control and servo control using stationary and dynamic simulations.

6.4 Set point control

In this section the control approach is used for set point control, where the main aim is disturbance rejection with respect to the load resistance r_{cell} connected to the fuel cell. The impact of the control approach upon the PEMFC is shown in stationary and in dynamic simulation results in the following.

6.4.1 Stationary simulation results

First of all, the stationary profiles of the controlled and the uncontrolled PEM fuel cell are compared. In Fig. 6.3 the most important steady state profiles of the controlled PEM fuel cell are displayed. They can be computed by inserting the control laws for the anode and the cathode in Eqn. 6.38, Eqn. 6.39 and Eqn. 6.42 in the fuel cell model given by Eqn. 2.76 to Eqn. 2.78 and considering only the stationary case using $x_c^{O_2} = x_{c,*}^{O_2} = 0.2$, $a_a^{H_2O} = a_c^{H_2O} = a_{c,*}^{H_2O} = 0.95$ and a varying load resistance r_{cell}. In Fig. 6.3a the cell voltage and the cell power are depicted with respect to the cell current. They are similar to the profiles of the uncontrolled PEMFC in Fig. 6.1a. In Fig. 6.3b the activity of water vapor in the cathode, the anode and the average activity in the membrane are displayed. These profiles are clearly different from the characteristic curves of the uncontrolled fuel cell in Fig. 6.3b. The main difference is that the activities in the fuel cell are upper bounded with the applied control approach. At the anode side, the electro-osmotic drag leads still to a dehumidification. This is due to the closed anode and cannot be avoided by the control approach as we outlined above. In Fig. 6.3c the oxygen and hydrogen content in the controlled fuel cell are shown. A comparison with the characteristic curves of the uncontrolled PEMFC in Fig. 6.1c shows that the oxygen content is held constant in the controlled PEMFC, while the hydrogen content still varies due to the variation of the activity at the anode side. Finally, in Fig. 6.3, the stationary profiles of the input variables of the controlled PEMFC are depicted. If we compare these profiles with the input variables of the uncontrolled case in Fig. 6.1d we can

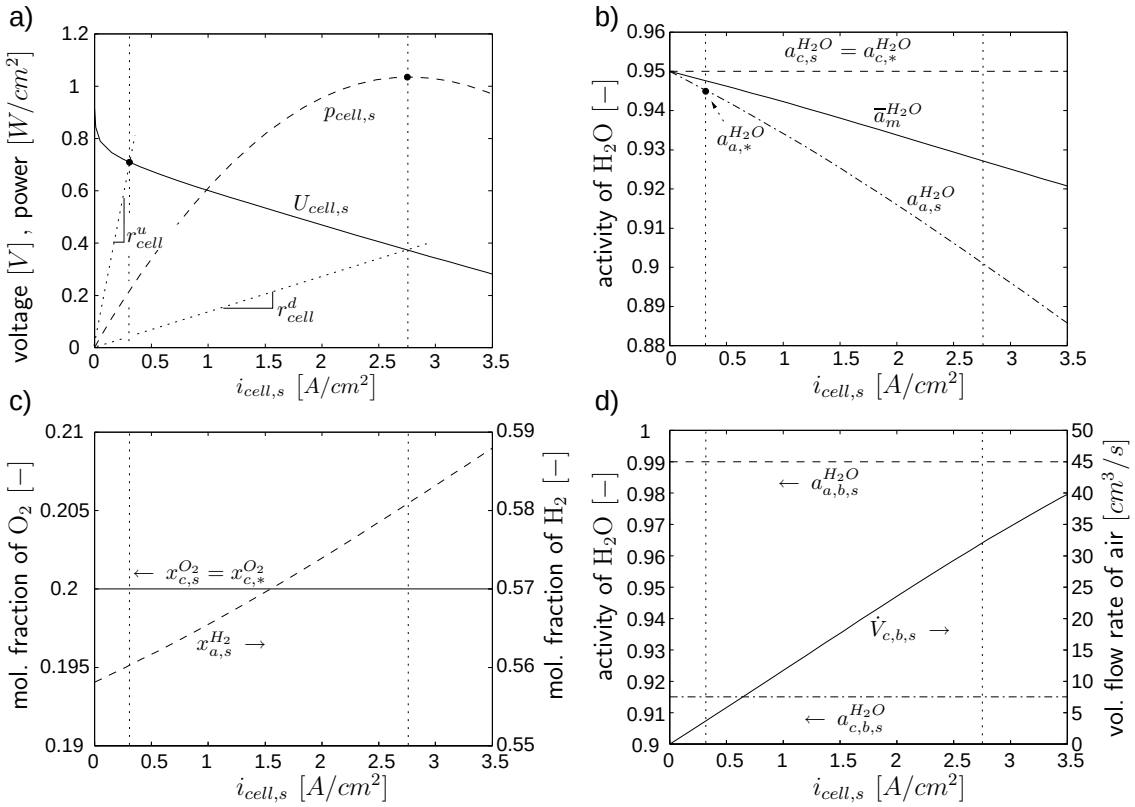

Figure 6.3: Stationary profiles of the controlled PEM fuel cell.

recognize two things: The activities in the anodic and cathodic inlet are equal in both cases, while the volume flow rate of air changes in the controlled case according to the demanded cell current and cell power.

6.4.2 Dynamic simulation results

In the following the results for set point control are presented. The choice of this set point is a compromise between a high stationary humidity in the fuel cell with small overvoltage losses and the usage of not too large control actions during the dynamic behavior of the PEMFC. In this contribution the desired set point in terms of the oxygen content, the hydrogen content and the humidity in the fuel cell is chosen to be $a_{c,*}^{H_2O} = 0.95$, $a_{a,*}^{H_2O} = 0.945$ and $x_{c,*}^{O_2} = 0.2$ and is displayed in Fig. 6.3b and Fig. 6.3c.

The aim of set point control is in general disturbance rejection. In this case, the disturbance is given by the varying load resistance r_{cell} and models the power drawn from the fuel cell. For this purpose, the load resistance is varied in the interval $r_{cell} \in \left[r_{cell}^d \; r_{cell}^u\right]$, where the boundaries r_{cell}^d and r_{cell}^u are displayed in Fig. 6.3a. They are determined by the beginning of the fuel cell's ohmic region, in order to use the self-humidification of the PEMFC for its operation, and the maximum cell power. The actual development of the load resistance with respect to time is shown in Fig. 6.4a. The signal is made up from steep drops in the load resistance modeling sharp increases in power demand and softer rises in r_{cell} meaning moderate decreases in the demanded power as one might expect the power request of a connected consumer. This signal is used for test purposes in the following simulation.

In addition to this, the robustness of the control approach with respect to different cell temperatures is also considered. This is done, because temperature changes have a large impact upon the water household in the fuel cell and can lead to flooding or drying out. In order to test the control approach, the temperature changes depicted in Fig. 6.4b are used. Three cases are discriminated. In the first case, the cell temperature is at its nominal value, while in the other cases a higher and a lower cell temperature is taken. The maximum changes of the temperature by $\pm 4K$ are chosen so that they are approximately equal to the appearing deviations in simple linear temperature control approaches for PEMFCs, e.g. [3].

In Fig. 6.5 the result of the set point control for the activity of water vapor in the fuel cell are shown. We can see that the activity $a_c^{H_2O}$ at the cathode side is hold at its reference value for all three considered temperatures despite the varying load resistance. Unfortunately, this is not the case for the activity in the membrane ($\overline{a}_m^{H_2O}$) and at the anode side ($a_a^{H_2O}$) due to the combination of electro-osmotic drag and closed anode as was already mentioned. The activity at the anode side is only upper bounded by its reference value. This leads, together with the constant control of the cathodic activity, to an upper bound for the activity in the membrane too.

Another point that can be seen from Fig. 6.5 is that the controlled PEMFC compared to the uncontrolled one responds to changes in the cell temperature in a reverse manner. The activities $a_a^{H_2O}$ and $\overline{a}_m^{H_2O}$ in the anode and the membrane are

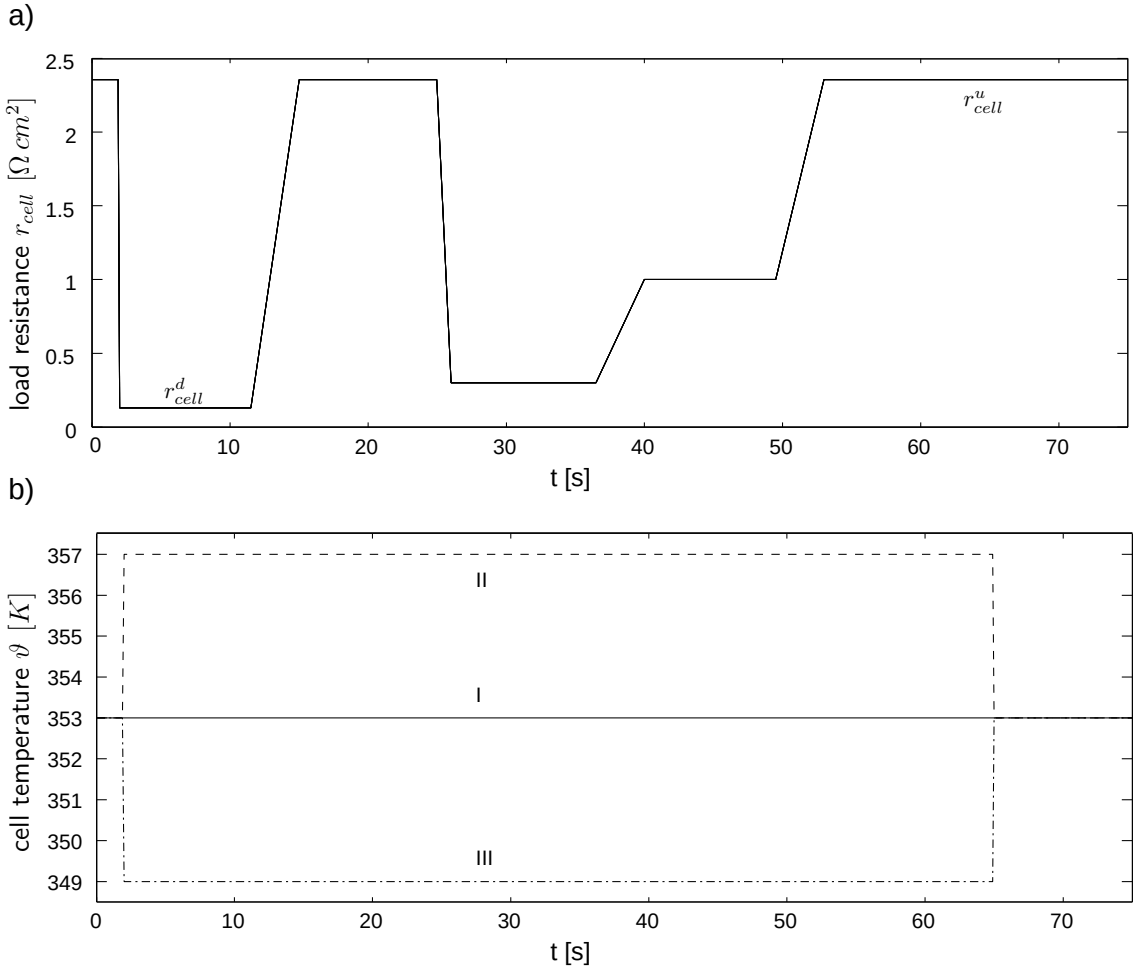

Figure 6.4: a) Development of the load resistance and b) the cell temperature with time.

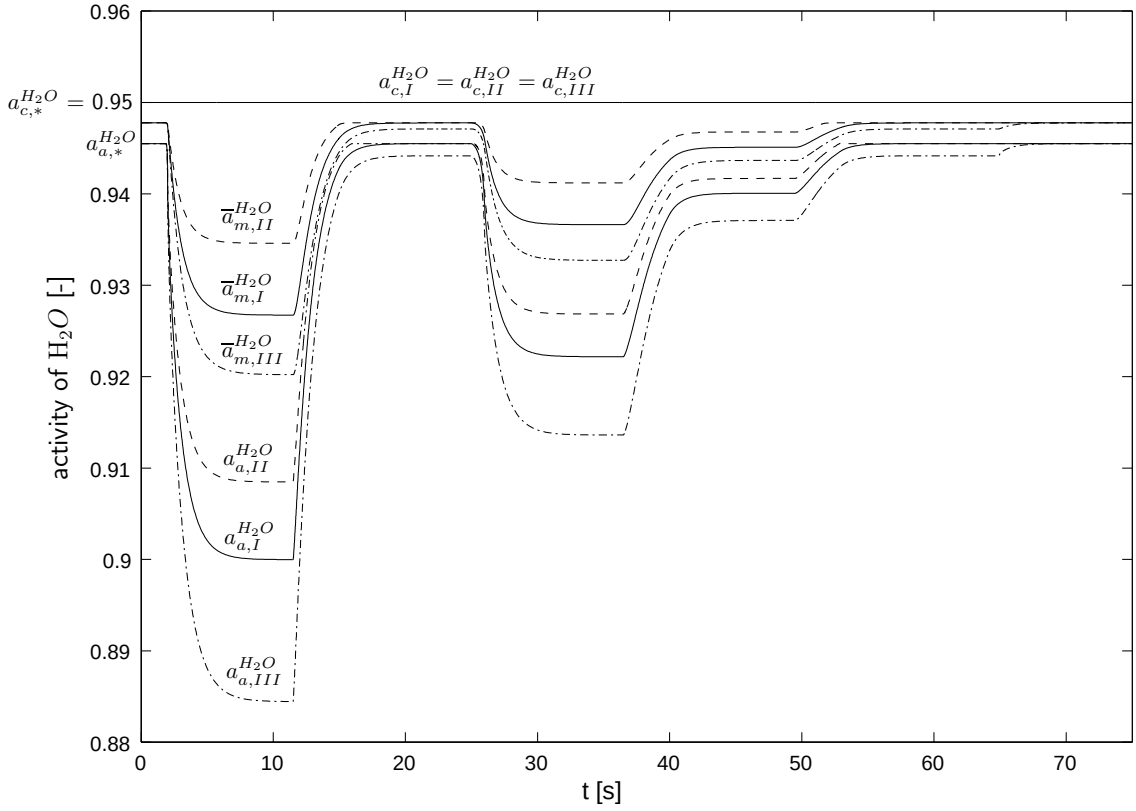

Figure 6.5: Activity of water vapor in the anode, the cathode and the membrane for the three temperature regimes $I - III$.

larger at higher temperatures and smaller at lower ones. This is not the case in the uncontrolled PEMFC, where undesired high (low) temperatures lead to drying out (flooding) and smaller (larger) activities in the cell. The reason for this inverse and favorable behavior is that the transport coefficient for the activity based transport in Eqn. 2.72 is becoming larger (smaller) at higher (lower) temperatures. This leads together with the constant control of the cathodic activity to a smaller (larger) activity gradient in the membrane and therefore to larger (smaller) activities in the membrane and the anode.

The content of hydrogen and oxygen in the fuel cell is given in Fig. 6.6. While the

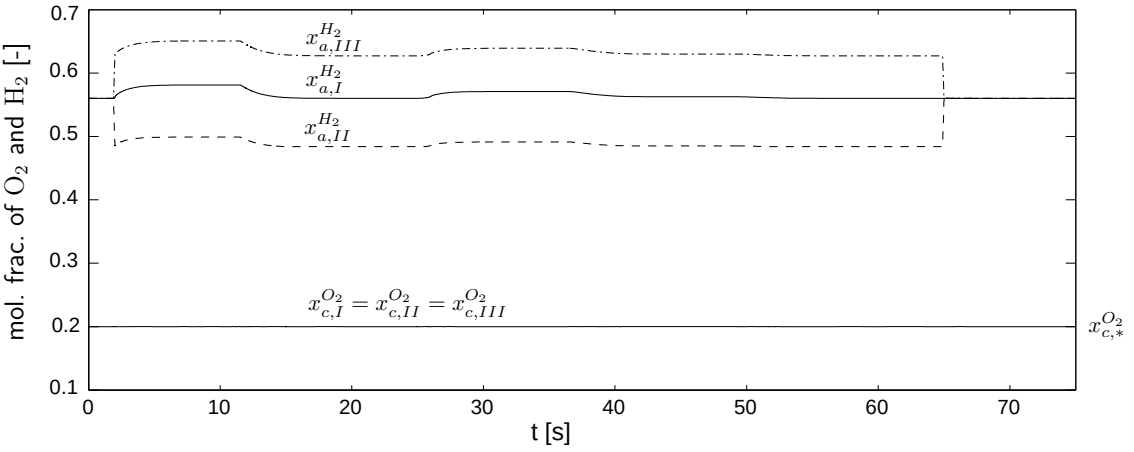

Figure 6.6: Hydrogen and oxygen content in the PEMFC for the three temperature regimes $I - III$.

oxygen content is held at its reference value by the controller, the hydrogen content varies due to the varying activity at the anode side. Despite that, an undersupply of the fuel cell with hydrogen is in general not possible, i.e. $x_a^{H_2} = 1 - a_a^{H_2O}\, p_{sat}/p_a^g > 0$ is in general valid. This is due to the control approach, that avoids flooding at the anode, i.e. $a_a^{H_2O} < 1$ and the common assumption for the given fuel cell operation, that the quotient of saturation pressure and overall gas pressure is in general less than one.

The cell current and the cell power that are drawn from the fuel cell are shown in Fig. 6.7 and Fig. 6.8 respectively. It can be seen, that the different temperature regimes in Fig. 6.4b cause different cell currents and cell powers. This is due to the varying proton conductivity in the membrane and has two causes. The first cause is the varying membrane activity ($\overline{a}_m^{H_2O}$) in Fig. 6.5 which is induced by the insufficient supply of the anode side with humidity raised by the combination of electro-osmotic drag and the closed anode. The second reason is the varying cell temperature which leads to a higher (lower) proton conductivity with larger (smaller) temperature. The second effect can be compensated by a suitable temperature control approach, while the first effect cannot be avoided with the given control approach because it is determined by the usage of the closed anode. It can be obviated by using an open

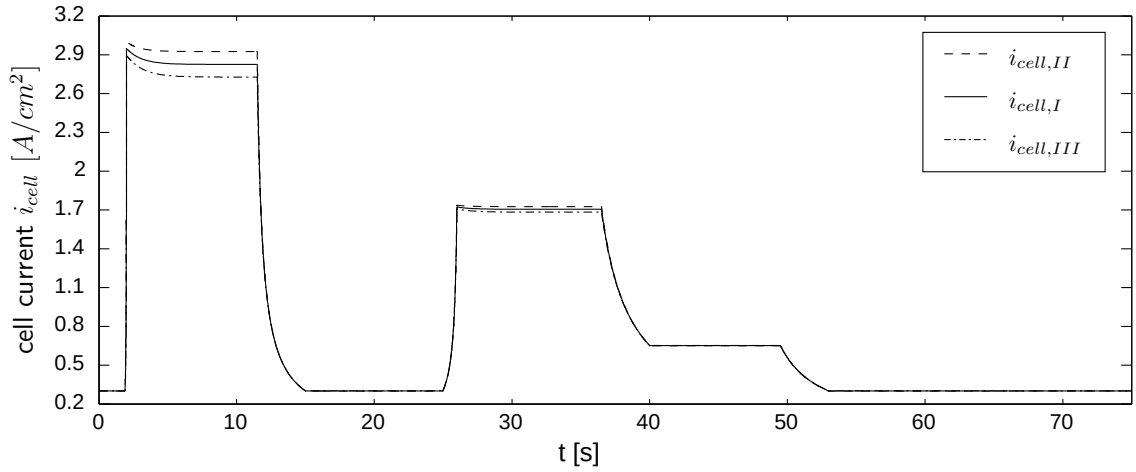

Figure 6.7: Cell current of the controlled fuel cell for the temperature regimes $I - III$.

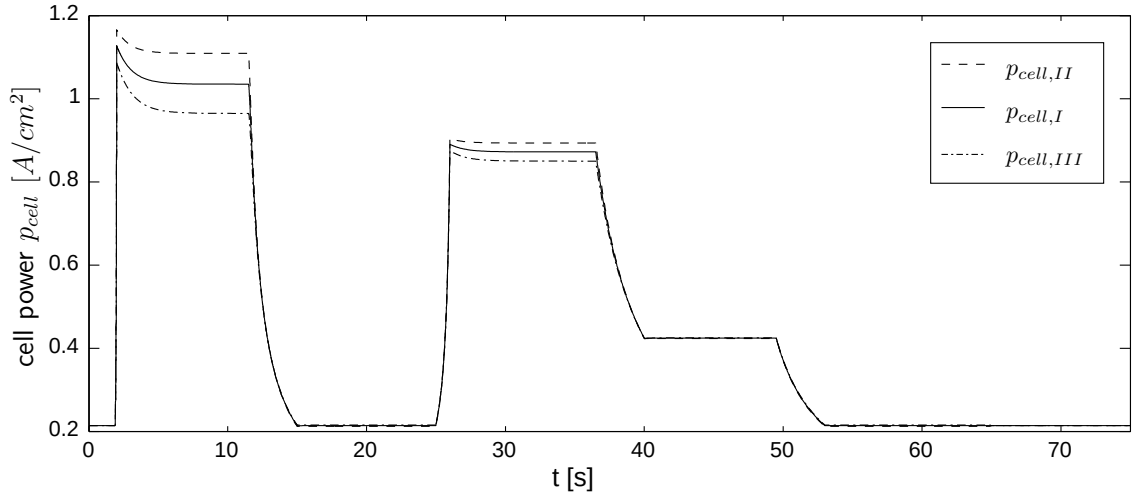

Figure 6.8: Cell power of the controlled fuel cell for the temperatures regimes $I - III$.

gas manifold at the anode side like it is done at the cathode side. This offers the possibility to compensate the electro-osmotic drag and avoid a dehumidification of the anode by an increased humidification stream at the inlet. For this purpose a control approach analog to the one at the cathode side could be used. The drawback of the open anode is, that unconsumed hydrogen can leave the anode and is wasted if no recycle is implemented there. This is automatically avoided with the closed anode and its major benefit.

Another point that comes with the usage of the proposed control approach is the transient behavior of the cell current and the cell power. From Fig. 6.7 and Fig. 6.8 one can see that the response of the cell current and the cell power to decreased load resistances, i.e. to a higher power demand is accompanied by overshoots of both quantities. This is a favorable behavior and not present in the uncontrolled PEMFC. The reason for this can be explained with the instantaneous behavior of the controlled fuel cell [87]. The instantaneous behavior is given by considering the processes in the fuel cell with fast transients, like the electrochemical reactions as dynamic and treating the slower processes like the mass transports and the electro-osmotic drag as static. With this, and the fact that the electro-osmotic drag is small (large) at small (high) power demand, the instantaneous behavior of the controlled PEMFC towards increasing power demand is therefore characterized by higher activities in the membrane and the anode compared to the stationary profiles of the fuel cell. This leads to a higher instantaneous proton conductivity of the membrane and therefore to higher instantaneous cell currents and cell powers for the same load resistance and causes the overshoots in Fig. 6.7 and Fig. 6.8.

The development of the input variables over time is depicted in Fig. 6.9 and can be physically explained as is outlined in the following. First of all, the input variables change according to the varied load resistance. This can be seen from the nominal case I. A decrease in the load resistance (Fig. 6.4a) results in an increased oxygen consumption and water production in the fuel and forces the controller to increase the volume flow rate of air and to lower the activity in the cathode inlet to compensate for that and vice versa. The controller at the anode side performs no control action in the nominal case, since the activity there does not exceed the reference value (Fig. 6.5). The input variables also change with the temperature regimes $I - III$. This is due to the impact of the temperature upon the gas composition in the fuel cell. The total concentration χ^{tot} of the gas phase at both electrodes is described according to Table 2.4 with the ideal gas law: $\chi^{tot}_{a/c} = p^g_{a/c}/\varrho\vartheta$. If the cell temperature is decreased (increased), χ^{tot} increases (decreases). Therefore, the molar flow $J_c^{O_2} = \dot{V}_{c,b}\,\chi_c^{tot}\,x_{c,b}^{O_2}$ that is necessary to supply the fuel cell with oxygen decreases (increases) in comparison to their nominal value. This is done by lowering (raising) the volume flow rate as can be seen from Fig. 6.9c. An analog reasoning is in general valid for the activity at the cathodic inlet in Fig. 6.9a with one exception: At very low volume flow rates caused by large increases in the load resistance and lower (higher) temperatures as normal, the cathodic inlet activity increases (decreases) beyond its nominal value in order to hold the activity in the cathode. This can be seen in Fig. 6.9a between 10 and 20 seconds for the cases II and III. The

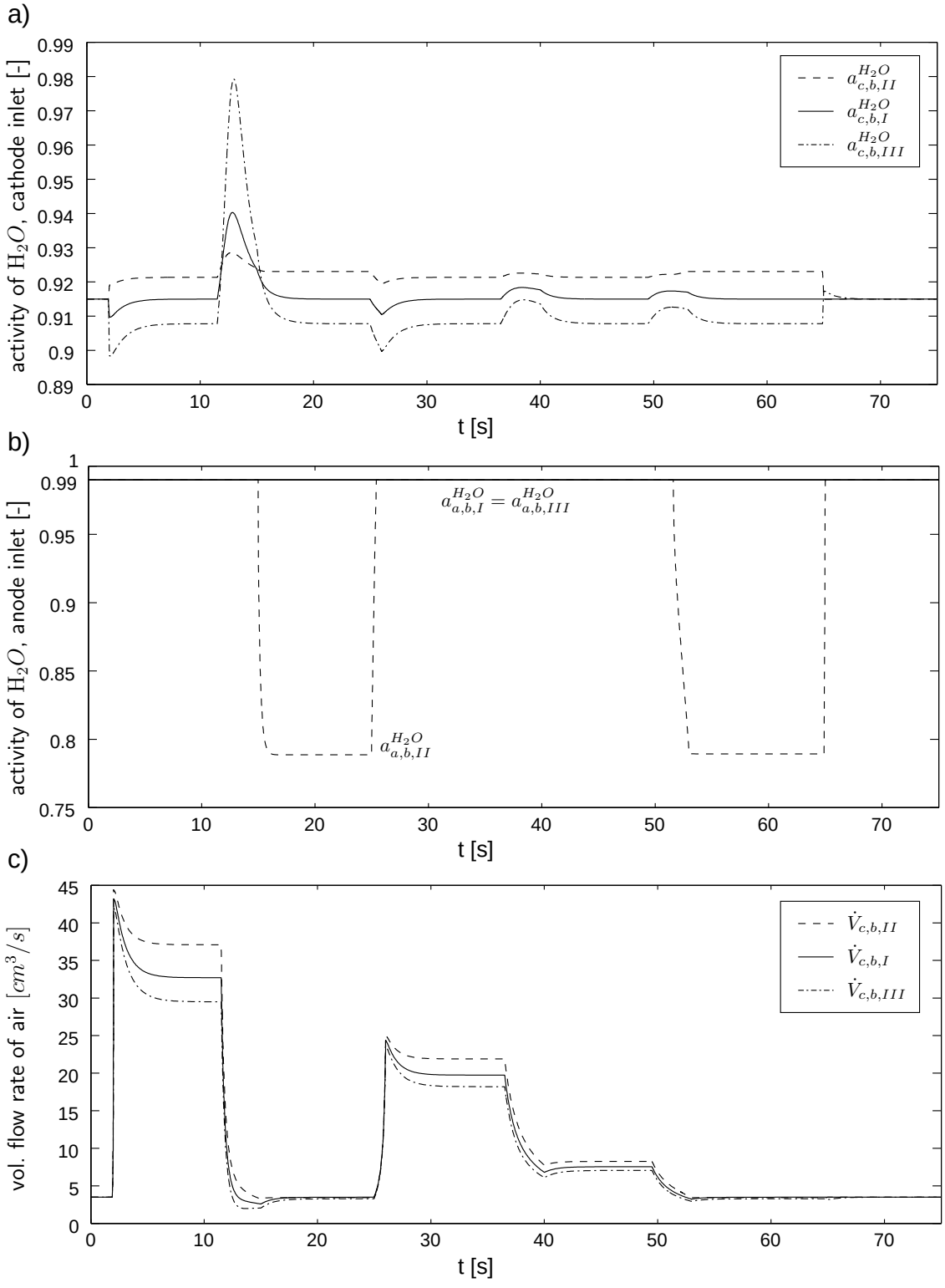

Figure 6.9: Time plots of the input variables for the temperature regimes $I - III$; Shown are a) the activity of water vapor in the cathode, b) in the anode, and c) the volume flow rate of air entering the cathode.

behavior of the inlet activity at the anode side in Fig. 6.9b is quite different from the above. It is at its maximum value for activities in the anode that are smaller or equal to the reference value. Another control action is only possible in the reverse case, i.e. if the anodic activity is going to exceed its reference value. This happens at higher temperatures and at high load resistances. In this case, the flow of water vapor that enters the anode, given by

$$J_a^{H_2O} = A \left(\frac{i_{cell}}{\zeta_c F} + N_a^{H_2O} \right) a_{a,b}^{H_2O} \frac{p_{sat}}{p_a^g} , \tag{6.44}$$

is higher than its nominal value due to the higher values of $N_a^{H_2O}$ (Fig. 6.10) and p_{sat}. Therefore, in order to hold the anodic activity at its reference value, the controller

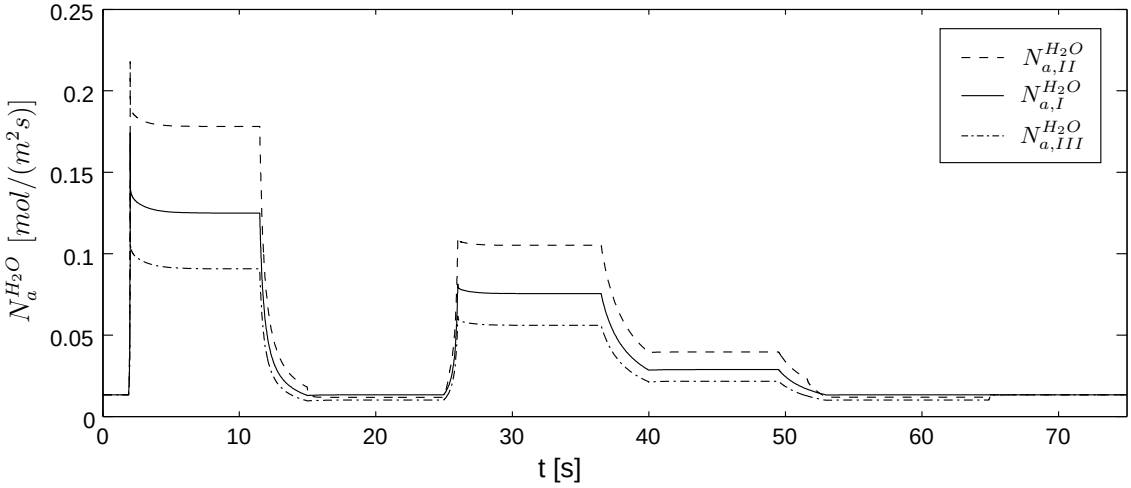

Figure 6.10: Molar flow density of water vapor that enters the membrane at the anode side depicted for the temperature regimes $I - III$.

decreases the inlet activity at the anode side, see $a_{a,b,II}^{H_2O}$ in Fig. 6.9b.

Further critical parameters with respect to the water household in fuel cell operation are the overall gas pressures in the electrodes. A variation in these quantities can quickly cause flooding or drying out in an uncontrolled PEMFC. Therefore, the robustness of the proposed control approach with respect to variations in the gas pressures is also studied. For this purpose, the overall gas pressure in both electrodes is altered according to Fig. 6.11. Three cases are considered. In the first case, the gas pressure is at its nominal value while in the other two cases a higher and a lower gas pressure is used for the dynamic simulation. The maximum variation of the pressure is approximately given by the tensile strength of a water soaked membrane [4]. For the following simulation the same changes in the load resistance as for the previous simulation study is used (Fig. 6.4a). First of all, the gas pressure p_c^g in the cathode is varied according to Fig. 6.11. It is found that the control approach is able to compensate the variations and hold the activity, the oxygen content and

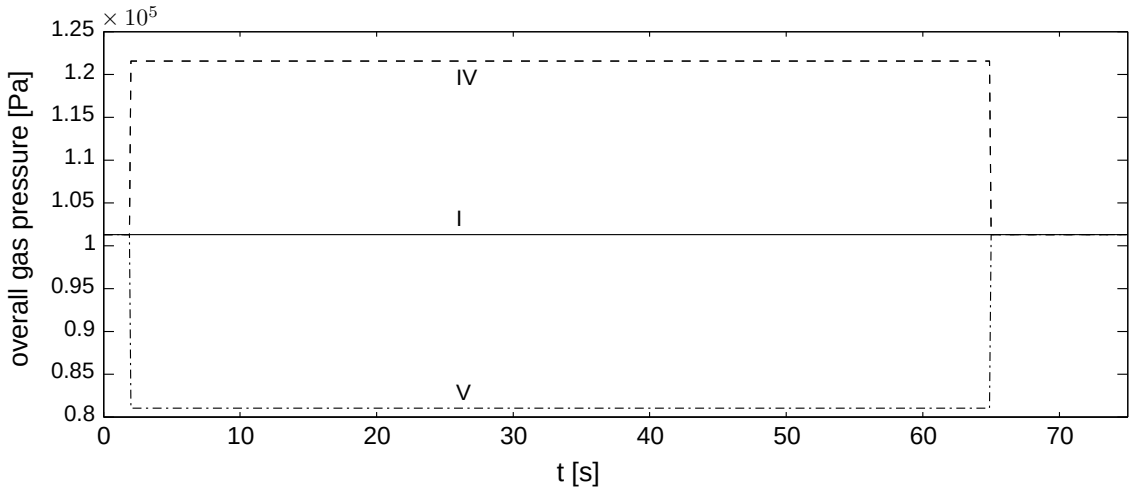

Figure 6.11: Variation of the overall gas pressure with time.

therefore also the cell current and the cell power in the fuel cell for cases IV and V are equal to the nominal case I in Fig. 6.5, Fig. 6.6, Fig. 6.7 and Fig. 6.8. This is not surprising due to the exclusive impact of the pressure variation at the cathode side and the usage of the cathodic activity as control variable.

If the variation of the gas pressure p_a^g at the anode side is considered according to Fig. 6.11, a different behavior in relation to the humidity in the fuel cell is found. This is shown in Fig. 6.12. It can be seen that the activity in anode and the membrane is affected by the variation of the anodic gas pressure, while this is not the case for the cathodic activity. This change is due to the combination of electro-osmotic drag and closed anode again, and can be explained with Eqn. 6.44. An increase (case IV) of the anodic gas pressure p_a^g results in a smaller flow $J_a^{H_2O}$ of water vapor and leads due to the electro-osmotic drag to a larger decline as in the nominal case and vice versa. The altered activity in the anode and the membrane is in the same order of magnitude as in the previous simulations, where a variation of the cell temperature was considered (Fig. 6.5). Therefore, approximately the same absolute deviations in the cell current and the cell power as well as in the input variables appear.

6.5 Servo control

In this section, the control approach is tested towards servo control. Although servo control is not that important in fuel cell operation as set point control, there is a necessity for this too. Servo control becomes important at the start-up and the shut-down phase of the PEMFC. In the following, a simple shut-down or set point change of the humidity in the fuel cell is used to illustrate the ability of the control approach for servo control. For this purpose, nominal model parameters are chosen, the load

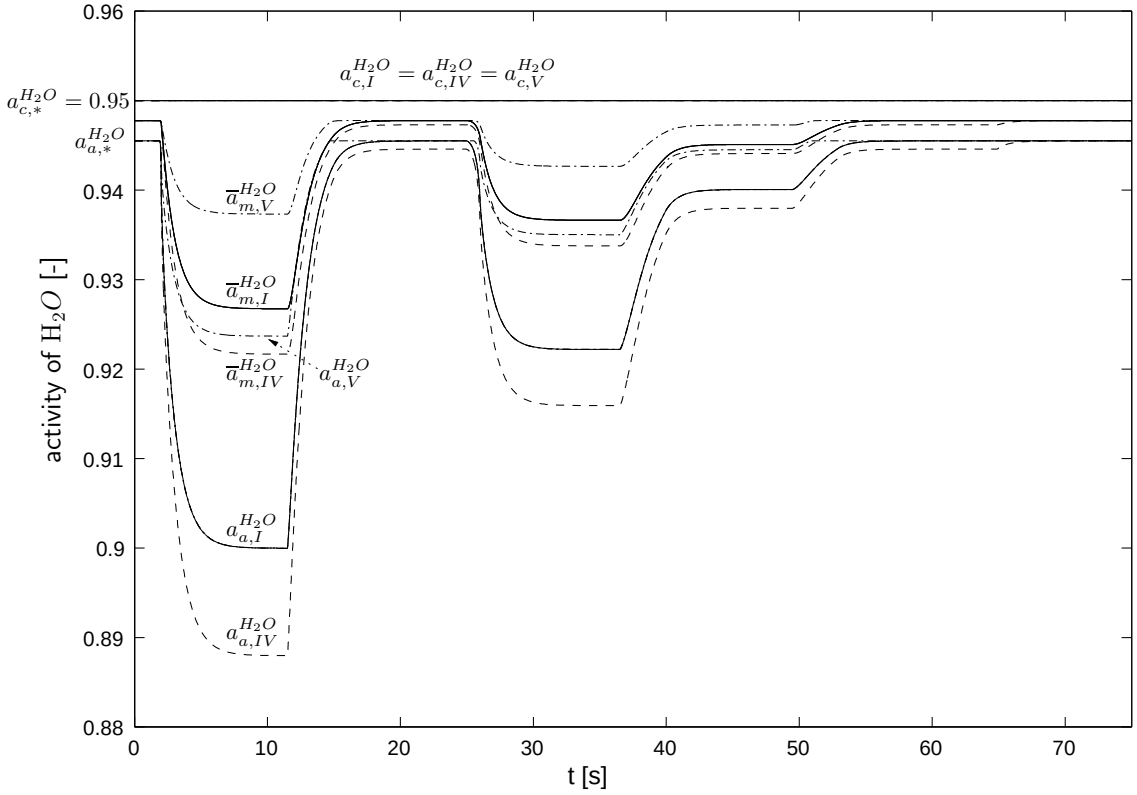

Figure 6.12: Activity of water vapor in the anode, the cathode and the membrane for the three pressure regimes I, IV and V of the overall anodic gas pressure p_a^g.

resistance remains constant at its upper value r^u_{cell} (Fig. 6.3a) and the reference trajectories in Fig. 6.13 are used. The starting point of the trajectories is given

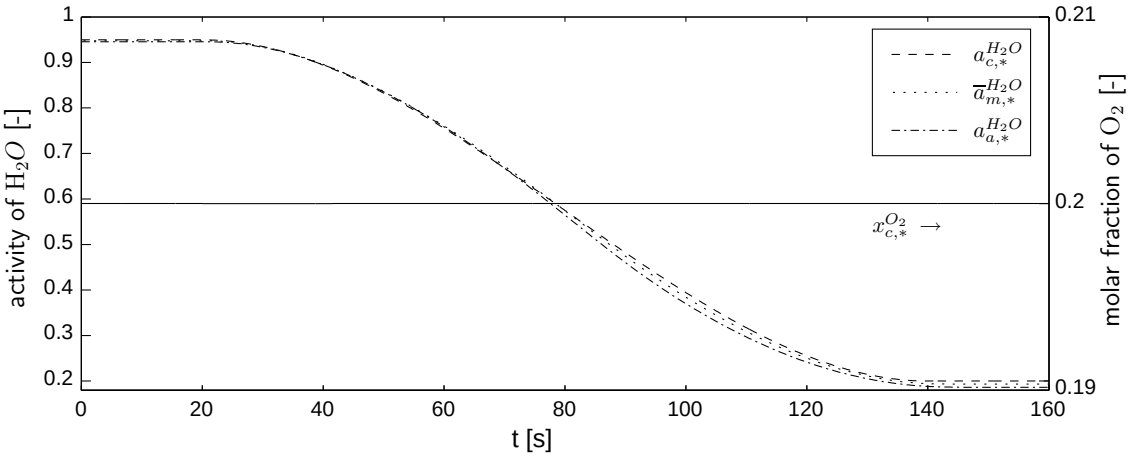

Figure 6.13: Reference trajectories used for servo control. The average membrane activity $\overline{a}^{H_2O}_{m,*}$ that results from the depicted activities in the electrodes is also shown.

by the set point used in the previous section for set point control. The endpoint is determined by the minimal activity that can be used in the membrane model from Weber [78]. It is not possible to use smaller values up to now. This is due to the fitting approach that Weber chooses and the experimental data that were available to him for the calculation of the proton conductivity in the membrane. This drawback could be overcome in the future by extending the validity of the membrane model towards lower activities but does not limit the capability of the control approach. Finally, a smooth transfer of the activities between the starting point and the end point is chosen.

The errors in the control variables are shown in Fig. 6.14. At the beginning of the time plot, an initial error is assumed that is typical in fuel cell operation: A too high humidity and a too low oxygen content is present in the PEMFC. This error could be the result of an uncompensated increase in the power demand in the fuel cell for example. It can be seen that the errors in the cathodic activity and the oxygen content vanish quite fast due to the control action. The transient behavior of the errors in the anodic activity and the average membrane activity is clearly slower due to the limited possible control action at the anode side caused by the closed anode as can be seen from the input variables in Fig. 6.15. Despite the fact that the anodic input variable $a^{H_2O}_{a,b}$ is at its minimum at the beginning, the error in the anodic control variable $a^{H_2O}_{a}$ decreases relatively slow. After the initial error vanishes in the anodic activity, the input variable increases and finally ends up at its maximum value $a^{H_2O}_{a,b,max}$. The input variables at the cathode side, i.e. $a^{H_2O}_{c,b}$ and $\dot{V}_{c,b}$ are also excited by the initial error but settle quicklier.

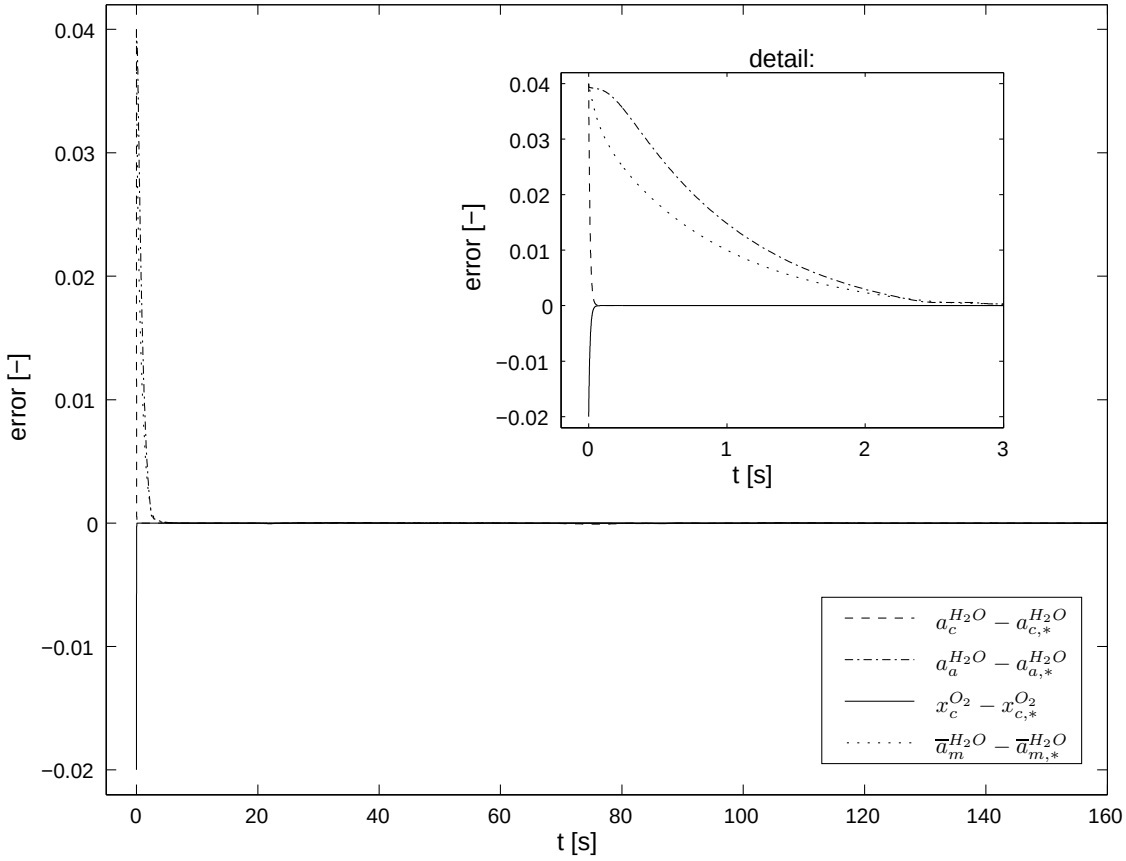

Figure 6.14: Absolute error of the control variables. The deviation of the average membrane activity $\overline{a}_m^{H_2O}$ from its reference value is also shown.

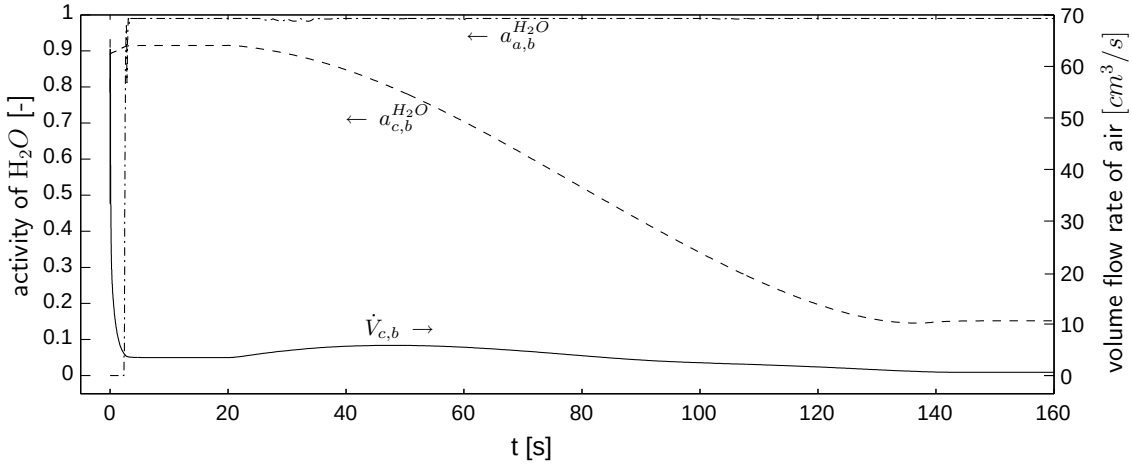

Figure 6.15: Development of the input variables at servo control.

6.6 Summary

In this chapter a passivity-based control study for a one-phase PEM fuel cell is presented. In a first step, the control objectives are stated. The main aims of the control approach are the avoidance of flooding and the undersupply of the fuel cell with oxygen and hydrogen. After that, a controllability analysis of the operating points of the PEMFC is carried out. This is done with a controllability criterion for linear time-invariant systems and step responses. It is found that the operating points are completely controllable and that the PEMFC can be controlled with decentralized controllers in the electrodes. In a third step, the principle of the passivity-based control approach is presented and applied to the PEMFC according to the results of the controllability analysis. Finally, the proposed control approach is tested in simulations for set point control and servo control. It is found that the control approach introduces upper limits for the activities in the fuel cell and can therefore prevent the building up of liquid water and avoid flooding, whereas an undersupply of the PEMFC with oxygen and hydrogen is avoided too. It is shown, that this is the case for nominal operating conditions as well as for disturbances in the cell temperature and the overall gas pressures in the electrodes, which can quickly lead to flooding in an uncontrolled cell. Unfortunately, the drying out of the anode side due to the electro-osmotic drag cannot be prevented by the control approach. It is pointed out, that this is caused by the use of a closed electrode at the anode side, which cannot maintain a sufficiently high humidification stream to compensate the impact of the electro-osmotic drag upon the anode and as consequence upon the membrane too. It is expected, that this circumstance can be eliminated by the use of an open gas channel at the anode like at the cathode and an analogous control design there.

CHAPTER 7

Conclusion

This work deals with the model-based analysis and control of PEM fuel cells. In chapter 3 a bifurcation analysis is performed with a rigorous two-phase PEMFC model in order to examine the behavior of two-phase PEM fuel cells close to flooding conditions. During this analysis, a steady state multiplicity is found. Their origin can be physically explained and results from different liquid water saturations in the PEMFC. After that, the multiplicity's dependency from several practical relevant fuel cell parameters, like the humidities in the gas bulks, the fraction of hydrophilic pores and the porosity and permeability of the gas diffusion and catalyst layers is studied in order to further characterize this bifurcation. Finally, the transient behavior of the fuel cell around the multiplicity is tested in dynamic simulations. The results obtained in chapter 3 characterize the stationary and dynamic behavior of two-phase PEMFCs at flooding conditions and can contribute to a better understanding and improvement of their performance.

After the behavioral analysis in chapter 3, a next step is taken towards the control of PEM fuel cells in chapter chapter 4. In this chapter, a model reduction based upon simplified physical assumptions is performed, in order to obtain a two-phase model that can be used in a real-time process control environment. The resulting model captures the steady-state multiplicity found in the original model and therefore shows good qualitative as well as acceptable quantitative agreement with the detailed model. The reduced model is of considerably lower order than the detailed model, because the number of dynamic states is decreased from 130 of the detailed model to 5 of the reduced model. The reduction in computation time is in the same order of magnitude, while the reduced model order also eases the application of nonlinear control approaches to PEM fuel cells.

Prior to the development of a fuel cell control strategy in chapter 6, the behavior of PEM fuel cells and DC-DC converters is analyzed in chapter 5. This is done, because DC-DC converters are often connected to PEMFCs in order to adapt the DC electricity from the fuel cell to the load's demands, and prior to this analysis, it

was not clear if such a connection might introduce multiplicities or instabilities in the connected system. This analysis is done for three common DC-DC converters: The boost, the buck and the buck-boost converter. First of all, the effect of the converter ripples are shown. They introduce oscillations in the fuel cell. Their origin is explained, discussed and possibilities for their suppression are given. After that, the overall behavior of the coupled systems is examined. It is shown mathematically that the connection between PEM fuel cells and boost, buck and buck-boost converters can neither lead to stationary multiplicities nor to oscillations in the coupled systems. As a consequence, it is not necessary to develop integrated control approaches for the couplings. Instead, we can concentrate on the development of control strategies considering only the PEMFC and can use existing control approaches for the DC-DC converters [20] in order to control both subsystems.

Finally in this contribution, a passivity-based control study for a one-phase PEM fuel cell is presented. The main aims of the control approach are the avoidance of flooding and the undersupply of the fuel cell with oxygen and hydrogen. Prior to the control design, a controllability analysis of the PEMFC is carried out. It is found that the operating points are completely controllable and that the PEMFC can be controlled with decentralized controllers in the electrodes. After that, a passivity-based control approach is presented and applied to the PEMFC according to the results of the controllability analysis. In the next step, the proposed control approach is tested in simulations for set point control and servo control. It is found that the control approach introduces upper limits for the activities in the fuel cell and can therefore prevent the building up of liquid water and avoid flooding, whereas an undersupply of the PEMFC with oxygen and hydrogen is avoided too. It is shown that this is the case for nominal operating conditions as well as for disturbances in the cell temperature and the overall gas pressures in the electrodes, which can quickly lead to flooding in an uncontrolled PEM fuel cell. After the successful test of the passivity-based control approach under one-phase conditions, it could now be applied to two-phase PEMFCs. This can be done in the future by using the reduced fuel cell model presented in chapter 3 combined with the two-phase gas bulks modeled in [60].

APPENDIX A

Derivations and remarks

A.1 Derivation of the reduced two-phase model

The reduced two-phase PEMFC model originates from the distributed two-phase model in chapter 3. In the following the derivation of the balance equations of the reduced model is shown.

Balance of liquid water. In the detailed model, liquid water mass balances are formulated in the catalyst and gas diffusion layers at the anode and the cathode side. They are given in Eqn. 2.7. In a first step, the balances are integrated over the layers (Fig. 2.4), i.e. from $d\Omega_1$ to $d\Omega_3$ and from $d\Omega_4$ to $d\Omega_6$ at the anode and the cathode side respectively. This results in the averaged liquid water balances in Eqn. 2.43. The mass flows $j^l_{\epsilon,b}$ model the liquid water flows from the bulks to the electrodes and are given by the mass flows of the detailed model in Eqn. 2.36 and Eqn. 2.37, i.e.

$$j^l_{a,b} := \tilde{j}^l_1|_{d\Omega_1} \quad \text{and} \quad j^l_{c,b} := -\tilde{j}^l_5|_{d\Omega_6} \,. \tag{A.1}$$

The pressure gradients in these two equations are determined by the boundary conditions in Eqn. 2.8d, i.e. the liquid water pressures at the bulk boundaries are equal to the gas pressures there. This result leads to Eqn. 2.44, whereas the pressure gradients are approximated by

$$\left.\frac{\partial \tilde{p}^l_1}{\partial z}\right|_{d\Omega_1} \approx \frac{p^l_a - p^l_{a,b}}{\beta_l(d_{gdl} + d_{catl})} \quad \text{and} \quad \left.\frac{\partial \tilde{p}^l_5}{\partial z}\right|_{d\Omega_6} \approx \frac{p^l_c - p^l_{c,b}}{\beta_l(d_{gdl} + d_{catl})} \,, \tag{A.2}$$

where the liquid water pressures in the bulks, $p^l_{a,b}$ and $p^l_{c,b}$, are set to the gas pressure p_g.

The mass flows $j^l_{\epsilon,m}$ in Eqn. 2.43 are calculated from the flows in Eqn. 2.45. Equation 2.45 itself can be derived from the distributed membrane model given in subsection 2.1.4, as will be shown in the following. The membrane humidity in the distributed model is given by Eqn. 2.16. For the reduced model, it is assumed that the membrane dynamics can be neglected compared to the slow liquid water dynamics in the catalyst and gas diffusion layers which dominate the transition behavior of the fuel cell at two-phase operation. This result was found during dynamic simulation studies performed for the results in chapter 3. With this assumption and after integrating Eqn. 2.16 from $d\Omega_3$ to $d\Omega_4$ we get:

$$0 = -\tilde{N}_{H_2O}|_{d\Omega_4} + \tilde{N}_{H_2O}|_{d\Omega_3} \,. \tag{A.3}$$

The quantity $\tilde{N}_{H_2O}$ models the transport of water vapor and liquid water through the membrane. In the reduced model the transport of water vapor is neglected and therefore only the transport of liquid water is considered:

$$\tilde{N}^l_{H_2O}\Big|_{d\Omega} := \tilde{S}\left(-\tilde{\alpha}_l\, v_l \frac{\partial \tilde{p}^{cp}_3}{\partial z} - \frac{\tilde{\sigma}^p_3\, \xi_l}{F}\frac{\partial \tilde{\phi}^p_3}{\partial z}\right)\Bigg|_{d\Omega} \tag{A.4}$$

with $d\Omega \in \{d\Omega_3, d\Omega_4\}$. The above equation differs from Eqn. 2.17 also in terms of the hydraulic transport coefficient. In Eqn. A.4, the hydraulic transport coefficient is simplified and only made up from $\tilde{\alpha}_l$ and v_l. This is done, because the other contributing term $\tilde{\sigma}^p_3 \xi^2_l / F^2$ is more than five orders of magnitude smaller then $\tilde{\alpha}_l$. Another approximation in Eqn. A.4 concerns the calculation of the pressure gradient in the membrane. In the reduced model it is approximated by a difference pressure gradient made up from the liquid water pressures in both electrodes:

$$\frac{\partial \tilde{p}^{cp}_3}{\partial z}\bigg|_{d\Omega} \approx \frac{p^l_c - p^l_a}{\beta_m d_m} \,. \tag{A.5}$$

Finally, the second term inside the brackets in Eqn. A.4 is also simplified for the reduced model by using the proton charge balance of the membrane given in Eqn. 2.3 of the detailed model. The integration of Eqn. 2.3 from $d\Omega_3$ to $d\Omega_4$ together with the definition of the cell current in Eqn. 2.4 leads to

$$-\tilde{\sigma}^p_3 \frac{\partial \tilde{\phi}^p_3}{\partial z}\bigg|_{d\Omega_4} + \tilde{\sigma}^p_3 \frac{\partial \tilde{\phi}^p_3}{\partial z}\bigg|_{d\Omega_3} = 0 \quad \text{and} \quad \tilde{\sigma}_p \frac{\partial \tilde{\phi}^p_3}{\partial z}\bigg|_{d\Omega} = -i_{cell} \tag{A.6}$$

for $d\Omega \in \{d\Omega_3, d\Omega_4\}$. If we now substitute $\tilde{S}$ and $\tilde{\alpha}$ by their replacements in the reduced model given in Eqn. 2.46 and Eqn. 2.48, and use Eqn. A.5 and Eqn. A.6 in Eqn. A.4 we get

$$\tilde{N}^l_{H_2O}\Big|_{d\Omega} = S\left(-\alpha_l\, v_l \frac{p^l_c - p^l_a}{\beta_m d_m} + \frac{\xi_l}{F} i_{cell}\right) \tag{A.7}$$

for $d\Omega \in \{d\Omega_3, d\Omega_4\}$. If we take the boundary conditions in Eqn. 2.29a and Eqn. 2.29b without the neglected vapor transport into account, i.e.

$$\tilde{j}^l_{a,m} = M_{H_2O}\, \tilde{N}^l_{H_2O}|_{d\Omega_3} \quad \text{and} \quad \tilde{j}^l_{c,m} = M_{H_2O}\, \tilde{N}^l_{H_2O}|_{d\Omega_4} \,, \tag{A.8}$$

and define $j^l_{a,m} := -\tilde{j}^l_{a,m}$ and $j^l_{c,m} := \tilde{j}^l_{c,m}$, we finally come up with Eqn. 2.45.

Balance of gas components. In the detailed model the mass balances for the gas components are formulated in the CATL and GDL for both electrodes. At the cathode side they read they are given by Eqn. 2.13. In a first step, the balances are integrated over the layers, i.e. from $d\Omega_4$ to $d\Omega_6$. With the assumptions that no oxygen or water vapor is transported through the membrane the following averaged equation results:

$$\frac{d\hat{\rho}_c^\iota}{dt} = \frac{1}{d_{gdl}+d_{catl}}\tilde{j}_5^\iota|_{d\Omega_6} + Q_c^g \tag{A.9}$$

$$\text{with} \quad Q_c^g := \begin{cases} -Q_c^l - \frac{M_{H_2O}}{2F}\frac{\int_{d\Omega_4}^{d\Omega_5}\tilde{Q}_c^{ch}dz}{d_{gdl}+d_{catl}} & \text{for } \iota = \mathrm{H_2O} \\ \frac{M_{O_2}}{4F}\frac{\int_{d\Omega_4}^{d\Omega_5}\tilde{Q}_c^{ch}dz}{d_{gdl}+d_{catl}} & \text{for } \iota = \mathrm{O_2} \end{cases} .$$

The term $\tilde{j}_5^\iota|_{d\Omega_6}$ describes the mass flow of oxygen and water vapor from the cathode to the cathode bulk. In the reduced model this term is approximated by:

$$\tilde{j}_5^\iota|_{d\Omega_6} = -\left(\hat{D}_5^\iota(1-\tilde{s}_\kappa^l)^2\frac{\partial\tilde{c}_\kappa^\iota}{\partial z}\right)\Bigg|_{d\Omega_6} \approx \underbrace{-\hat{D}_c^\iota(1-\tilde{s}_\kappa^l)^2\frac{c_{c,b}^\iota - c_c^\iota}{\beta_\iota(d_{gdl}+d_{catl})}}_{-j_{c,b}^\iota :=} , \tag{A.10}$$

where the differential gradient is expressed by a difference gradient and the boundary conditions from Eqn. 2.14d are included. The integral in Eqn. A.9 can be further simplified with the proton charge balance in the cathodic catalyst layer and the cell current:

$$\int_{d\Omega_4}^{d\Omega_5}\tilde{Q}_c^{ch}dz = \int_{d\Omega_4}^{d\Omega_5}\frac{\partial}{\partial z}\left(-\tilde{\sigma}_4^p\frac{\partial\tilde{\phi}_4^p}{\partial z}\right)dz = -i_{cell} . \tag{A.11}$$

Finally, if Eqn. A.10 and Eqn. A.11 are used in Eqn. A.9 the gas balance of the reduced model at the cathode side in Eqn. 2.51 results. The derivation of the gas balance at the anode side can be done analog to the above one.

A.2 Determination of the fitting parameters

In the reduced two-phase model in chapter 4, four parameters are used to fit its quantitative behavior towards the detailed model in chapter 3: β_m, β_{O_2}, β_{H_2O} and β_l. All four are introduced by approximating the gradients of the detailed model during the model reduction (section A.1). Originally, all four fitting parameters are set to $\beta = 1$. With this setting there is already a qualitative agreement between detailed and reduced model observable. In order to improve the quantitative agreement of both models the fitting parameters are adjusted. This is described in the following. The parameter adaption is done iteratively in simulation studies comparing the results of the reduced model with that of the detailed model for nominal parameter values of f_{HI}, $c_{a,b}^{H_2O}$, $c_{c,b}^{H_2O}$. The fuel cell models are operated in rheostatic mode and

the adaption is done in two steps. In a first step, the reduced model is adapted to reproduce the influence of the bulk humidities upon the multiplicity. For this, three parameters are used: β_m, β_{O_2} and β_{H_2O}. The parameter β_{H_2O} has a strong influence upon the first turning point of the steady state multiplicity (see points 1, 3, 5 in Fig. 3.2b for example). So it is used to approximate the stationary and dynamic behavior there. The influence of the other two parameters β_m, β_{O_2} is smaller there. They are used to adapt the second turning point (see points 2,4,6 in Fig. 3.2b for example) and the following stable branch. Both turning points are stationary characterized by a high liquid water saturation. Dynamically, large transition times towards and from this stable branch due to the slow liquid water dynamics are observed. The parameters β_m and β_{O_2} are now used to adapt the stationary and dynamic behavior of the reduced model there. This is done under the condition that the behavior at the first bifurcation remains nearly unchanged. While the parameter β_m is used to improve the dynamic behavior, e.g. the transition times of the liquid water dynamics, the parameter β_{O_2} is used to approximate the stationary behavior. In a second step, the reduced model is adapted to reproduce the influence of the liquid water outflow of the cell. This is achieved by adapting the parameter β_l. The parameters β_m, β_{O_2} and β_{H_2O} remain constant during this adaption.

A.3 Derivation of the one-phase PEMFC model

In this section, the equations for the simple and one-phase fuel cell model in chapter 5 are derived. In a first step, the differential equation for the overpotential in the PEMFC is derived from the equivalent electrical circuit in Fig. 2.5. The charge balance at the double layer capacitor C_{dl} reads $d\mathfrak{Q}/dt = i_{cell} - i_T$. The charge $\mathfrak{Q}$ can be expressed in terms of the overpotential to be $\mathfrak{Q} = -C_{dl}\,\eta_c$, where $\eta_c < 0$ holds. If the double layer capacitance is assumed to be constant and the current i_T is expressed using the Tafel equation

$$i_T := i_T^0\, x_c^{O_2}\, \exp(-b\eta_c) \quad \text{with} \quad b := (1-\varphi_c)\zeta_c F/\varrho\vartheta\,, \tag{A.12}$$

then the differential equation of the overpotential in Eqn. 2.63 results. The algebraic equation for the cell voltage in Eqn. 2.65 can be obtained using Kirchhoff's voltage law.

The model equations for the oxygen and the water content in the fuel cell are derived from the CSTR in Fig. 2.5. Mass balances for the species $\iota \in \{O_2, N_2, H_2O\}$ read

$$\dot{n}_c^\iota = \dot{V}_{c,b}\,\chi_{c,b}^\iota - \dot{V}_c\,\chi_c^\iota + \nu_c^\iota\, A\, i_T/\zeta_c F \tag{A.13}$$

where n_c^ι (χ_c^ι) describes the molar amount (concentration) of species ι in the CSTR. The symbol ν_c^ι denotes the stoichiometric coefficients of the cathodic reaction with $\nu_c^{O_2} = -0.5$, $\nu_c^{H_2O} = 1$ and $\nu_c^{N_2} = 0$ and the expression $i_T/\zeta_c F$ refers to the reaction rate and is given by Faraday's law. The volume flow rate of air at the inlet $\dot{V}_{c,b}$ is kept constant. The volume flow rate at the outlet $\dot{V}_c$ can be determined if the

gas phase is assumed to be isotherm, isobaric and ideal. The ideal gas law reads $p_g V_c = n_c^{tot} \varrho \vartheta$. The symbol $n_c^{tot} := \sum_\iota n_c^\iota$ denotes the total amount of gas inside the CSTR and is constant if isobaric, isothermic conditions as well as a constant CSTR volume V_c is assumed. This means $\dot{n}_c^{tot} = \sum_\iota \dot{n}_c^\iota = 0$. If the mass balances from Eqn. A.13 are inserted an algebraic equation for the output flow rate $\dot{V}_c$ results: $\dot{V}_{c,b} \sum_\iota \chi_{c,b}^\iota - \dot{V}_c \sum_\iota \chi_c^\iota + \sum_\iota \nu_c^\iota A\, i_T/\zeta_c F = 0$. This equation can be simplified if the total concentration in the CSTR $\chi_c^{tot} := n_c^{tot}/V_c = \sum_\iota n_c^\iota/V_c = \sum_\iota \chi_c^\iota = p_g/\varrho\vartheta = const.$ is defined. The total concentration in the CSTR and at the inlet is the same: $\chi_{c,b}^{tot} = \chi_c^{tot}$, because we assume an ideal and isobaric, isothermic gas phase in the inlet as well. With these simplifications the output flow rate can be written as

$$\dot{V}_c = \dot{V}_{c,b} + \sum_\iota \nu_c^\iota A\, i_T/\zeta_c F \chi_c^{tot} = \dot{V}_{c,b} + A\, i_T/2\, \chi_{tot}\, \zeta_c\, F\,. \tag{A.14}$$

If we insert the above equation in Eqn. A.13 and use $n_c^\iota = V_c\, \chi_c^\iota$ and the molar fractions $x_c^\iota := n_c^\iota/n_c^{tot} = \chi_c^\iota/\chi_c^{tot}$ and $x_{c,b}^\iota := \chi_{c,b}^\iota/\chi_c^{tot}$, then Eqn. 2.61 and Eqn. 2.62 result for $\iota = O_2, H_2O$.

A.4 Enlargement of the double layer capacitance

In this section it is briefly shown that a capacitor connected in parallel to a PEMFC can be used to increase the double layer capacitance of the cell. The capacitor with capacitance C_{II} is assumed to be lossless and is connected to the ports of the equivalent electrical circuit in Fig. 2.5. The capacitor can be used to suppress oscillations in the fuel cell induced by the duty cycle of a connected DC/DC-converter. A time interval of one duty period T is considered for the following equations. For the overpotential η_c and the cell voltage U_{cell}, Eqn. 2.63 and Eqn. 2.65 are still valid. The voltage at the new capacitor is identical to the cell voltage and is calculated by

$$C_{II} \frac{dU_{cell}}{dt} = i_{cell} - i\,, \tag{A.15}$$

where i denotes the new output current of the fuel cell that is different from i_{cell}. If Eqn. 2.65 is differentiated with respect to time and inserted in Eqn. A.15 one gets

$$C_{II} \left(\frac{d\eta_c}{dt} - r_m \frac{di_{cell}}{dt} \right) = i_{cell} - i\,, \tag{A.16}$$

where we have assumed that the change of the water content $x_c^{H_2O}$ in the cell is negligible over one duty period. If Eqn. 2.63 is differentiated with respect to time, under the assumption that the oxygen content $x_c^{O_2}$ is assumed to be constant, and solved for di_{cell}/dt we obtain

$$\frac{di_{cell}}{dt} = \frac{\partial i_r}{\partial \eta_c} \frac{d\eta_c}{dt} - C_{dl} \frac{d^2\eta_c}{dt^2}\,, \tag{A.17}$$

where i_T denotes the Tafel equation from Eqn. A.12. If Eqn. A.17 and Eqn. 2.63 are inserted for di_{cell}/dt and i_{cell} in Eqn. A.16 a second order ODE for the overpotential results:

$$r_m C_{dl} C_{II} \frac{d^2\eta_c}{dt^2} + \left(C_{dl} + C_{II} \left[1 - r_m \frac{\partial i_T}{\partial \eta_c} \right] \right) \frac{d\eta_c}{dt} = i_T(\eta_c) - i \,. \tag{A.18}$$

If the first term on the left hand side is negligible compared to the second term, e.g. if the fuel cell is well humidified and leads to a fairly small membrane resistance r_m, a first order ODE for the overpotential follows:

$$\left(C_{dl} + C_{II} \left[1 + r_m \, b \, i_T(\eta_c) \right] \right) \frac{d\eta_c}{dt} = i_T(\eta_c) - i \,. \tag{A.19}$$

This equation has the same structure as the original ODE for the overpotential in Eqn. 2.63, whereas the new equation and therefore the parallel connection of the fuel cell and the capacitor shows an increased double layer capacitance.

A.5 Formula for stationary oscillations of the overpotential in a PEMFC if connected to buck or buck-boost converters

In this section the formula in Eqn. 5.24 is derived. The ODE for the overpotential in Eqn. 5.23 is used as a starting point. It is assumed that the changes in the inductor current I_{ind} and the oxygen content $x_c^{O_2}$ are small over one duty period T of the converter, and can be approximately replaced by their average values $\overline{I}_{ind}$ and $\overline{x}_c^{O_2}$. If the switching function q is defined by

$$q := \begin{cases} 1 & \text{for} \quad t \in \mathfrak{T}_{on} := [t_0, t_0 + t_{on}[\\ 0 & \text{for} \quad t \in \mathfrak{T}_{off} := [t_0 + t_{on}, t_0 + T[\end{cases} \tag{A.20}$$

the following nonlinear ODE in η_c results:

$$C_{dl} \, \dot{\eta}_c = \begin{cases} -\overline{I}_{ind}/A \;+\; i_T^0 \, \overline{x}_c^{O_2} \, \exp(-b\eta_c) & \text{for} \quad t \in \mathfrak{T}_{on} \\ \qquad\qquad\quad i_T^0 \, \overline{x}_c^{O_2} \, \exp(-b\eta_c) & \text{for} \quad t \in \mathfrak{T}_{off} \end{cases} \tag{A.21}$$

with initial conditions $\eta_c(t_0) = \eta_{c_0}$ and $\eta_c(t_0 + t_{on}) = \eta_{c_1}$. With the following change in variables $w := \exp(b\eta_c)$ and the definitions $h := b\,\overline{I}_{ind}/A\,C_{dl}$ and $g := b\,i_T^0\,\overline{x}_c^{O_2}/C_{dl}$ a linear ODE in w can be obtained:

$$\dot{w} = \begin{cases} -h\,z \;+\; g & \text{for} \quad t \in \mathfrak{T}_{on} \\ \qquad\quad g & \text{for} \quad t \in \mathfrak{T}_{off} \end{cases} \,. \tag{A.22}$$

This ODE can be solved easily and the solution in the original variables reads

$$\eta_c^{on} = \frac{1}{b} \ln \left(\frac{g}{h} + \left(\exp(b\,\eta_{c_0}) - \frac{g}{h} \right) \exp(-h(t - t_0)) \right) \text{ for } t \in \mathfrak{T}_{on} \,, \tag{A.23}$$

$$\eta_c^{off} = \frac{1}{b} \ln \left(\exp(b\,\eta_{c_1}) + g(t - (t_0 + t_{on})) \right) \text{ for } t \in \mathfrak{T}_{off} \,. \tag{A.24}$$

With the above solutions we can now define the oscillation amplitude $\Delta\eta_c$ of the overpotential. It is given by

$$\Delta\eta_c := \lim_{t\to t_0+T} \eta_c^{off} - \lim_{t\to t_0+t_{on}} \eta_c^{on} \tag{A.25}$$

with unknown initial conditions η_{c_0} and η_{c_1}. The initial condition η_{c_1} can be calculated by demanding continuity at $t = t_0 + t_{on}$ between both solutions: $\eta_{c_1} \triangleq \lim_{t\to t_0+t_{on}} \eta_c^{on}$. We get from Eqn. A.23

$$\exp(b\,\eta_{c_1}) = \frac{g}{h} + \left(\exp(b\,\eta_{c_0}) - \frac{g}{h}\right) \exp(-h\,t_{on})\,. \tag{A.26}$$

The initial condition η_{c_0} can be obtained by demanding $\eta_{c_0} \triangleq \lim_{t\to t_0+T} \eta_c^{off}$. This is valid for the stationary case and we get

$$\exp(b\,\eta_{c_0}) = \frac{(\frac{g}{h})^2 \exp(-h\,t_{on}) - g(T - t_{on})}{\frac{g}{h}\exp(-h\,t_{on}) - 1} \tag{A.27}$$

from calculating this limit from Eqn. A.24 after inserting Eqn. A.26. The initial conditions in the solutions can now be eliminated by inserting Eqn. A.26 and Eqn. A.27 in Eqn. A.23 and Eqn. A.24. Therefore, the stationary oscillation amplitude of the overpotential can now be calculated from Eqn. A.25. With the relation $\overline{q} = t_{on}/T$ from Eqn. 5.7 the formula in Eqn. 5.24 results. Note that the oscillation amplitude $\Delta\eta_c = \eta_{c_0} - \eta_{c_1}$ has to be always greater than zero, because in fuel cell operation we have $\eta_{c_0} > \eta_{c_1}$. With Eqn. A.26 and Eqn. A.27 and $\overline{q} = t_{on}/T$ this condition can be reformulated to $(1 - \overline{q})\,T\,h > 1$.

Bibliography

[1] M. Acosta, C. Merten, G. Eigenberger, H. Class, R. Helmig, B. Thoben, and H. Muller-Steinhagen. Modeling non-isothermal two-phase multicomponent flow in the cathode of PEM fuel cells. *Journal of Power Sources*, 159(2):1123–1141, 2006. 50

[2] K. Adzakpa, J. Ramousse, Y. Dub, H. Akremi, K. Agbossou, M. Dostie, A. Poulin, and M. Fournier. Transient air cooling thermal modeling of a pem fuel cell. *Journal of Power Sources*, 179(1):164–176, 2008. 81

[3] J.-W. Ahn and S.-Y. Choe. Coolant controls of a pem fuel cell system. *Journal of Power Sources*, 179(1):252–264, 2008. 81, 95

[4] F. Barbir. *PEM Fuel Cells*. Academic Press Sustainable World. Elsevier, 2005. 2, 3, 71, 102

[5] M. Bautista, Y. Bultel, and P. Ozil. Polymer electrolyte membrane fuel cell modelling: d.c. and a.c. solutions. *Chemical Engineering Research and Design*, 82(7):907–917, 2004. 65

[6] A. Bazylak. Liquid water visualization in pem fuel cells: A review. *International Journal of Hydrogen Energy*, In Press, Corrected Proof:–. ISSN 0360-3199. 9, 80

[7] J. Bear. *Dynamics of Fluid in Porous Media*. Elsevier, 1972. 15

[8] J. Benziger, E. Chia, J. Moxley, and I. Kevrekidis. The dynamic response of pem fuel cells to changes in load. *Chemical Engineering Science*, 60(6):1743–1759, 2005. 39, 66

[9] R. Borup, J. Meyers, B. Pivovar, Y. S. Kim, R. Mukundan, N. Garland, D. Myers, M. Wilson, F. Garzon, D. Wood, P. Zelenay, K. More, K. Stroh, T. Zawodzinski, J. Boncella, J. E. McGrath, M. Inaba, K. Miyatake, M. Hori, K. Ota,

Z. Ogumi, S. Miyata, A. Nishikata, Z. Siroma, Y. Uchimoto, K. Yasuda, K.-i. Kimijima, and N. Iwashita. Scientific aspects of polymer electrolyte fuel cell durability and degradation. *Chemical Reviews*, 107(10):3904–3951, 2007. 4, 5, 6

[10] K. Brennan, S. L. Campbell, and L. R. Petzold. *Numerical Solution of Initial Value Problems in Differential-Algebraic Equations*. Classics in Applied Mathmatics. Society for Industrial and Applied Mathmatics, 1996. 40

[11] Y. Bultel, K. Wiezell, F. Jaouen, P. Ozil, and G. Lindbergh. Investigation of mass transport in gas diffusion layer at the air cathode of a pemfc. *Electrochimica Acta*, 51(3):474–488, 2005. 65

[12] X. Cheng, Z. Shi, N. Glass, L. Zhang, J. Zhang, D. Song, Z.-S. Liu, H. Wang, and J. Shen. A review of pem hydrogen fuel cell contamination: Impacts, mechanisms, and mitigation. *Journal of Power Sources*, 165(2):739–756, Mar. 2007. ISSN 0378-7753. 4, 5

[13] W. Choi, J. Howze, and P. Enjeti. Development of an equivalent circuit model of a fuel cell to evaluate the effects of inverter ripple current. *Journal of Power Sources*, 158(2):1324–1332, 2006. 57

[14] M. Danzer and E. Hofer. Electrochemical parameter identification - an efficient method for fuel cell impedance characterisation. *Journal of Power Sources*, 183 (1):55–61, 2008. 71

[15] M. A. Danzer, J. Wilhelm, H. Aschemann, and E. P. Hofer. Model-based control of cathode pressure and oxygen excess ratio of a PEM fuel cell system. In *10th Ulm Electro Chemical Talks*, 2007. 6

[16] M. A. Danzer, J. Wilhelm, H. Aschemann, and E. P. Hofer. Model-based control of cathode pressure and oxygen excess ratio of a pem fuel cell system. *Journal of Power Sources*, 176(2):515–522, 2008. 79

[17] F. de Bruijn, V. Dam, and G. Janssen. Review: Durability and Degradation Issues of PEM Fuel Cell Components. *Fuel Cells*, 8(1):3–22, 2008. 4, 5, 6, 65

[18] R. Eckl, W. Zehtner, C. Leu, and U. Wagner. Experimental analysis of water management in a self-humidifying polymer electrolyte fuel cell stack. *Journal of Power Sources*, 138(1-2):137–144, 2004. 39

[19] M. Eikerling and A. A. Kornyshev. Electrochemical impedance of the cathode catalyst layer in polymer electrolyte fuel cells. *Journal of Electroanalytical Chemistry*, 475(2):107–123, 1999. 32, 35

[20] R. W. Erickson and D. Maksimović. *Fundamentals of Power Electronics*. Springer, 2001. 33, 58, 59, 65, 78, 79, 109

[21] European Commission. Developing new energy for the future. Announcement, October 2008. 1

[22] European Hydrogen & Fuel Cells Technology Platform. Strategic research agenda & deployment strategy. Strategic overview, 2005. 1

[23] European Hydrogen & Fuel Cells Technology Platform. Implementation plan. Status report, 2007. 1

[24] N. Fouquet, C. Doulet, C. Nouillant, G. Dauphin-Tanguy, and B. Ould-Bouamama. Model based PEM fuel cell state-of-health monitoring via ac impedance measurements. *Journal of Power Sources*, 159(2):905–913, 2006. 50

[25] R. S. Gemmen. Analysis for the effect of inverter ripple current on fuel cell operating condition. *Transactions of the ASME*, 125:576–585, 2003. 57

[26] A. Gensior, O. Woywode, J. Rudolph, and H. Güldner. On differential flatness, trajectory planning, observers, and stabilization for dc-dc converters. *IEEE Transactions on Circuits and Systems*, 53:2000–20010, 2006. 78, 79

[27] J. Golbert and D. R. Lewin. Model-based control of fuel cells:: (1) regulatory control. *Journal of Power Sources*, 135(1-2):135–151, 2004. 7, 50, 79

[28] R. Hanke-Rauschenbach, M. Mangold, and K. Sundmacher. Bistable current-voltage characteristics of pem fuel cells operated with reduced feed stream humidification. *J. Electrochem. Soc.*, 155(2):B97–B107, 2008. 39, 66, 77

[29] A. Hermann, T. Chaudhuri, and P. Spagnol. Bipolar plates for pem fuel cells: A review. *International Journal of Hydrogen Energy*, 30(12):1297–1302, Sept. 2005. ISSN 0360-3199. 3

[30] High Level Group. Hydrogen energy and fuel cells: A vision of our future. Final report, European Commision Community Research, 2003. 1

[31] W. H. Hogarth and J. B. Benziger. Operation of polymer electrolyte membrane fuel cells with dry feeds: Design and operating strategies. *Journal of Power Sources*, 159:968–978, 2006. 79

[32] International Energy Agency. Prospects for hydrogen and fuel cells. Energy technology analysis, 2005. 4

[33] International Energy Agency. Energy technology essentials - fuel cells, 2007. 4

[34] International Energy Agency. Key world energy statistics, 2008. 1

[35] International Energy Agency. *World Energy Outlook*. 2008. 1

[36] S. G. Kandlikar and Z. Lu. Thermal management issues in a pemfc stack - a brief review of current status. *Applied Thermal Engineering*, In Press, Corrected Proof, 2008. 6

[37] A. Katsaounis, S. Balomenou, D. Tsiplakides, S. Brosda, S. Neophytides, and C. Vayenas. Proton tunneling-induced bistability, oscillations and enhanced performance of pem fuel cells. *Applied Catalysis B: Environmental*, 56(3):251–258, 2005. 39, 77

[38] H. K. Khalil. *Nonlinear Systems*. Pearson Education International, 2000. 88, 89

[39] S. D. Knights, K. M. Colbow, J. St-Pierre, and D. P. Wilkinson. Aging mechanisms and lifetime of PEFC and DMFC. *Journal of Power Sources*, 127(1-2): 127–134, 2004. 39

[40] A. A. Kulikovsky. The effect of stoichiometric ratio [lambda] on the performance of a polymer electrolyte fuel cell. *Electrochimica Acta*, 49(4):617–625, 2004. 77

[41] A. A. Kulikovsky, H. Scharmann, and K. Wippermann. On the origin of voltage oscillations of a polymer electrolyte fuel cell in galvanostatic regime. *Electrochemistry Communications*, 6(7):729–736, 2004. 39

[42] A. Kumar and D. P. *Control of nonlinear differential algebraic equation systems*. Chapman & Hall/CRC, 1999. 81

[43] P. Kurzweil. *Brennstoffzellentechnik*. Vieweg, 2003. 2

[44] Y. A. Kuznetsov. *Elements of Applied Bifurcation Theory*. Springer, third edition, 2004. 40

[45] K. C. Lauzze and D. J. Chmielewski. Power control of a polymer electrolyte membrane fuel cell. *Industrial and Engineering Chemistry Research*, 45(13): 4661–4670, 2006. 79

[46] R. Leyva, A. Cid-Pastor, C. Alonso, I. Queinnec, S. Tarbouriech, and L. Martinez-Salamero. Passivity-based integral control of a boost converter for large-signal stability. *IEE Proc.-Control Theory Appl.*, 153(2):139–146, 2006. 78, 79

[47] X. Li and I. Sabir. Review of bipolar plates in pem fuel cells: Flow-field designs. *International Journal of Hydrogen Energy*, 30(4):359–371, Mar. 2005. ISSN 0360-3199. 3

[48] S. Litster and G. McLean. Pem fuel cell electrodes. *Journal of Power Sources*, 130(1-2):61–76, May 2004. ISSN 0378-7753. 3

[49] G. Ludyk. *Theoretische Regelungstechnik 1*. Springer, 1995. 67, 81, 83

[50] J. Lunze. *Regelungstechnik 2*. Springer, 2002. 84

[51] R. Makharia, M. F. Mathias, and D. R. Baker. Measurement of catalyst layer electrolyte resistance in pefcs using electrochemical impedance spectroscopy. *J. Electrochem. Soc.*, 152(5):A970–A977, 2005. 65

[52] M. Mangold, A. Kienle, E. D. Gilles, and K. D. Mohl. Nonlinear computation in DIVA – methods and applications. *Chemical Engineering Science*, 55(2): 441–454, 2000. 24, 31, 40

[53] M. Mangold, S. Motz, and E. D. Gilles. A network theory for the structured modelling of chemical processes. *Chemical Engineering Science*, 57(19):4099–4116, 2002. 24

[54] W. Na. Feedback-linearization-based nonlinear control for pem fuel cells. *IEEE transactions on energy conversion*, 23(1):179–190, 2008. 79

[55] H. Nijmeijer and A. J. van der Schaft. *Nonlinear Dynamical Control Systems*. Springer, 1995. 81, 82

[56] R. P. O'Hayre, S.-W. Cha, W. Colella, and F. B. Prinz. *Fuel Cell Fundamentals*. John Wiley & Sons, Inc., 2006. 2, 71

[57] S. J. Paddison and K. S. Promislow, editors. *Device and Materials Modeling in PEM Fuel Cells*. Springer, 2009. 3

[58] J. Pukrusphan, A. G. Stefanopoulou, and H. Peng. Control of fuel cell breathing. *IEEE Control Systems Magazine*, 24(2):30–46, 2004. 6, 50, 79

[59] S. Rahmsdorf and H. J. Schellnhuber. *Der Klimawandel*. C.H.BECK, 2007. 1

[60] P. Rathke. Modellbildung und Simulation des zweiphasigen Wasserhaushalts in den Gasverteilungsstrukturen von Bipolarplatten für PEM-Brennstoffzellen. Student's thesis (german), Otto-von-Guericke-Universität Magdeburg, 2009. 80, 109

[61] M. Rubio, A. Urquia, and S. Dormido. Diagnosis of pem fuel cells through current interruption. *Journal of Power Sources*, 171(2):670–677, 2007. 65

[62] L. Schindele. *Einsatz eines leistungselektronischen Stellglieds zur Parameteridentifikation und optimalen Betriebsführung von PEM-Brennstoffzellensystemen (German)*. PhD thesis, University Karlsruhe, Germany, 2006. 71

[63] W. Schmittinger and A. Vahidi. A review of the main parameters influencing long-term performance and durability of pem fuel cells. *Journal of Power Sources*, 180(1):1–14, May 2008. ISSN 0378-7753. 4, 5, 6

[64] J. Schumacher, P. Gemmar, M. Denne, M. Zedda, and M. Stueber. Control of miniature proton exchange membrane fuel cells based on fuzzy logic. *Journal of Power Sources*, 129(2):143–151, Apr. 2004. ISSN 0378-7753. 79

[65] M. Seifart. *Analoge Schaltungen*. Verlag Technik, 2003. 33

[66] R. Seydel. *Practical Bifurcation and Stability Analysis: From Equilibrium to Chaos*. Springer, second edition, 1994. 40

[67] W. Shireen, R. A. Kulkarni, and M. Arefeen. Analysis and minimization of input ripple current in pwm inverters for designing reliable fuel cell power systems. *Journal of Power Sources*, 156(2):448–454, 2006. 57

[68] C. Siegel. *PEM Fuel Cell Modeling and Simulation Using Matlab*. Academic Press, 2008. 3

[69] C. Siegel. Review of computational heat and mass transfer modeling in polymer-electrolyte-membrane (pem) fuel cells. *Energy*, 33(9):1331–1352, Sept. 2008. ISSN 0360-5442. 3

[70] T. E. Springer, T. A. Zawodzinski, and S. Gottesfeld. Polymer electrolyte fuel cell model. *J. Electrochem. Soc.*, 138(8):2334–2342, 1991. 19

[71] S. Srinivasan. *Fuel Cells: From Fundamentals to Applications*. Springer, 2006. 2, 9

[72] T. Trabold, J. Owejan, D. Jacobson, M. Arif, and P. Huffman. In situ investigation of water transport in an operating pem fuel cell using neutron radiography: Part 1 - experimental method and serpentine flow field results. *International Journal of Heat and Mass Transfer*, In Press, Corrected Proof:–. 9, 80

[73] F. Tränkle, M. Zeitz, M. Ginkel, and E. Gilles. PROMOT: A modeling tool for chemical processes. *Mathematical and Computer Modelling of Dynamical Systems*, 6(3):283–307, 2000. 24, 31

[74] K. Tüber, D. Pocza, and C. Hebling. Visualization of water buildup in the cathode of a transparent pem fuel cell. *Journal of Power Sources*, 124(2):403–414, 2003. 9, 80

[75] S. Varigonda and M. Kamat. Control of stationary and transportation fuel cell systems: Progress and opportunities. *Computers & Chemical Engineering*, 30 (10-12):1735–1748, 2006. 6

[76] W. Vielstich, A. Lamm, and H. A. Gasteiger, editors. *Handbook of Fuel Cells: Fundamentals, Technology and Applications*, volume 1-4. Wiley, 2003. 2, 3

[77] A. Z. Weber and J. Newman. Transport in polymer-electrolyte membranes, i. physical model. *Journal of The Electrochmical Society*, 150(7):A1008–A1015, 2003. 11, 14, 17, 18

[78] A. Z. Weber and J. Newman. Transport in polymer-electrolyte membranes, ii. mathematical model. *Journal of The Electrochemical Society*, 151(2):A311 – A325, 2004. 11, 14, 17, 18, 105

[79] A. Z. Weber and J. Newman. Transport in polymer-electrolyte membranes, iii. model validation in a simple fuel-cell model. *Journal of The Electrochemical Society*, 151(2):A326–A339, 2004. 11, 17

[80] A. Z. Weber, R. M. Darling, and J. Newman. Modeling two-phase behavior in PEFCs. *Journal of The Electrochemical Society*, 151(10):A1715–A1727, 2004. 15, 20, 45, 47

[81] C. H. Woo and J. Benziger. Pem fuel cell current regulation by fuel feed control. *Chemical Engineering Science*, 62(4):957–968, 2007. 79

[82] H. Wu, P. Berg, and X. Li. Non-isothermal transient modeling of water transport in pem fuel cells. *Journal of Power Sources*, 165(1):232–243, 2007. 50

[83] J. Wu, X. Z. Yuan, J. J. Martin, H. Wang, J. Zhang, J. Shen, S. Wu, and W. Merida. A review of pem fuel cell durability: Degradation mechanisms and mitigation strategies. *Journal of Power Sources*, 184(1):104–119, Sept. 2008. ISSN 0378-7753. 4, 5

[84] C. Yang, S. Srinivasan, A. B. Bocarsly, S. Tulyani, and J. B. Benziger. A comparison of physical properties and fuel cell performance of nafion and zirconium phosphate/nafion composite membranes. *Journal of Membrane Science*, 237(1-2):145–161, 2004. 33

[85] N. Yousfi-Steiner, P. Moçotéguy, D. Candusso, D. Hissel, A. Hernandez, and A. Aslanides. A review on pem voltage degradation associated with water management: Impacts, influent factors and characterization. *Journal of Power Sources*, 183(1):260–274, 2008. 6

[86] N. Yousfi-Steiner, P. Moçotéguy, D. Candusso, and D. Hissel. A review on pem fuel cell catalyst degradation and starvation issues: causes, consequences and diagnostic for mitigation. *Journal of Power Sources*, In Press, Accepted Manuscript, 2009. ISSN 0378-7753. 6

[87] F. Zenith and S. Skogestad. Control of fuel cell power output. *Journal of Process Control*, 17(4):333–347, 2007. 57, 100

[88] J. Zhang, J. D. Fehribach, and R. Datta. Mechanistic and bifurcation analysis of anode potential oscillations in pemfcs with co in anode feed. *J. Electrochem. Soc.*, 151(5):A689–A697, 2004. 39, 77

[89] T. Zhao, K. D. Kreuer, and T. Van Nguyen, editors. *Advances in Fuel Cells*. Elsevier Science & Technology, 2007. 3

[90] C. Ziegler, H. Yu, and J. Schumacher. Two-phase dynamic modeling of the PEMFC and simulation of cyclo-voltammograms. *Journal of The Electrochemical Society*, 152(8):A1555–A1567, 2005. 8, 11, 15, 20, 21, 22, 33, 50